Optimization and Characterization of Laser Powder Bed Fusion of AlSi10Mg for Complex Aerospace Structures

by

Zachariah Mears

A thesis
presented to the University of Waterloo
in fulfillment of the
thesis requirement for the degree of
Master of Applied Science
in
Mechanical and Mechatronics Engineering

Waterloo, Ontario, Canada, 2025

© Zachariah Mears 2025

Author's Declaration

I hereby declare that I am the sole author of this thesis. This is a true copy of the thesis, including any required final revisions, as accepted by my examiners.

I understand that my thesis may be made electronically available to the public.

Abstract

Manufacturing for the aerospace industry is dominated by the production of components which operate in extreme environments under high loads and must be as light-weight as possible. Aerospace components are typically highly complex and produced in relatively small quantities, whereby manufacturing typically involves specialized tooling, with high costs due to complexity. Additive Manufacturing (AM) presents a potential solution to these challenges. AM presents unparalleled design freedom, since increasing the complexity of a part does not increase the cost. Not only can AM be used to aid in the manufacturing of complex aerospace components, but it can enable new designs that can significantly reduce weight and increase the performance of assemblies and systems. In particular, laser powder bed fusion (LPBF) is one of the most widely adopted metal AM technologies, as it provides high feature resolution, while achieving fully dense parts, with tailored microstructure. Although there are a number of use cases for LPBF in aerospace, there are still a number of manufacturing and design constraints that have limited its adoption. This work adds to the body of knowledge towards addressing these limitations by investigating several topics important to the practical use of LPBF for the manufacturing of aluminum aerospace components with complex design architectures, particularly in considering thin walled structures with complex surface inclinations: tailoring surface topography, studying mechanical properties, and customizing design architectures for structural and performance criteria.

A case study is presented considering a key structural member for a high powered sounding rocket. The structural member is re-designed for AM to demonstrate a new methodology for the design of lightweight structures under compressive loading. Simulations were deployed which used the stress response of an initial solid beam design to create a functionally graded hollow shell that was then augmented with surface lattices to further

prevent thin wall buckling. After the part was printed from AlSi10Mg using LPBF, it was subjected to compression testing. A novel test fixture was designed and validated to allow fixed-end free-end buckling testing. The design exhibited exceptionally even stress distribution and very high buckling resistance, demonstrating a 98% increase in strength compared to the conventional part design, despite the two designs having equal mass.

One of the largest design constraints of LPBF is the inability to print structures with steep overhangs. When these overhangs can be printed, the downward facing surface, known as downskin, typically has a very high surface roughness. To enable the printing of structures with steeper overhangs and better surface roughness, a number of process parameter combinations are tested across downskin angles ranging from 75° to as low as 20°. A modeling approach is proposed for predicting the effect of process parameters on downskin roughness and the predicted performance is found to align closely with the experimentally measured roughness. A set of process parameters are identified that enable the printing of parts at angles as low as 20° with good surface roughness.

The tensile properties of thin-walled structures printed from AlSi10Mg are then investigated using a select range of process parameters. The effect of part thickness, part orientation, and part finishing (machining vs. as-built) on the measured tensile properties of the samples is discussed. The Young's modulus, yield strength, ultimate tensile strength, and elongation at break are characterized for these process parameters. The effect of overhang angle on tensile properties is measured, with significant reductions in performance found at low downskin angles. The design of a number of complex aerospace components which rely on the results of this work are then discussed. This includes multiple parts slated to fly on the 2nd ever Canadian built liquid rocket.

Acknowledgements

I would like to thank everyone at the Multi-Scale Additive Manufacturing lab for their continual support and assistance, for always being happy to talk when I had research questions, and for always making the lab a fun place to work.

In particular, I would like to thank Prof. Mihaela Vlasea for being an amazing supervisor. She has given me invaluable guidance throughout my degree, always made time for me when I have needed advice, and encouraged many of my most ambitious projects.

Others who deserve special thanks are: Allan David Rogalsky, for his guidance on a wide range of subjects from specific research topics, to testing methodologies, to statistics and data analysis, all while working to make sure I and everyone in the lab were operating safely. Jerry Ratthapakdee, for the countless hours of work he put into operating the machines that allowed for my research to succeed, for tolerating that every single one of my builds was either big, ambitious, complicated, or risky, and for teaching me all of the important design considerations only an experienced technician would notice. I would also like to thank Lisa Brock for her work during her Master's degree. While we have not met, her research gave me a great base to start from and allowed me to explore much further into the topics that I am passionate about. Thank you to my friends, Krishn and Shannon, who helped to proofread this thesis and reduce the number of spelling mistakes.

Finally, I would like to thank the Waterloo Rocketry team. In addition to providing invaluable learning opportunities during my undergraduate degree, the team provided me with practical design challenges that helped to guide and direct my research when other industry projects fell short. The team is comprised of some truly remarkable students and I am excited to see them continue to achieve ever more impressive accomplishments.

Dedication

To my family and to my friends who are like family.

Table of Contents

Author's Declaration ii

Abstract iii

Acknowledgements v

Dedication vi

List of Figures xii

List of Tables xxi

1 Introduction 1

1.1 Past Work . . . 3

1.2 Thesis Outline . . . 5

2 Optimization of Rocket Structural Members via Additive Manufacturing 7

2.1 Introduction . . . 8

2.2 Application Background . . . 9

2.3 Materials and Methods . . . 12

2.3.1 Printing Process . . . 12

2.3.2 Design Case Study Workflow . . . 15

2.3.3 Validation and Testing Methodology 24
2.4 Results and Discussion 30
2.4.1 Test Samples 30
2.4.2 Test Results 31
2.4.3 Comparison of Design Performance 33
2.5 Conclusions 36

3 Optimization of Downskin Surface Roughness for AlSi10Mg Structures Printed using Laser Powder Bed Fusion 38

3.1 Introduction 39
3.2 Materials and Methods 42
3.2.1 Printing Process 42
3.2.2 Modeling 43
3.2.3 Test Sample Geometry 52
3.2.4 Process Parameter Selection 52
3.2.5 Surface Roughness Measurement 57
3.2.6 Computed Tomography 57
3.3 Results and Discussion 58
3.3.1 Prediction of Process Parameter Performance 58
3.3.2 Surface Roughness Results 60
3.3.3 Comparison Between Modeling and Results 65
3.3.4 CT Scan Analysis 68
3.3.5 Core Power Investigation 72
3.3.6 Recommended Process Parameters 73
3.4 Conclusions 77

4 Investigation of Part Thickness and Orientation on the As-Built Tensile Properties of AlSi10Mg Manufactured using Laser Powder Bed Fusion 79

4.1 Introduction . . . 80

4.2 Materials and Methods . . . 83

4.2.1 Printing Process and Paramerters . . . 83

4.2.2 Design of Experiment . . . 85

4.2.3 Characterization . . . 91

4.3 Results and Discussion . . . 96

4.3.1 Surface Roughness . . . 96

4.3.2 Tensile Measurement . . . 101

4.3.3 Young's Modulus and Correction of Cross-sectional Area Error . . . 104

4.3.4 Effect of Thickness and Orientation on Tensile Properties . . . 108

4.3.5 Effect of Part Angle on Tensile Properties . . . 108

4.3.6 Effect of Coupon Type and Process Parameters on Tensile Properties 115

4.4 Conclusions . . . 120

5 Research Applications 123

5.1 Turbopump . . . 124

5.1.1 Turbine Housing . . . 127

5.1.2 Inducer and Impeller . . . 129

5.1.3 Pump Housing . . . 131

5.1.4 Results and Future Work . . . 133

5.2 Flight Longerons . . . 134

5.3 Printed Injectors . . . 140

5.3.1 Channel Diameter Calibration . . . 141

5.3.2 Injector Design and Testing . . . 143

5.4 Tronosjet Waveguides 149

6 Conclusions and Future Works **152**

6.1 Future work 154

6.1.1 Structural Optimization 155

6.1.2 Downskin Surface Roughness and Print Angle Optimization 156

6.1.3 Tensile Property Charaterization 159

Letters of Copyright Permission **161**

References **163**

APPENDICES **186**

A Chapter 2: Structural Optimization **187**

Appendix A.1 Build Plate Layout 188

Appendix A.2 Test Fixture Alignment 189

Appendix A.3 Test Data Including Outliers 190

B Chapter 3: Downskin Surface Roughness Optimization **192**

Appendix B.1 Numerical Values for Downskin Overlap Model 193

Appendix B.2 Previous Work on Downskin Rougnness of 7A76 Aluminum . . . 195

Appendix B.3 Complete Surface Roughness Measurements 197

Appendix B.4 Analysis of Variance Code 204

C Chapter 4: Tensile Properties **207**

Appendix C.1 Tensile Data Processing Code 208

Appendix C.1.1 process_samples.py 208

Appendix C.1.2 calculate_properties.py 211
Appendix C.2 Complete Tensile Data 216
Appendix C.3 Analysis of Variance Code 219
Appendix C.3.1 Surface Roughness ANOVA Code 219
Appendix C.3.2 Tensile Properties ANOVA Code 220

List of Figures

2.1 Location of longerons on the Leviathan of the Sky rocket and rendering of a longeron. Each longeron is comprised of a primary strut machined from Aluminum 7075-T6 square stock with a waterjet cut Aluminum 6061-T6 mounting tab attached at each end with a pair of #10-32 3/8" countersunk bolts. 10

2.2 Effective length of columns based on end conditions. Column length - L, effective length - L_{ef}, critical load - P_{cr}. Adapted from [30]. 11

2.3 Processes diagram for Laser Powder Bed Fusion [34]. 12

2.4 Maximum longeron footprint and required mounting hole locations. All dimensions in mm. 16

2.5 Design iterations: (a) Iteration 1: uniform lattice and shell (b) Iteration 2: graded shell with lattice and overhang considerations (c) Iteration 3: final design with surface lattices. 21

2.6 Von Mises stress analysis results: (a) Iteration 1: stress distribution is high and uneven between front and back of the part (b) Iteration 2: stress distribution is better but still uneven. Significant stress concentrations at the corners of the part near the fastener locations. Stress on internal lattice is very low (c) Iteration 3: stress is much lower and stress distribution is fairly even across the part (d) Legend. 22

2.7 First buckling mode based on linear buckling simulations: (a) Iteration 1 (BLF = 1.66) (b) Iteration 2 (BLF = 3.21) (c) Iteration 3 (BLF = 3.64). . 23
2.8 Test fixture: (a) Rendering with shaft cover removed (b) Fixture in test frame during test. 27
2.9 Constant displacement rate FEA simulation of the test fixture and longeron. Shown in the buckled state with deformation true to scale. Simulation was used to validate the fixture would perform as expected before manufacturing. 28
2.10 Low cost test fixture validation sample manufactured from 1" aluminum angle stock with waterjet cut mounting plates press-fit to each end. Used for experimental validation of the test fixture. 29
2.11 Experimental test results for conventional and printed longerons. Failure load is considered to be the maximum measured force. All printed longerons significantly outperform the conventional longerons. 33
2.12 Comparison of performance for different validation methods. Euler and Johnson calculations give equivalent results, with the appropriate method being used based on the slenderness ratio of each design as discussed in Section 2.3.3. The performance increase of the printed design over the conventional design is significant for every assessment method. 35

3.1 Demonstration part showing downskin surfaces in blue, sideskin surfaces in purple, and upskin surfaces in red, as well as the part core in orange. The build direction is orthogonal to the plane of the build plate. 41
3.2 Critical melt depth location for MDR, based on hatch spacing, h [71]. . . . 46

3.3 Graphical diagram of the melt pool overlap model at two different angles. The meltpool is represented by the orange and green areas, while the solid part is shown in blue. Solid fraction is the amount of re-melted part (orange) vs fresh powder (green) in the melt pool. Conductivity is assumed proportional to the length of the melt pool border contacting the solid part (the border between the blue and orange areas): (a) 90° sideskin printing: most of the meltpool is dense, re-melted part and there is high conductivity to the surrounding solid part. (b) 20° downskin printing: most of the meltpool is less dense fresh powder and there is much less contact with the solid part for heat to conduct away. 50
3.4 Relative material conductivity and solid fraction based on melt pool overlap model. Numerical values provided in Appendix B.1. 51
3.5 Sample geometries: (a) 3mm thick facet (b) 1mm thick facet (c) 1mm thick 20° sample. 53
3.6 Reduced Build Volume build plate with 10 of each sample geometry. 54
3.7 Process map of tested process parameters. 56
3.8 Estimated keyhole number vs angle for each set of process parameters as a function of downskin angle. 59
3.9 Estimated MDR vs angle for each set of process parameters. The blue region indicates too low an MDR, likely to result in lack of fusion, while the red region indicates a high MDR likely to result in excessive heat input. 60
3.10 Best and worst surfaces measured. (a) Best roughness: sample 6, thin structure, 75°, $R_a = 8.1\mu m$ (b) Worst roughness: sample 2, 20° structure, 20°, $R_a = 98.6\mu m$. 61

3.11 Average measured downskin roughness vs angle for thin and 20° samples with standard deviation. 62
3.12 Average roughness vs angle for tested core process parameters. 65
3.13 2nd order polynomial surface, of the form $z = a + bx + cy + dx^2 + ey^2 + fxy$, fit to measured roughness data as a function of angle and MDR, with $R^2 = 0.876$. The steep convex curvature indicates a clear ideal MDR at each angle corresponding to the lowest surface roughness. 66
3.14 Ideal MDR for lowest surface roughness based on fitted surface. The fitted surface is plotted as a height map. The ideal MDR varies from 2.15 at 20° to 1.95 at 75°. 67
3.15 Height map comparison of powder adhesion on 75° downskin. (a) Sample # 6, thin coupon, with minimal powder adhesion, $S_a = 8.1\mu m$. Roughness is dominated by gradual waviness from the underlying texture with occasional particle adhesion. (b) Sample # 9, thin coupon, with significant powder adhesion, $S_a = 14.4\mu m$. Roughness is dominated by adhered particles, visible as circular yellow and orange regions. 69
3.16 CT cross sections of samples. Thick samples maintain a high density while significant keyhole porosity is observed in thin samples, particularly at low downskin angles. (a) Sample # 3 thick. (b) Sample # 7 thick. (c) Sample # 3 thin. (d) Sample # 7 thin. (e) Sample # 3 20°. (f) Sample # 7 20°. . 71
3.17 CT cross sections of modified core power samples. Surface roughness and dimentional accuracy improve as power decreases, while porocity transitions from keyhole to high density, to severe lack of fusion: (a) Sample A, core power 255.3 W (b) Sample B, core power 240 W (c) Sample C, core power 220 W (d) Sample D, core power 200 W (e) Sample E, core power 180 W. 74

3.18 Comparison of downskin surface roughness data published by EOS vs roughness measurements from optimal process parameters [41]. 76

4.1 Layout of tensile samples (blue) on sample blanks (orange). The area used for measuring surface roughness is shown in red. Top: horizontal coupon blank use for thick (3 mm) and thin (1 mm) samples. Bottom: overhang sample blank used for 75°, 60°, 45°, 30°, and 20° samples, 1 mm thick. . . 86

4.2 Build plate layout for horizontal and overhang tensile experiment indicating X and Y axis, along with the recoater and gas flow directions. Only samples 1YTN - 3YTK, and samples 3XTN - 20-1 are used in this work. 88

4.3 Build plate layout for vertical sample coupons showing the recoater and gas flow directions. Only the labeled samples (R1 - R10 and F1 - F10) are discussed in this work. 89

4.4 Sample geometry and dimensions. (a) Subsized ASTM E8 sample geometry with reduced grip length used for horizontal, overhang, and vertical flat samples. (b) round subsized ASTM E8M sample geometry with dimensions matching those used by a major machine manufacturer [100], [101]. 90

4.5 Tensile tester setup with extensometer attached to a verification sample via elastic bands. 3D printed jigs are used to aid the alignment of samples (seen in blue). 94

4.6 Stress Strain curve for sample 3YTK-T, showing the raw data, as well as the calculated linear region used to compute the 0.2% offset, the 0.2% offset line, the intersection point defining the yield strength, and the UTS point. 95

4.7 Complete set of tensile coupons after machining. Top left: verification samples, middle left: machined vertical round samples, bottom left: flat unmachined vertical samples. Middle and right are the waterjet horizontal and overhang samples. 103
4.8 Calculated young's modulus of horizontal samples based on physically measured cross-sectional area. 105
4.9 Deviation between the sample CAD design and measured sample thickness against average surface roughness of each horizontal sample. A linear line of best fit is used, with an R^2 of 0.481. 106
4.10 Comparison of calculated Young's modulus based on manual cross-section measurements vs. corrected cross-section based on CT results. The average Young's modulus using the corrected cross-section is 69.8 ± 0.7 GPa. . . . 107
4.11 Measured UTS and yield strength of horizontal samples based on corrected cross-section. The average UTS is 422.1 ± 4.1 MPa, and the average yield strength is 265.6 ± 1.0 MPa. 109
4.12 Measured % elongation at break for all horizontal samples. The average is 6.1 ± 0.4%. 110
4.13 Average thickness of overhang samples based on CT vs print angle relative to the build plate. There are two replicates at each angle. 111
4.14 Young's modulus measured for each overhang sample using cross-section from CT. 112
4.15 Measured UTS and yield strength for overhang samples. 113
4.16 Measured elongation at break for overhang samples. 114
4.17 Measured Young's modulus for all vertical samples. The average Young's modulus is 66.9 ± 1.0 GPa. 118

4.18 Measured UTS and yield strength of vertical samples. The average UTS is 420.9 ± 12.9 MPa, and the average yield strength is 231.0 ± 5.0 MPa. . . . 119
4.19 Measured elongation at break for all vertical samples. The average elongation is 5.2 ± 0.8 %. 120

5.1 Cross-section of the Waterloo Rocketry turbopump assembly. The turbine housing, pump inducer, pump impeller, and pump housing were manufactured using LPBF. 126
5.2 Cross-section of turbopump turbine housing printed from Inconel 625 with lattice supports still attached. A teardrop shaped manifold is used to direct hot gas to the nozzles. 129
5.3 Turbopump inducer and impellers printed from AlSi10Mg: (a) Inducer after machining and support removal. (b) Un-machined impeller in the as-printed state. (c) Impeller after machining and minimal support removal. 131
5.4 Turbopump pump housing printed from AlSi10Mg. Supports have been removed but post-machining has not been completed. 132
5.5 Turbopump housing showing showing distinct line artifact at the point where the downskin scan strategy is disabled. 133
5.6 Aurora injector section assembly. Longerons are highlighted in blue. Note that the top coupler has a wider diameter than the bulkhead at the bottom, resulting in eccentric loading on the longerons. 135
5.7 Aurora longeron simulations with section view: (a) Von Mises stress analysis result. Scale maximum is set to 242 MPa, the Z axis yield strength identified in Chapter 4. (b) First buckling mode based on linear buckling simulation. The buckling load factor (BLF) is 7.99. 138
5.8 Aurora longerons on the build plate after de-powdering. 139

5.9 Initial brazed injector concept. 55 hypodermic needle tubes are brazed into a brass plate to form the fuel injector. These tubes pass through holes in a lower plate, forming an annular gap for oxidizer to flow through. A series of O-ring seals are used to ensure propellants don't mix. 141
5.10 CT scan results for small diameter fluid channels. (a) Cross-section of 1 mm as-designed channel 25 mm long. While some spatter is present, overall the channel is very uniform and free of concerning obstructions. (b) CT slice of sample showing measurements of all tested diameters. 142
5.11 CFD flow visualization of printed injector. Oxidizer enters from the top of the injector, while fuel enters from a port in the upper right corner of the image. The rectangular volume at the bottom of the image is the combustion chamber, and the fuel and oxidizer can be observed impinging on one another. 144
5.12 CFD simulation of pressure drop throughout the fuel channels of the injector used to refine the flow distribution. The fuel orifices can be seen as a low pressure region in green: (a) Initial fuel flow simulation. It was found that the fuel splitter resulted in uneven flow, with a disproportionate amount of fuel entering the inner fuel manifold. (b) Final fuel flow simulation. The fuel splitter (hidden from view by the outer manifolds) now results in an even pressure distribution between the inner fuel manifold and the secondary outer fuel manifold. 146
5.13 Printed injectors after being cut from the build plate but before post-machining. 147

5.14 Eridium injector testing: (a) Cold flow testing of the fuel channels using high pressure water. The two fuel streams of each element impinge, resulting in atomization of the fuel. (b) Static fire of the Eridium engine using the printed injector. The engine operated smoothly, with high combustion efficiency. 148
5.15 Surface roughness measurement of demonstrator waveguides. 151

6.1 Letter confirming right to reproduce Figure 6.1. 161
6.2 Golden Light Publishing open access policy [113]. 162

A.1 Build plate with structural members and various other components for use in other works. 188
A.2 Test fixture alignment process using clamps and 1-2-3 blocks to ensure centering. 189
A.3 Experimental test results for all samples including outliers. 191

List of Tables

2.1 LPBF process parameters for part production. Laser power - P, beam radius - r_b, point distance - p_d, exposure time - t_e, hatch distance - h_d, effective laser power - P_{eff}, and effective velocity - v_{eff}. The drill delay time, t_d, is constant at 10 µs. A standard hatch angle rotation of 67° was deployed. . . 14

2.2 Assumed mechanical properties of as-printed AlSi10Mg and Al7075-T6 [41][40][42]. 15

2.3 Summary of design iteration performance. 24

2.4 Mass of printed and conventional samples. 31

3.1 Properties of AlSi10Mg used for process modeling [15], [26]. 45

3.2 LPBF process parameters used in design of experiment. Laser power - P, beam radius - r_b, point distance - p_d, exposure time - t_e, hatch distance - h, effective laser power - P_{eff}, effective velocity - v_{eff}, and Volumetric Energy Density - VED. The drill delay time, t_d, is constant at 10 µs. A standard hatch angle rotation of 67° was used. 55

3.3 Summary of core and skin process codes used for each sample. 57

3.4 Surface Roughness (Sa) measurements for thin facets and 20° samples in µm. The lowest roughness at each angle is in bold text. 63

3.5 Surface Roughness (Sa) measurements for thick facets in µm. The lowest roughness at each angle is in bold text. 63

3.6 Surface Roughness (Sa) measurements for 20° samples printed with reduced core powers. 73

3.7 Recommended process parameters for AlSi10Mg. Laser power - P, beam radius - r_b, point distance - p_d, exposure time - t_e, hatch distance - h, effective laser power - P_{eff}, effective velocity - v_{eff}, and Volumetric Energy Density - VED. The drill delay time, t_d, is constant at 10 µs. A standard hatch angle rotation of 67° should be used. 76

4.1 Recipe 1: Low roughness optimized LPBF process parameters used for most samples [15]. Laser power - P, beam radius - r_b, point distance - p_d, exposure time - t_e, hatch distance - h, effective laser power - P_{eff}, effective velocity - v_{eff}, and Volumetric Energy Density - VED. The drill delay time, t_d, is constant at 10 µs and a layer height of 35 µm is used. 84

4.2 Recipe 2: Alternate high density optimized LPBF process parameters as reported by Patel et al. [26]. Laser power - P, beam radius - r_b, point distance - p_d, exposure time - t_e, hatch distance - h, effective laser power - P_{eff}, and effective velocity - v_{eff}. The drill delay time, t_d, is constant at 10 µs and a layer height of 35 µm is used. 85

4.3 Measured surface roughness of the horizontal test coupons with no waviness filtering. The sample naming scheme is described in Section 4.2.2. 97

4.4 Measured surface roughness of the overhang test coupons with no waviness filtering. The sample naming scheme is described in Section 4.2.2. 98

4.5 Summary of measured sample dimensions for horizontal and overhang coupons. Width and Thickness are based on manual measurement with calipers. Deviation is the difference between the designed thickness, and the true thickness measured via CT. 101

4.6 Summary of tensile properties for as-printed parts manufactured using Recipe 1. 122

5.1 Process parameters and surface roughness (Sa) measurements for waveguide samples with 45° downskin. The system has a beam diameter of 80 µm. Renishaw B does not use a downskin strategy, so border strategy is listed as downskin. 150

A.1 Failure load of tested samples, outliers are in bold. 190

B.1 Computed values for the downskin melt pool overlap model presented in section 3.2.2. Effective thermal conductivity, K_{eff}, effective density, ρ_{eff}, and effective diffusivity, α_{eff}, are specific to AlSi10Mg. 194

C.1 Measured tensile properties for all samples. Sample dimensions can be found in Table 4.5. 216

Chapter 1

Introduction

A defining feature of manufacturing for the aerospace industry, particularly the space industry, is the dominance of functional performance above other requirements. Aircraft, rockets, and satellites are all highly complex systems by nature of the extreme conditions in which they operate [1]. As such, they are comprised of components that must perform complex functions, while enduring high loads, extreme temperature environments, or both. Lightweighting is also of critical concern, as minor increases in the mass of an aircraft or rocket can result in significant reductions in performance [2]. Typically, aerospace components are produced in relatively low volumes, with high complexity [1]. However, traditional manufacturing of high complexity parts often requires the use of specialized processes and tooling, leading to significant costs associated with the design complexity [3].

Additive manufacturing (AM), also known colloquially as 3D printing, presents a potential solution to this challenge. AM is a manufacturing process where material is deposited one layer at a time to create components based on 3D model data [4]. This allows the cre-

ation of complex structures without the need for specialized tooling. The location of solid material is fully controllable and, unlike conventional manufacturing, there is no additional cost associated with additional design complexity. While this design freedom may help to reduce costs associated with specialized tooling, AM is still a relatively new technology with additional cost drivers [5]. The largest benefits to technology adoption are introduced when design for additive manufacturing (DfAM) is considered. DfAM is a broad subject, but primarily revolves around improving part performance by leveraging the design freedoms of AM, while factoring in the limitations of the technology. Common DfAM methods for improving part performance include latticing, topology optimization, and part consolidation [6], [7]. Often DfAM can result in significant weight savings, performance increases, or reductions in failure points, all of which are hugely beneficial for aerospace applications [8].

There are seven defined types of AM as defined by the American Society for Testing and Materials (ASTM) [9]. Of these AM technologies, laser powder bed fusion (LPBF) has seen a wide adoption for aerospace manufacturing of metal components [1], [10]. LPBF uses a high powered laser directed by mirrors to selectively melt thin layers of powder, layer-by-layer, creating solid metal parts. LPBF has become popular across a number of industries, owing to its ability to create detailed designs with high feature resolution, custom microstructure, and strength, while achieving full density parts with less porosity than casting [11], [12].

One of the many materials available for LPBF is AlSi10Mg; this material has seen broad adoption for the manufacturing of aerospace parts [1]. AlSi10Mg is the most widely used aluminum alloy for AM, as its composition is easily weldable and provides a good balance of printability, high mechanical strength, corrosion resistance, and thermal conductivity [13].

Although there have been a number of use cases for LPBF in aerospace, there are still multiple challenges which have limited its adoption [14]. LPBF can enable extremely complex designs, but it is subject to a number of design constraints: limited ability to print steep overhangs without the use of support structures, relatively high surface roughness, and limitations in the the design and manufacturing of internal features such as channels. In addition, DfAM is still an emerging field of study and the best methodologies for part designs that leverage AM are still an active research topic [6], [7].

The objective of this thesis is to further the available body of knowledge on the design and manufacturing of complex structures for aerospace applications produced from AlSi10Mg using LPBF. To do so, several topics important to the practical engineering design of these structures are discussed, including structural optimization, surface roughness improvement, and characterization of tensile properties. Further background on the manufacturing of AlSi10Mg using LPBF and its relevance are presented within the papers that comprise this work.

1.1 Past Work

In addition to the wide base of available literature on the LPBF manufacturing of AlSi10Mg, the work of L. Brock [15] presents an important base for the further development of AlSi10Mg capabilities presented in this present work. Brock's work used the same LPBF system (AM400, Renishaw, UK) and plasma atomized AlSi10Mg powder (AP&C, Montreal, Canada) as was available for this work, making her findings directly applicable to build upon. Brock's research included a thorough investigation of many of the mechanical properties of AlSi10Mg. She identified two sets of process parameters which enable high density printing of AlSi10Mg, with a tradeoff between slightly higher density (99.95%

dense) and higher production rates (99.84% dense). She also identified a set of process parameters optimized for low surface roughness on the vertical side of printed parts (sideskin). These process parameters are used as a starting point for the design of experiment presented in Chapter 3 and also see usage in Chapter 4. Brock's work also involved the characterization of hardness, wear rate, and corrosion resistance.

While Brock's work was comprehensive, two areas important to the design of complex structures remained to be explored. The first area is the roughness of downward facing surfaces (downskin); while Brock conducted significant research on the optimization of sideskin surface roughness, the work was limited to vertically printed surfaces. Printing of complex structures typically involves the creation of surfaces at a wide variety of angles relative to the build plate, and it is well established that downskin surfaces are the most problematic in regards to high surface roughness [16]. The other area pending investigation is studying the tensile properties of the optimized process parameters developed by Brock. Brock's research did not include investigation into mechanical properties such as Young's modulus, yield strength, ultimate tensile strength (UTS), and elongation at break. These mechanical properties are critical when designing complex components, which are often subjected to significant loading.

Another guiding force in this work is the research conducted by S. Patel [17] on the printing of AlSi10Mg using LPBF. Patel's work developed a set of process parameters that enable printing of AlSi10Mg at densities as high as 99.98%. These process parameters are used for the structural applications presented in Chapter 2 of this work and the tensile properties of these parameters are later evaluated in Chapter 4. Patel's work on the use of melting modes for predicting process parameter performance is also expanded upon in Chapter 3 of this work.

1.2 Thesis Outline

This thesis is organized into a total of six chapters, centered primarily around three pre-publication papers detailing the research that has been conducted for this thesis. Chapters 2, 3, and 4 are structured as journal papers with pertinent literature review and make up the main body of this work. Chapter 5 then presents a discussion of practical applications where this research has been applied. Finally, Chapter 6 provides the conclusions and recommendations for future work.

Chapter 2 discusses the design optimization of a key structural member for a rocket. In doing so, it presents a comparative case study between the performance of additively and conventionally manufactured structural members. A new methodology is presented for the use of AM in the design of high strength, lightweight structural members where buckling is a primary concern. The design is then experimentally tested using a novel fixed-end free-end buckling test fixture to validate the simulation results, showing a 98% performance improvement for the optimized design.

Chapter 3 addresses the optimization of downskin surface roughness. A new modeling approach for predicting the performance of downskin process parameters is presented and comparisons between the predicted and measured results are made. The interaction between core scanning power and near-surface porosity is discussed and, finally, a set of process parameters is recommended for the printing of AlSi10Mg at steep downskin angles with low surface roughness.

Chapter 4 investigates the tensile properties of as-printed AlSi10Mg. Using the process parameters identified in Chapter 3, the effect of part thickness and orientation on Young's modulus, yield strength, UTS, and elongation at break is investigated, along with the effect on surface roughness. The effect of overhang angle on the tensile properties of

thin structures is also explored. Finally, comparisons are made between as-printed and machined tensile coupons.

Lastly, Chapter 5 presents a discussion of some of the practical work that has been done based on the results of this research. This chapter includes a discussion on the design of additively manufactured components for a rocket engine turbopump, as well as the design of a liquid rocket engine injector and key rocket structural members. The injector and structural members are slated to fly on a rocket in August 2025 and all of these applications rely directly on the work presented in the previous chapters. A brief discussion is also presented on experimental work done for an industry partner looking to adopt this work for production.

Finally, Chapter 6 discusses the key conclusions of this thesis, with a particular focus on recommending areas of future studies that could improve upon the results presented in this work.

Chapter 2

Optimization of Rocket Structural Members via Additive Manufacturing

Abstract

In recent years, the use of additive manufacturing (AM) has seen increasing adoption across the aerospace industry for the manufacturing of brackets and other structural components of spacecraft. This can be attributed to the success of design for additive manufacturing (DfAM) techniques to optimize for performance while minimizing mass. Unfortunately, current DfAM approaches such as topology optimization are unable to effectively optimize parts which operate under compressive loading where buckling is a primary concern. In this work, a key structural member of a high-powered sounding rocket is used as a design case study for AM to demonstrate a new methodology for the design of lightweight members under compressive loading. Simulations were deployed to create a functionally graded hollow shell geometry based on the stress response of a solid beam design under specific weight constraints. The beam design was then augmented with internal

surface lattices to further prevent thin wall buckling. The final design was manufactured from AlSi10Mg using laser powder bed fusion and tested experimentally. To execute mechanical testing, a novel test fixture was designed and validated to allow fixed-end free-end buckling testing of the printed parts. The design exhibited even stress distribution and very high buckling resistance, demonstrating a 98% increase in strength compared to the conventional part design despite the two designs having equal mass.

2.1 Introduction

Metal Additive Manufacturing (AM) presents many new opportunities for improving the manufacturing of aerospace components, as AM allows for complex geometries that would not be practical or even possible with conventional manufacturing methods [8]. This creates a wide range of new design for additive manufacturing (DfAM) possibilities that can be leveraged when conceptualizing parts. For instance, part consolidation can be used to reduce manufacturing complexity and failure points, as well as size and weight reduction of assemblies by turning them into a single component [1], [18]. Geometry can also be optimized for the end-use application, while leveraging the degrees of freedom of the AM process to take advantage of methods such as latticing and topology optimization to create strong, lightweight parts [6], [7]. Many case studies have been presented on the usage of DfAM techniques to optimize various components and assemblies, with some case studies particularly focused on the aerospace sector [18], [19]. Case studies often showcase impressive results for weight savings or other benefits; however, these studies often do not comment on the design performance of the original design, the influence of material changes, or on any reductions in design performance due to lightweighting [20]–[22]. Other DfAM studies have used AM to develop novel designs such as aerospike rocket engines [23]

or compliant mechanisms for instrumented knee implants [24]. These types of applications highlight the possibilities introduced with AM, but without a conventionally manufactured equivalent, comparison of AM to conventional design solutions is made difficult.

The goal of this study is to consider the optimization of a key structural component in a rocket assembly that has been well designed based on conventional manufacturing constraints. This work will present a comparison between the conventional design and the DfAM optimized design to demonstrate how AM can be leveraged towards lightweighting and structural performance against compression loading and buckling. Laser powder bed fusion (LPBF) is considered as the metal AM technology of choice, as it provides excellent feature resolution [25] and tailored material properties [26], [27]. As such, LPBF has become on of the most widely adopted forms of metal AM.

2.2 Application Background

For this study, a key structural member of the Leviathan of the Sky rocket is considered[1]. Three structural members, known as longerons, transfer the thrust from the rocket's engine into the propellant tank and airframe. These longerons, shown in Figure 2.1, consist of a total of 7 parts. A primary strut machined from Aluminum 7075-T6 square stock is attached to a waterjet cut Aluminum 6061-T6 mounting tab at each end with a pair of #10-32 3/8" countersunk bolts. The maximum load applied to a single longeron is

[1]Leviathan of the Sky was a hybrid sounding rocket developed by the Waterloo Rocketry team for the 2023 Spaceport America Cup competition. The rocket had a mass of 57 kg when fully loaded and was 4.4 m in length. When tested, the system achieved a maximum altitude of 31,476 ft, with a maximum velocity of Mach 1.5 during its flight in June of 2023. More details about the rocket and the Waterloo Rocketry team can be found at: https://www.waterloorocketry.com/

estimated to be 12,209 N [28]. As a conservative assumption, the longeron is designed assuming fixed-free end conditions where one end of the longeron is assumed to be fully fixed and the end where load is applied is assumed to be fully unconstrained. This is important as the dominant failure mode for the longeron is buckling. Based on the Euler column formula presented in Equation 2.1, it can be seen that $P_cr[N]$, the critical force at which an ideal column will buckle is highly dependent on $L_{ef}[m]$, the effective length of the column based on the end-conditions [29]. The other terms in the equation are $E[Pa]$, the Young's modulus of the material, and $I[m^4]$, the second moment of area of the column cross-section. As shown in Figure 2.2, L_{ef} varies significantly based on the end-conditions.

$$P_{cr} = \frac{\pi^2 EI}{L_{ef}^2}[N] \tag{2.1}$$

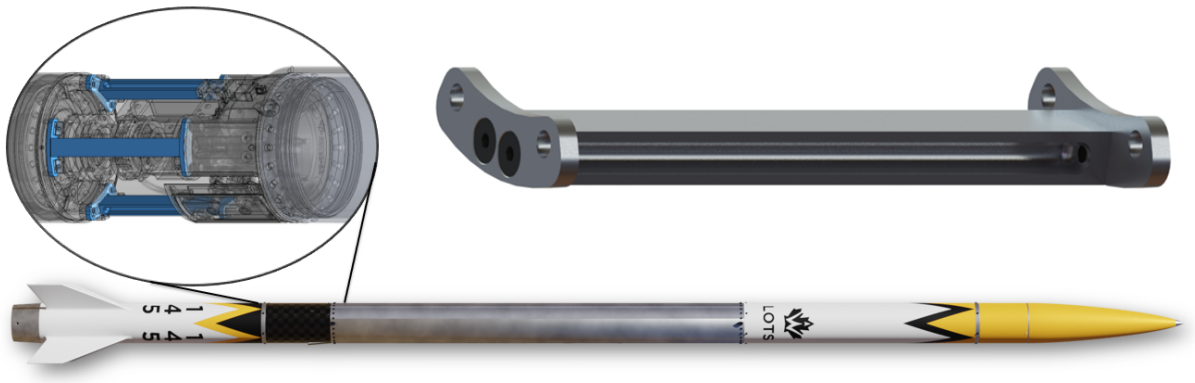


Figure 2.1: Location of longerons on the Leviathan of the Sky rocket and rendering of a longeron. Each longeron is comprised of a primary strut machined from Aluminum 7075-T6 square stock with a waterjet cut Aluminum 6061-T6 mounting tab attached at each end with a pair of #10-32 3/8" countersunk bolts.

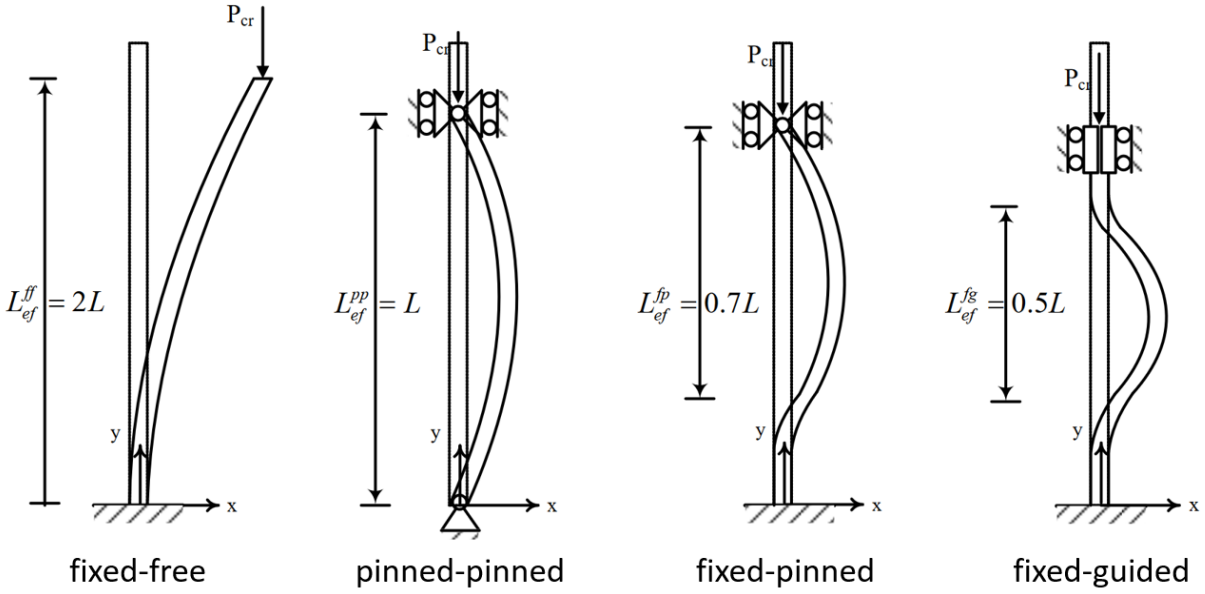


Figure 2.2: Effective length of columns based on end conditions. Column length - L, effective length - L_{ef}, critical load - P_{cr}. Adapted from [30].

The focus of this study is to re-design the longerons to be printed using LPBF. The objective is to keep the design mass constant while the design is optimized to increase the part strength as much as possible. Ultimately, this case study will demonstrate that, by taking advantage of the design flexibility provided by AM, material distribution can be optimized to create a stronger part for the given load case.

2.3 Materials and Methods

2.3.1 Printing Process

LPBF uses a high powered laser to selectively melt thin layers of metal powder together, layer by layer, to form solid metal parts. A diagram of the process is shown in Figure 2.3. LPBF is capable of producing parts with good dimensional accuracy and fine features. Depending on the material and process parameters used, very high densities exceeding those of cast parts can be achieved [31]. Strength is also comparable to or, in some cases, exceeds the bulk material properties of cast parts[12]. However, LPBF can present challenges due to residual stress buildup and steep overhangs that typically require support material [32], [33]. In addition, LPBF is often more expensive than traditional manufacturing methods and so is most worthwhile when it is used for capabilities not possible with traditional manufacturing, such as manufacturing extremely complex geometries or mass production of individually customized parts [5].

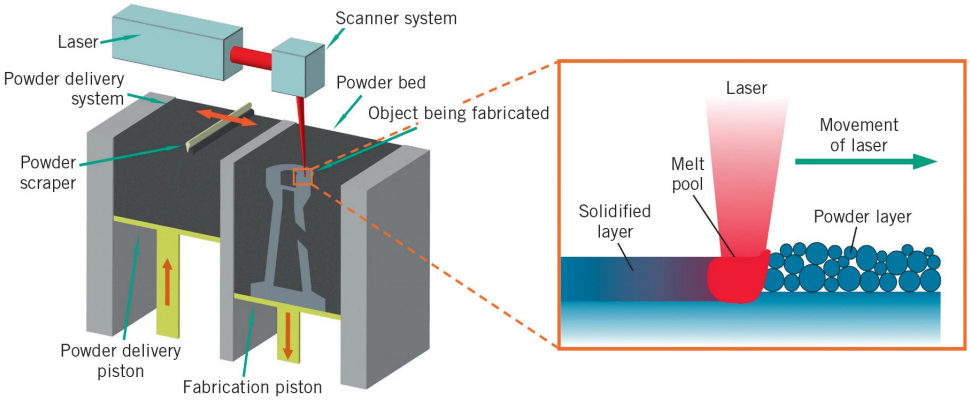


Figure 2.3: Processes diagram for Laser Powder Bed Fusion [34].

Powder and Machine

The longerons that were optimized for AM were printed using a modulated LPBF system (AM400, Renishaw, UK). The machine has a 400W ytterbium fibre laser and scans using point-by-point exposure. The optimized longerons were designed to be printed using AlSi10Mg. AlSi10Mg is one of the most widely available aluminum alloys for additive manufacturing and presents a balance of good mechanical properties with ease of crack free printing [35]. Plasma atomized pre-alloyed AlSi10Mg Powder (AP&C, Montreal, Canada) with a size distribution of 20-63 µm and a D50 of 45 µm was used in this work.

Process Parameters

Since parts were printed to target structural performance, it is critical that process parameters are selected to result in good density and strength. Parameters were selected based on the results of Patel et al. [26], who reported the use of a de-focused beam to achieve a part density over 99.98%. Parts were printed with a layer thickness of 30µm. A single sideskin border with a recipe based on Brock's work [15] was used as well as a single upskin layer and 4 downskin layers. The laser scanning parameters used are presented in Table 2.1.

Table 2.1: LPBF process parameters for part production. Laser power - P, beam radius - r_b, point distance - p_d, exposure time - t_e, hatch distance - h_d, effective laser power - P_{eff}, and effective velocity - v_{eff}. The drill delay time, t_d, is constant at 10 µs. A standard hatch angle rotation of 67° was deployed.

Region	P [W]	r_b [µm]	p_d [µm]	t_e [µs]	h_d [µm]	P_{eff} [W]	v_{eff} [mm/s]
Core	350	54	55	60	100	300	786
Sideskin	270	35	60	50	100	225	1000
Upskin	180	35	55	90	100	162	550
Downskin	125	90	70	70	100	109	875

Mechanical Properties Considerations for Simulations

At the time of writing, experimental data had not been collected for the mechanical properties of AlSi10Mg printed with the process parameters presented in Table 2.1. As such, the material properties were assumed to be similar to those published by a major LPBF machine producer using their standard process for the same layer height of 30 µm in the as-built condition. The key mechanical properties are presented in Table 2.2, along with the properties for the Al 7075-T6 bar stock which was used to machine the conventional longerons. Residual stresses from the printing process are a common concern in LPBF. It is common to heat treat parts after printing to reduce these residual stresses. However, the process of stress reliving AlSi10Mg parts significantly degrades the material yield strength by partially or fully annealing the material. As such, a second heat treatment is usually required to improve the yield strength. This heat treatment typically requires a fast water

quench and the resulting fast cooling rate makes parts susceptible to warping [36]–[38]. For this work, it was decided to leave parts in the as-printed state as it was deemed that the LPBF process results in good yield strength with no post-processing for this material system. The build plate layout was carefully considered to ensure that the design and print orientation minimized any residual stress build-up and is shown in Appendix A.1. In the as-printed state, there is anisotropy in the mechanical properties based on the printing direction [39], [40]. To simplify analysis and simulations, the material was assumed to be isotropic, with the lowest value taken as a conservative assumption.

Table 2.2: Assumed mechanical properties of as-printed AlSi10Mg and Al7075-T6 [41][40][42].

Property	AlSi10Mg As-Printed	Al7075-T6
Yield Strength	230 MPa	505 MPa
Ultimate Tensile Strength	450 MPa	570 MPa
Elongation at Break	6.3%	11%
Young's Modulus	70 GPa	72 GPa

2.3.2 Design Case Study Workflow

Design Constraints

The optimized longeron design must abide by the same design constraints as the original conventional design. It must mount within the same footprint using two 1/4"-28 bolts, as shown in Figure 2.4, and maintain the same length of 161 mm and mass of 84 g as the

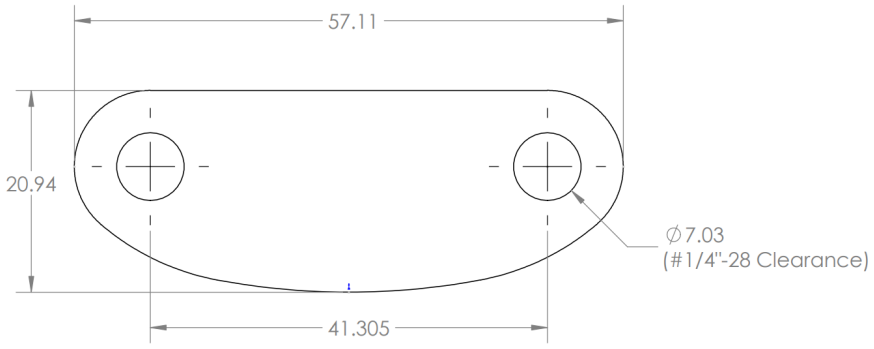


Figure 2.4: Maximum longeron footprint and required mounting hole locations. All dimensions in mm.

original design. The bolts thread into the bulkheads above and below the longerons, so tool access must be maintained for installation.

While AM allows for significantly more design freedom than most manufacturing methods, there are still limitations to what geometry can be printed. Some of the key design constraints are summarized as follows and were considered in the design process for this case study:

- **Overhang Angle**: Overhangs up to 45° typically print reliably with a reasonable surface finish. Overhangs between 45° and 30° are possible, but result in a significantly degraded surface finish, and overhangs beyond this angle are only possible under specific process parameter selection and laser scanning conditions (beyond the scope of the present work)[33], [43], [44].

- **Minimum Feature Size**: Minimum feature sizes are dependent on process parameters, but typically thin walls and pins should be at least 0.6 mm thick. Thinner features are possible for walls, but this is likely to result in degraded performance.

[32], [33].

- **Accuracy**: While highly dependent on the specific feature, tolerances of 0.1 mm are typically achievable as long as no significant part warpage occurs [33], [43].
- **Minimum material usage**: Large volumes of solid material are prone to high residual stresses, warping, and cracking and should be avoided [45].
- **Powder Removal**: Provisions must be made to ensure excess powder can be easily removed after the printing process. Any enclosed volumes must have de-powdering holes added to allow this [33].
- **Surface Finish**: LPBF can create acceptable surface finishes, with an S_a surface roughness typically around of 10-20 µm and no worse than 50 µm for most features. However for critical mating interfaces post-machining may be required [41], [44].
- **Supports and Removal**: When supports are required, considerations must be made to ensure they can be removed, and any required post machining of the resulting rough surface can be accomplished.
- **Part Removal**: Parts may be printed fully welded onto the build plate; as such, they must be cut free. This is typically done using a horizontal bandsaw or electrical discharge machining (EDM), with EDM giving a significantly better resulting surface finish and much thinner cuts. Excess material allowance to accommodate for part removal is required and dependent on the part removal process.
- **Part Orientation**: The print orientation of the part must be considered throughout the design process, as the print orientation affects overhangs, the required supports associated with overhangs, mechanical properties, and surface finish [41], [44].

Design Iterations and Justifications for Design Improvements

Ideally, the optimization of the printed design could be done using topology optimization. Unfortunately, despite significant research progress [46], most optimization tools are not capable of directly optimizing critical buckling load response. The buckling response of components designed via solid isotropic material with penalization (SIMP) topology optimization for compressive members is typically poor [46], [47].

Therefore, a manual iteration approach towards geometry optimization was deployed in this work. Design work was done first using a conventional CAD design tool (SolidWorks, Dassault Systemes, France) to create the initial geometry. Design refinements and simulations were then done iteratively using a dedicated DfAM software package (nTop, NY, USA). For comparison of designs, both static stress analysis and linear buckling analysis were used to assess and contrast the stress in the parts (conventional design and DfAM design) as well as the buckling resistance. Linear buckling analysis is known to over-predict actual part strength but is effective for comparing designs and predicting buckling modes [48], [49]. The result of the simulation is the so-called Buckling Load Factor (BLF), which is the theoretical safety factor for the idealized elastic part. Based on previous work [47], shell-lattice designs have been shown to be highly effective for creating lightweight yet highly rigid structures. The outer shell works to take the majority of the load and provides excellent buckling resistance. However, this thin shell is prone to surface buckling, thus a lattice was used in this work to provide additional stiffness to the shell.

Iteration 1

The I-beam profile of the conventional design was replaced with the largest volume that would fit in the design space and this was shelled with a wall thickness of 1 mm. A Body Centered Cubic (BCC) lattice with a cell size of 7.5 mm and a 1.25 mm strut

thickness was then used to fill the volume. The resulting Iteration 1 is shown in Figure 2.5a. Finite Element Analysis (FEA) was then conducted on the latticed design using the DfAM software package (nTop, NY, USA). An adaptively sized tetrahedral mesh was used with a maximum edge length of 1 mm and a feature tolerance of 0.25 mm. Load distribution blocks 1" x 1.5" x 3" in size with an edge length of 2 mm were simulated at either end of the longeron to provide a more representative force distribution into the longeron. The load was applied to the top face of the top block, and a fixed boundary condition was applied to the bottom face of the bottom block. The stress simulation and linear elastic buckling results are shown in Figure 2.6a and Figure 2.7a respectively. The Iteration 1 shell and latticed infill design approach provided superior buckling strength to the conventional design, but the stress distribution across the part was very uneven and there were very high stress concentrations at the corners where the mounting tabs meet the shell. In addition, Iteration 1 did not consider the the maximum overhang angle constraint for LPBF and would require a large amount of support material regardless of the print orientation.

Iteration 2

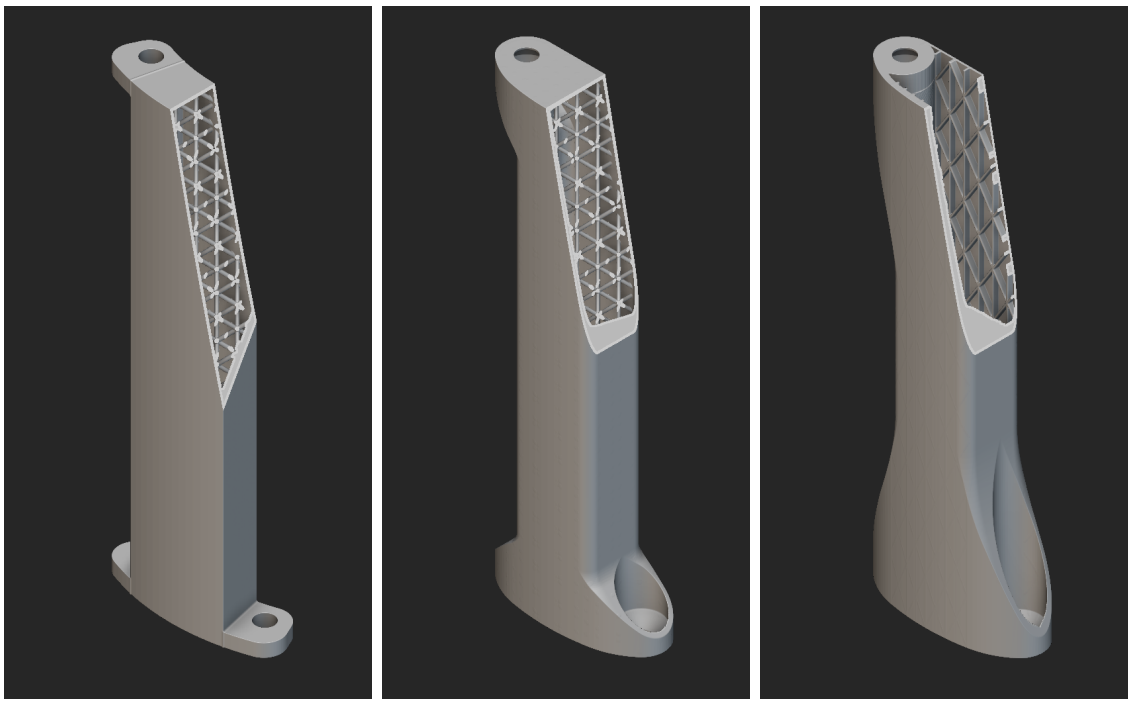
Iteration 2 considered printing the longeron vertically. This results in increased print times, but should significantly reduce the residual stress build-up, which tends to be an issue for long members printed horizontally [50], [51]. The vertical orientation is also optimal for part productivity as it allows for the highest number of parts to be nested on the build plate. To address the overhang angle constraint, the initial geometry was re-designed for Iteration 2 as shown in Figure 2.5b. By using countersunk screws for mounting the longeron and adding additional material around the bolt holes, the geometry of Iteration 2 is possible to print without supports.

To address the uneven stress distribution observed in Iteration 1, a functionally graded

shell was implemented to distribute material as needed. This was accomplished by running a stress simulation on the initial solid volume of Iteration 2 and mapping the results of that simulation to the shell thickness across the part. The resulting shell was set to 1 mm at the thinnest point and 3.3 mm at the thickest. The same 7.5 mm BCC lattice was retained but the strut thickness was reduced to 1.1 mm to give the desired final design mass of 84 g. The results for Iteration 2 show a significant improvement in buckling resistance over both the conventional design and Iteration 1, as well as a more even stress distribution than Iteration 1; however, the stress was still much higher than the conventional design. In addition, large stress concentrations were still observed in the corners near the fasteners of Iteration 2.

Iteration 3

For Iteration 3, the initial geometry was altered to have a much more gradual transition between the end profile with the mounting holes to the uniform profile along the middle of the longeron. The objective was to eliminate the stress concentrations observed for Iteration 2. Using the same functionally graded shell methodology as Iteration 2, the shell thickness for Iteration 3 was driven by a stress simulation of the initial Iteration 3 geometry. A minimum thickness of 0.7 mm was used for areas under 10 MPa in the initial stress simulation and a maximum possible thickness of 3.8 mm was used for areas above 50 MPa of stress in the initial simulation. It was observed that the stress was very low in the majority of the volume lattice structure used for Iteration 1 and Iteration 2, as shown in Figures 2.6a and 2.6b. However, the volume lattice used a large portion of the available mass. Therefore, for Iteration 3, the volume lattice was replaced with an isogrid surface lattice on the interior surfaces of the longeron. This fulfills the same role of stiffening the thin structure while requiring significantly less mass. The selected grid had a unit cell 16 mm tall and 10 mm wide. The isogrid was set to a constant 2mm depth, with a wall

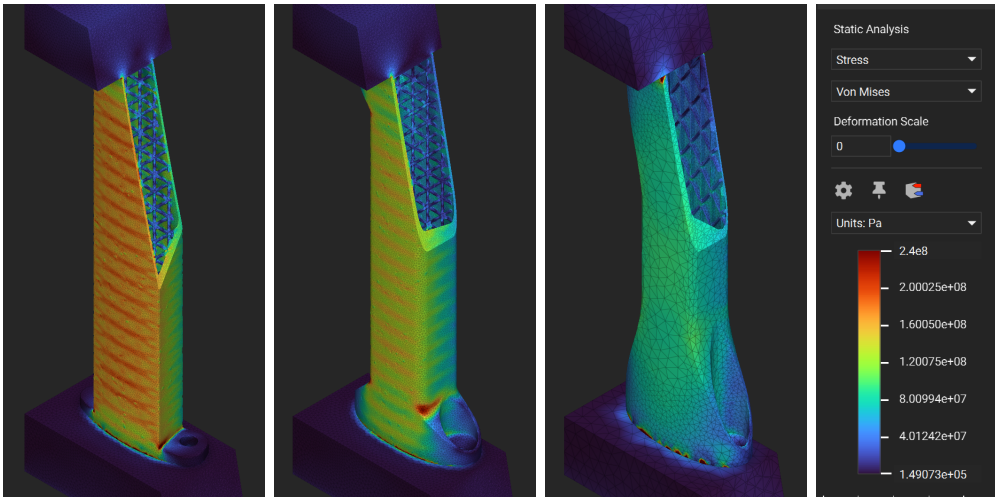


(a) (b) (c)

Figure 2.5: Design iterations: (a) Iteration 1: uniform lattice and shell (b) Iteration 2: graded shell with lattice and overhang considerations (c) Iteration 3: final design with surface lattices.

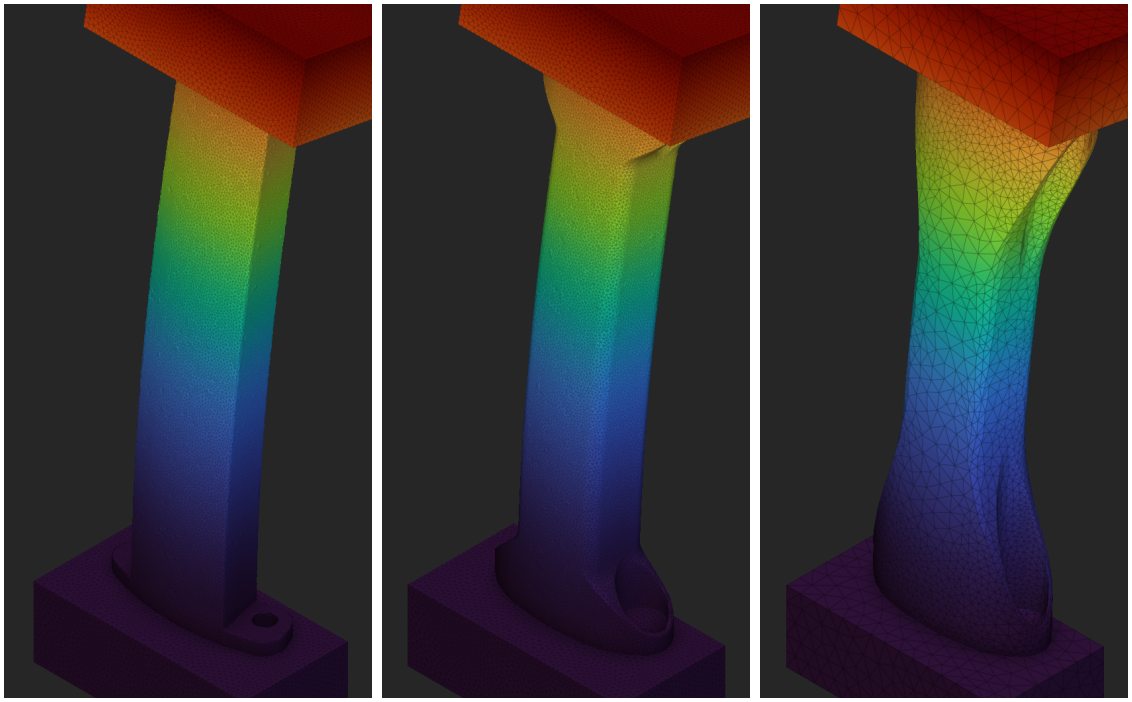
thickness of 0.7 mm.

The top and bottom surfaces of the shell used a significant amount of material but did not provide any meaningful structural benefit. In addition, they created issues with de-powdering and overhang angles. As such, they were removed from the Iteration 3 design to save material and doing so removed the last remaining printing challenges. A summary of the performance of each design iteration is provided in Table 2.3.



(a) (b) (c) (d)

Figure 2.6: Von Mises stress analysis results: (a) Iteration 1: stress distribution is high and uneven between front and back of the part (b) Iteration 2: stress distribution is better but still uneven. Significant stress concentrations at the corners of the part near the fastener locations. Stress on internal lattice is very low (c) Iteration 3: stress is much lower and stress distribution is fairly even across the part (d) Legend.



(a) (b) (c)

Figure 2.7: First buckling mode based on linear buckling simulations: (a) Iteration 1 (BLF = 1.66) (b) Iteration 2 (BLF = 3.21) (c) Iteration 3 (BLF = 3.64).

Table 2.3: Summary of design iteration performance.

Iteration	Mass	Buckling Factor	Maximum Stress
Conventional	84 g	1.09	135 MPa
Iteration 1	72 g	1.66	200 MPa
Iteration 2	84 g	3.21	170 MPa
Iteration 3	84 g	3.64	100 MPa

2.3.3 Validation and Testing Methodology

During the design of the optimized longeron, simple static stress analysis and linear buckling analysis were used to compare designs; however, it is known that linear buckling over-predicts the strength of components and is not a reliable method for determining the true strength of a part [52]. As such, additional work was required to determine the actual performance of the parts. Hand calculations were conducted to estimate the actual part strength and then non-linear displacement simulations were conducted to more accurately predict the failure loads. Finally, to demonstrate the real-world performance, the parts were experimentally tested to failure.

Validation - Hand Calculations

Hand calculations were used to estimate the strength of the longerons. For the conventional longeron, the standard Euler column formula, Equation 2.1, can be used. However, for the printed longeron (Iteration 3), the slenderness ratio is too low for the Euler column formula to give meaningful results. As such, Johnson's parabolic formula for intermediate length

columns is used, as presented in Equation 2.2 [29]. In this equation, $S_y[Pa]$ is the material's yield strength, and $k[m]$ is the radius of gyration, defined by $k = \sqrt{I/A}[m]$. Since the printed longeron has a complex geometry, the software used to optimize the longeron was used to compute its cross-sectional area, $A[m^2]$, and its second moment of inertia, $I[m^4]$ for the mid-plane cross-section of the part. It is important to note that the parabolic formula assumes a constant cross-section for the entire length of the column. This is not the case for the printed design; as such, it is assumed that there may be notable error in this calculation, but it still serves as a useful baseline to ensure simulation and testing results are reasonable.

$$P_{cr} = A(S_y - \left(\frac{S_y L_{ef}}{2\pi k}\right)^2 \frac{1}{E})[N] \tag{2.2}$$

Validation - Mechanical Testing and Custom Fixture Assemblies

Fixture Design

Based on a review of available literature, no systems have been found for destructive testing of members loaded in a fixed-free end constraint at the scale required for the longerons [53], [54]. A possible reason for the lack of fixtures for this loading condition is that it is well understood that equivalent results are achieved by testing a member double the length in a pinned-pinned end condition [29], [30]. This testing approach is simpler to achieve, as pinned attachments are a common test fixture. Unfortunately, the longerons have a non-uniform cross-section, so this approach is not appropriate. It may be possible to attach two longerons together, but the high cost of printing or machining the longerons means that this was not economical for testing multiple samples.

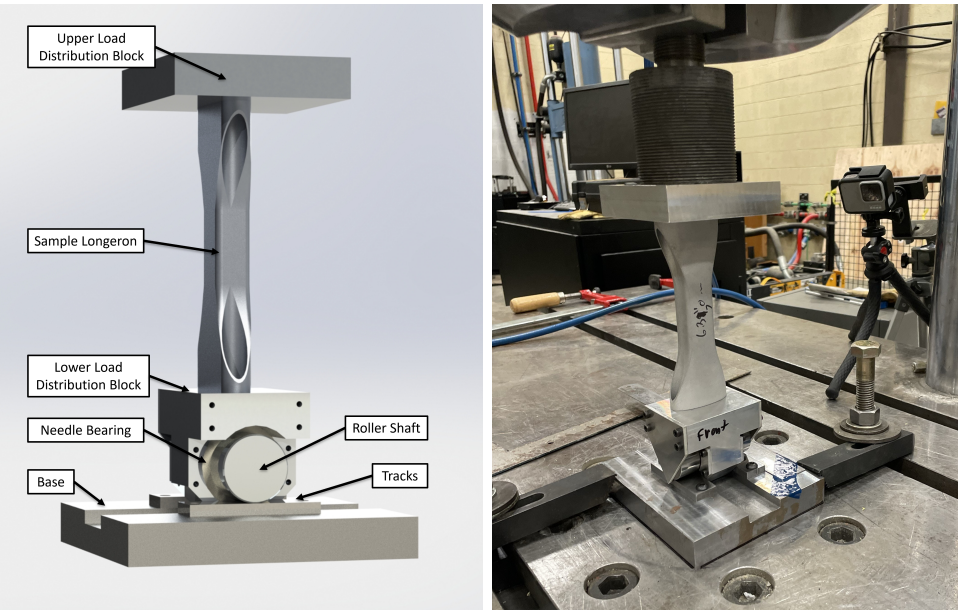
Therefore, a custom fixture was designed to facilitate fixed-free end compressive testing.

Free end conditions imply that the end of the member is fully free to move in all six degrees of freedom, which would necessitate a complex fixture. While linear buckling is not an accurate way to predict the exact buckling loads, it is an effective way to determine the buckling modes of a part. Based on simulations, it is known that the dominant buckling mode is simple bending along a known axis. This means that the test fixture only needs to support two degrees of freedom as the failure mode only occurs within a single plane.

A test fixture was designed using a bearing and roller system as shown in Figure 2.8. The longeron is bolted to load distribution blocks at both ends. These parts are made from 6061-T6 aluminum to minimize stress concentrations at the interface. The top load distribution block is fully constrained against the top of the load frame by friction. The lower load distribution block houses a large needle bearing with a static load rating of 86 kN. The bearing allows the lower load distribution block to rotate freely around a 1.5" diameter hardened steel shaft. This shaft is free to roll along a pair of AR500 hardened steel tracks which allows the shaft to roll freely without plastic deformation up to a maximum load of 39 kN. These tracks are mounted to a mild steel base which transfers load into the table of the test frame and is clamped in place using toe clamps.

Fixture Validation via Simulation Approaches

The chosen mechanical testing method is novel and not yet proven in literature. This method needed to be verified in simulation to understand if it would perform as intended before the experimental testing was deployed. A commercial FEA package (Ansys Inc, USA) was used to run a constant displacement rate simulation of the final Iteration 3 longeron and test fixture, as shown in Figure 2.9. A displacement rate of 0.01 mm/s was applied and the reaction force was measured. It was seen that the jig performed as expected with the load slowly increasing until a specific point at which the longeron buckled and the roller system suddenly shifted, indicating the load at which the longeron failed. This



(a) (b)

Figure 2.8: Test fixture: (a) Rendering with shaft cover removed (b) Fixture in test frame during test.

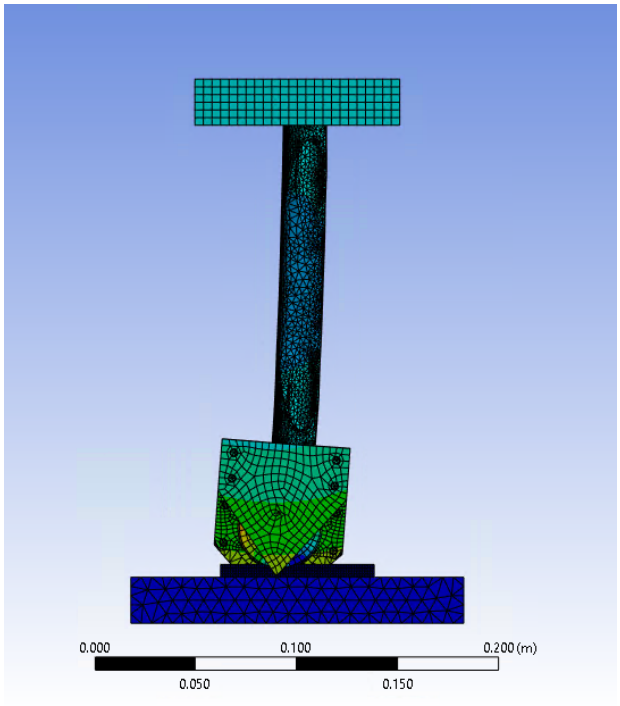


Figure 2.9: Constant displacement rate FEA simulation of the test fixture and longeron. Shown in the buckled state with deformation true to scale. Simulation was used to validate the fixture would perform as expected before manufacturing.

aligned closely with what was later observed in physical testing. The same simulation was also run with the conventional longeron to enable comparison between the simulation results.

Fixture Validation via Experimental Approaches

Before testing the expensive conventional and AM samples, it was desired to verify that the testing setup performed as expected. In order to do so, a simple strut made from aluminum angle extrusion was designed to allow multiple tests to be run at low-cost. These samples where cut from 1" x 1/8" 6061 aluminum angle and machined to length. Mounting

plates made from 5052 aluminum were then waterjet cut and lightly press-fit onto the ends of the samples. One of the fixture validation samples is shown in Figure 2.10.

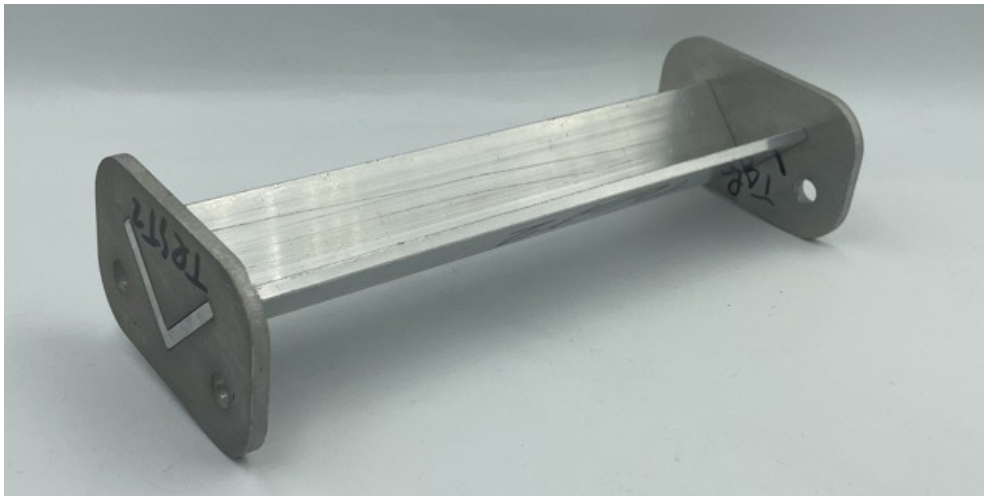


Figure 2.10: Low cost test fixture validation sample manufactured from 1" aluminum angle stock with waterjet cut mounting plates press-fit to each end. Used for experimental validation of the test fixture.

Mechanical Testing

Samples were tested using a tensile/compressive test frame with a 100 kN load cell (MTS Series 322, MTS Systems, Minnesota, USA). To test a sample, the specimen was first bolted into the top and bottom load distribution blocks, and the roller was placed on the tracks. The fixture was designed such that a pair of standard 1-2-3 blocks could be used to center the roller in the middle of the fixture base and the system could then be clamped in place such that it could not move. The head of the test frame was then lowered and an initial pre-load of 0.5 kN was applied. The alignment of the fixture was verified and the clamps were removed such that the roller system was free to move. The test was then completed at a fixed displacement rate of 0.01 mm/s. The test was manually

terminated once it was observed that the sample had buckled, and the reaction force had began to decrease, indicating that the part had failed. The alignment setup using 1-2-3 blocks is pictured in Appendix A.2.

2.4 Results and Discussion

2.4.1 Test Samples

Three samples of the optimized AM design were printed using the process described in Section 2.3.1. The samples were EDM cut from the build plate and media blasted to improve their surface finish. While the EDM cut face of the samples had excellent surface finish and alignment, it was observed after the first test that the as-printed top faces of the printed longerons were somewhat rough and led to poor alignment in the test fixture. As such, the top face of the longerons was post-machined on a manual mill and approximately 0.2 mm of material was removed, significantly improving the surface finish and alignment. A total of four conventional samples were available for testing, three of which had flown on the rocket, but were inspected to ensure they still met the design specification, and one spare which had not seen service. In addition, three validation samples were machined for confirming the performance of the test fixture. Both the conventional and printed samples were weighed using a high precision scale (Secura 224-1S, Sartorius, Germany) and their masses can be seen in Table 2.4.

Table 2.4: Mass of printed and conventional samples.

Sample	Conventional	Printed
Sample 1	82.97	83.48 g
Sample 2	83.27 g	84.07 g
Sample 3	85.86 g	84.49 g
Sample 4	83.31 g	N/A
Average	83.85 g	84.01 g

2.4.2 Test Results

Testing was split across two sessions. In the first session, the three validation samples were tested using the test fixture. It was confirmed that they were generating reasonable data and that buckling occurred as expected, with no visible deformation until the sudden onset of buckling and the roller system shifting. Once the efficacy of the experimental fixture was confirmed, one of the conventional samples and one of the printed samples were tested in sequence. The first printed sample gave a lower strength than expected based on the simulation results. Upon further inspection, it was found that the as-printed top surface of the sample resulted in a slight misalignment of the fixture. To resolve the misalignment, the top face of each sample was post-machined as previously described which fixed this issue. In addition, it was observed that, due to the design of the test fixture and the nature of a fixed-displacement rate test, it appeared that only elastic deformation occurred during buckling. Since no plastic deformation could be measured on the sample after the test, it was decided that samples could be re-tested to gather additional data. During the second testing session, the remaining conventional and printed samples were tested. During the experiments, it was found that, in some cases, the fixture's roller system

could bind if not properly lubricated or if misaligned. This essentially resulted in the end conditions switching from fixed-free to fixed-pinned. This caused the samples to withstand a significantly higher force before finally buckling with significant plastic deformation. The problem was mostly resolved via careful lubrication and alignment of the fixture before each test, but this issue resulted in outlying data for one of the printed samples and two of the conventional samples. The complete testing data including the validation and outlying samples are presented in Appendix A.3. The results for the successful conventional and printed sample tests are presented in Figure 2.11.

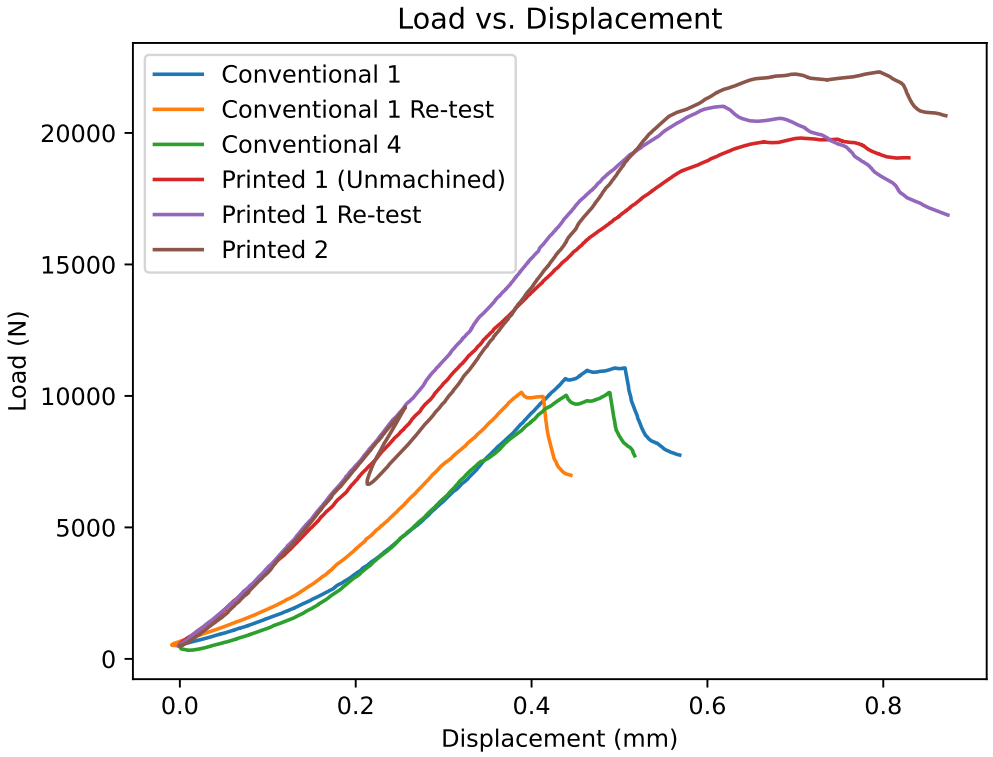


Figure 2.11: Experimental test results for conventional and printed longerons. Failure load is considered to be the maximum measured force. All printed longerons significantly outperform the conventional longerons.

2.4.3 Comparison of Design Performance

The estimated strength of the conventional and printed longerons are presented in Figure 2.12 for each of the validation methods used: hand calculations using the the Euler and Johnson equations discussed in Section 2.3.3, fixed displacement rate simulations of the entire test fixture, and experimental testing. It can be seen that there are considerable

variations between the estimated critical load from the hand calculations vs. the simulations, particularly for the conventional samples. However, the simulation results align reasonably well with the experimental test results. The discrepancy between the hand calculations vs. the simulation and test results may be due to the assumption of ideal end conditions in the hand calculations. It is likely that the mounting tabs used to mount the longeron have some impact on the overall stiffness of the structure compared to ideal end conditions. In addition, since the test fixture is of a novel design, it is not definitively known how accurately it models ideal fixed-free end conditions. It is also likely that the additional length required for the fixture mechanism may influence the effective buckling length of the total structure, potentially reducing the buckling strength compared to an ideal scenario. Finally, while efforts were made to ensure the best possible alignment of the fixture, the exact degree to which eccentric loading may have been applied is unknown and this may affect the resulting measured strength.

While there are a number of factors that make it difficult to determine the exact strength of the conventional and printed longeron designs, it can be seen that across every evaluation method, the printed longeron design substantially outperforms the conventional design. Based on the average destructive testing result, the printed design is 98±14% stronger than the conventional design for the same mass, despite AlSi10Mg having a significantly lower yield strength than Al 7075-T6. This highlights how, for some applications, the design freedoms enabled by AM may alow for significant performance improvements in the design of structural components.

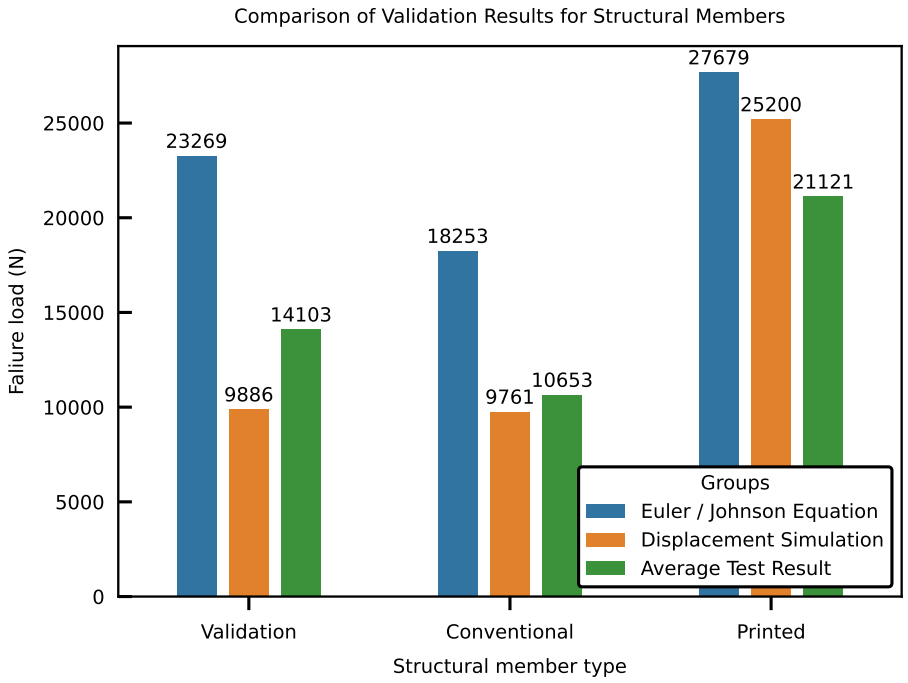


Figure 2.12: Comparison of performance for different validation methods. Euler and Johnson calculations give equivalent results, with the appropriate method being used based on the slenderness ratio of each design as discussed in Section 2.3.3. The performance increase of the printed design over the conventional design is significant for every assessment method.

2.5 Conclusions

In this work, metal AM was used to redesign a conventionally manufactured structural member with the objective of significantly improving its strength via design optimization. The optimized members were then printed using LPBF and a test fixture was developed to conduct destructive testing of both the conventional and printed designs. The key findings of this work are summarized below:

1. The use of AM can result in significant improvement in structural part performance under certain load cases by enabling the design of geometry that is optimized for the load case and is not limited by the manufacturability requirements of conventional manufacturing. Specifically, it was possible to re-design a longeron such that the optimized design achieved 198±14% the strength of the conventional design for the same mass based on experimental testing.

2. At present, commercially available topology optimization software packages do not feature tools capable of topology optimization for buckling resistance. Instead, a manual iteration approach must still be used to generate an optimal initial geometry. As such, there is a need for better optimization methods for designs where buckling is a key factor to enable rapid design optimization of these types of structures. In addition, while methods such as the use of surface lattices to prevent buckling in shelled structures were highly effective in this case study, more work is required to develop broadly applicable workflows for the design of these types of lightweight structures.

3. A test fixture was developed to allow the testing of structural members under fixed-free end buckling. The fixture was proven to be effective for enabling the comparison

of different designs via real-world destructive testing. However, some further refinements are required to ensure the reliability of the test fixture. In addition, more characterization work is required to determine how accurately it models fixed-free end conditions, and refinements may be required to improve its accuracy.

This work focused specifically on the possibilities of AM for the design of structural components at the part level. Even further optimization is possible when entire assemblies are considered for design optimization, and when factors such as fluid systems and thermal management are included in the optimization process.

Chapter 3

Optimization of Downskin Surface Roughness for AlSi10Mg Structures Printed using Laser Powder Bed Fusion

Abstract

In this work, the downskin surface roughness of parts printed using LPBF is considered. A number of process parameter combinations are tested across downskin angles ranging from 75° to as low as 20° to identity process parameters that enable the printing of AlSi10Mg at low downskin angles with good surface roughness. To aid in this work, a novel method is proposed for modeling the behavior of downskin. The proposed approach allows the adaptation of an analytical model developed for predicting melt pool geometry in the core of a part to allow its use for predicting downskin performance. This method

is used to predict the performance of downskin process parameters before printing and a close alignment is found between process parameters which are predicted to be effective and the experimentally measured roughness. The effect of sample thickness and core process parameters on downskin roughness is investigated and CT scanning is used to explore the relationship between core power and near-surface porosity at steep downskin angles. Finally, a set of process parameters are identified which enable the printing of parts as low as 20° while achieving a significantly lower surface roughness than what has been published by industry.

3.1 Introduction

In recent years, metal additive manufacturing (AM) has seen a significant uptake in usage across the aerospace sector [55]. Of the available metal AM technologies, laser powder bed fusion (LPBF) has been of particular interest due to its ability to produce full density parts with excellent feature resolution [1].

Use cases of LPBF in aerospace have been particularly focused on engine components and other high temperature, high performance systems which require the usage of material classes such as titanium and nickel super alloys [1], [56]. This may be attributed to two main factors. The first is that while LPBF has certain limitations, it provides excellent design freedom, enabling easier manufacturing of parts with complex fluid manifolds and other difficult geometry[10]. The second reason to select LPBF for manufacturing is that the titanium and nickel alloys used in aerospace tend to have extremely poor machinability, making conventional manufacturing expensive and increasing the economic viability of using LPBF [5], [57], [58].

In comparison, aluminum alloys, in conjunction with LPBF, have seen an emerging

but limited adoption in the aerospace industry [1], [59]. While there may be a number of reasons for this, low adoption in LPBF can be partially attributed to the ease of machining for aluminum alloys [60]. Since aluminum alloys are easier to machine and therefore cheaper to turnaround into products when compared to LPBF, there is less economic incentive to manufacture aluminum parts using the more expensive approach. To justify printing a part from aluminum alloys, there must be significant value added to balance the added expense [5]. As such, aluminum parts in particular should look to leverage DfAM techniques such as topology optimization, part consolidation, and latticing to create components that can significantly outperform their conventional machined counterparts.

While LPBF allows for a significant amount of design freedom, one significant downside is the inability to print structures with steep overhangs (surfaces facing downwards with respect to the build plate) without supports [32]. Even when an overhang can be printed, the surface often exhibits significantly degraded finish [61]. These surfaces, referred to as downskin, typically have surface roughness characteristics multiple times poorer than that of sideskin (surfaces perpendicular to the build plate) or upskin (surfaces facing upwards away from the build plate). Figure 3.1 depicts the different types of surfaces based on angle of inclination with respect to the build plate. When creating complex designs for LPBF, poor downskin and the requirement for support material at low angles can pose significant challenges to designers and requires design tradeoffs that reduce part performance [18]. As such, there is significant value if process parameters can be identified which improve downskin roughness and allow geometry with steeper downskin angles.

This work aims to identify process parameters which enable the manufacturing of aluminum alloy (AlSi10Mg) parts with reduced downskin roughness (compared to literature [41], [62]) and steeper downskin angles (supportless down to 20°, which is well below the standard 45° minimum [32], [44]). Traditional high-strength aluminum alloys used in

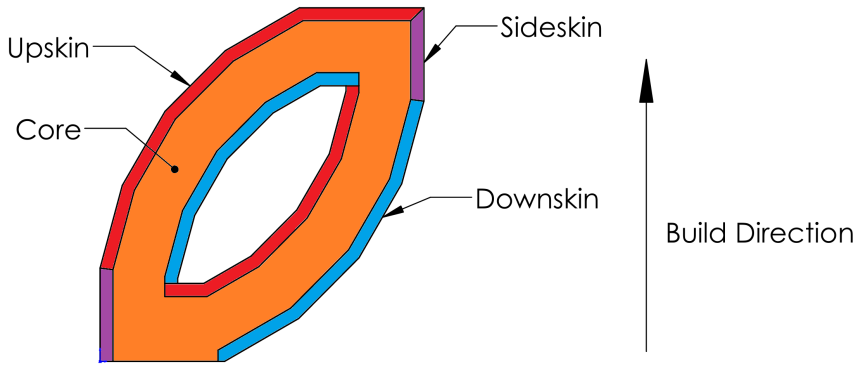


Figure 3.1: Demonstration part showing downskin surfaces in blue, sideskin surfaces in purple, and upskin surfaces in red, as well as the part core in orange. The build direction is orthogonal to the plane of the build plate.

aerospace such as 6061 and 7075 are highly prone to cracking during the LPBF process [63], [64]. For this reason, a number of alloys have been adapted or developed for LPBF which are significantly less prone to cracking, such as Al-Sc alloys for high strength applications [65]. Another class of alloys that is typical for LPBF is AlSi10Mg. AlSi10Mg was selected as the alloy of choice for this work as it provides reasonably good material properties and is one of the most widely adopted aluminum alloys for LPBF [13].

To enable better comparison and prediction of downskin process parameter performance, a novel method for modeling the behavior of downskin is presented herein. The proposed approach allows the adaptation of an analytical model developed for predicting the melt pool geometry in the core of the part (with solid material as the substrate boundary condition) [66] to allow its use for predicting downskin performance (under the assumption that the boundary condition changes gradually from solid to powder). Using this method and previous data on optimized sideskin parameters[15], an experiment is designed to determine a set of process parameters which alow for the printing of AlSi10Mg

with significantly improved surface roughness and at steeper downskin angles down to 20°.

3.2 Materials and Methods

3.2.1 Printing Process

Parts were printed using plasma atomized AlSi10Mg powder (AP&C, Montreal, Canada) with a size distribution of D10-D90 of 20-63 µm and a D50 of 45 µm [15]. Printing was conducted with a modulated LPBF system (AM400, Renishaw, UK). The system features a soft silicone recoater which allows a greater tolerance against in-situ part warpage or spatter. All parts used a nominal layer thickness of 35 µm with a hatch rotation angle of 67° between each layer. Two border scans were used for sideskin and five downskin layers were used, with downskin scanning being activated at angles of 45° or less. Scanning was completed in the following order: core hatching, downskin hatching, sideskin border, downskin border. A reduced build volume (RBV) system was used to reduce the amount of powder required for the build. Since the system uses a modulated beam, the effective power, $P_{eff}[W]$ and effective velocity $v_{eff}[m/s]$ are given by Equation 3.1 and Equation 3.2 respectively, where $P[W]$ is the laser power, $t_e[\mu s]$ is the exposure time, $t_d[\mu s]$ is the drill delay time, and $p_d[\mu m]$ is the point distance.

$$P_{eff} = P\frac{t_e}{t_e + t_d}[W] \tag{3.1}$$

$$v_{eff} = \frac{p_d}{t_e + t_d}\left[\frac{m}{s}\right] \tag{3.2}$$

3.2.2 Modeling

Significant research has been conducted on the development of analytical models for accurate prediction of various LPBF process outcomes[67]. Generally, models present significant value in allowing the prediction of process performance, enabling intelligent choice of experiment process parameters by focusing on combinations that are likely to succeed in achieving specific targets (density, microstructure, etc.)[68]. Since most work is focused on the physics of the laser-material interaction in the core of a part (where boundary conditions assume a solid substrate), including the models adopted in this work [66], [69], a method is presented to re-frame any such an analytical model for use in the development of downskin processes parameters with reasonable performance outcomes.

Keyhole Number

One useful tool in the prediction of process parameter performance is the dimensionless keyhole number, Ke, originally developed by Gan et al. [69] and defined by Equation 3.3.

$$Ke = \frac{AP_{eff}}{\pi\rho C_p(T_m - T_0)\sqrt{\alpha v_{eff} r_b^3}} \tag{3.3}$$

With the variables being absorptivity, A, effective power, $P_{eff}[W]$, density, $\rho[kg/m^3]$, heat capacity, $C_p[J/(kgK)]$, liquidus temperature, $T_m[K]$, substrate temperature, $T_0[K]$, assumed to be ambient (293 K) in this work, thermal diffusivity, $\alpha[m^2/s]$, effective scan speed, $v_{eff}[m/s]$, and laser beam radius, $r_b[m]$. The objective of the keyhole number is to predict the melting mode of any given set of process parameters. A set of threshold values are used to determine whether the process parameters will result in conduction, transition, or keyhole melting modes given the keyhole number. However, Patel et al.

identified that the original thresholds proposed by Gan et al. did not hold well against experimental results for AlSi10Mg [26]. Patel et al. demonstrated that keyhole numbers below 12 represent process parameters which result in conduction mode melting, while keyhole numbers between 12 and 20 result in transition mode melting, and keyhole numbers above 20 result in unstable keyhole melting modes. In the conduction mode, power density is relatively low and conduction is the main mechanism by which heat transfers through the melt pool and into the surrounding material. This typically results in a stable semi-circular melt pool, with very low levels of material vaporization. In the keyhole mode, high power density leads to high levels of vaporization. This results in a deep cavity of vapor in the melt pool with the depth largely driven by the recoil momentum of the vaporizing material and convection being the primary heat transfer mechanism. Strong keyholing can result in an unstable melt pool which causes bubbles of gas to get entrained in the melt pool. As the melt pool solidifies these bubbles become permanently trapped in the part, resulting in porosity. The transition mode lies between the conduction and keyhole modes with heat transfer being a combination of conduction and convection. Since vaporization is only moderate, the melt pool is typically stable [26], [70]. As such, it is typically desirable to ensure process parameters result in conduction or transition melting modes. The keyhole number approach was utilized as a screening method for experimental planning of process parameter combinations.

Thermophysical Melt Pool Model

In addition, an analytical melt pool simulation model which has been previously reported [15], [71] is used for the prediction of melt pool size and shape for a given set of process parameters. The model is adapted from the work of Rubenchik et al. [66] and is based on an analytical solution for the temperature field of a 3D Gaussian moving heat source on a

semi-infinite plane. By solving for the point at which the temperature exceeds the melting point of the material, the melt pool dimensions can be predicted. The model is implemented as MATLAB code and requires the material properties presented in Table 3.1, as well as the process parameters presented later in this work as inputs. Based on the simulated melt pool size a number of useful metrics can be evaluated to predict the performance of process parameters. One important predictor of porosity is the ratio between the melt depth and the nominal layer height, as observed in several works [72]–[74]. This melt depth ratio (MDR) is defined by Equation 3.4, where l is the nominal layer height, and d_{melt} is the melt pool depth at the minimum depth between melt pools as shown in Figure 3.2 [71].

Table 3.1: Properties of AlSi10Mg used for process modeling [15], [26].

Properties	**Material(AlSi10Mg)**
Thermal conductivity, K [W/(mK)]	113
Density, ρ [kg/m^3]	2685
Specific heat capacity, C_p [J/(kgK)]	963
Melting temperature, T_m [K]	863
Vaporization temperature, T_v [K]	2740
Thermal diffusivity, α [m^2/s]	4.37×10^{-5}
Absorptivity, A	0.25
Powder particle size, D_{50} [μm]	45
Powder bed relative density, R_{powder}	0.46

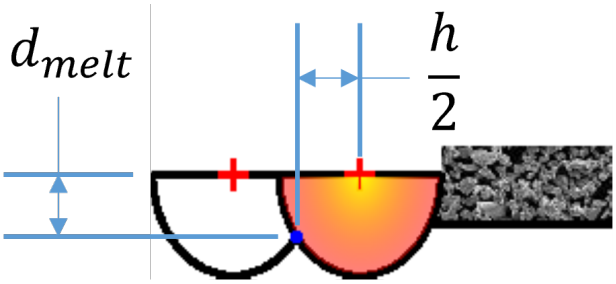


Figure 3.2: Critical melt depth location for MDR, based on hatch spacing, h [71].

$$MDR = \frac{d_{melt}}{l} \tag{3.4}$$

For AlSi10Mg, it has been shown that an MDR of 1.5 results in significant porosity, while good results can be acheived at an MDR of 2 [15]. As such, an MDR of 1.75 is considered the lower bound for a potentially acceptable set of process parameters. Similarly, it has been found that beyond an MDR of 2.5, no improvement is observed in part density, while energy input continues to increase. Therefore an MDR of 2.5 is selected as the upper bound in this work [15], [75].

The Melt Pool Overlap Model

While the presented models are useful tools in predicting process performance, they are focused on predicting the performance of the bulk printing process when scanning at the core of the part and are developed and verified under that assumption. As such, they do not inherently account for the differences in process mechanics encountered while printing in the downskin region of the part. In order to enable the use of these models for predicting the performance of downskin process parameters, a model is proposed to determine the effective material properties while printing downskin. The objective is that by determining

the effective properties relative to core printing, they can be input into these and other models to help predict the performance of new downskin process parameters.

Two primary differences are identified between printing in the core region and printing in the downskin region. The first is the difference in density of the substrate material being melted. When printing over solid material, there is significant re-melting of the layers below the current layer of powder. When printing in the downskin region, there is less solid material below the instantaneous melt pool and an increased amount of loose powder in the substrate. Since loose powder has a much lower density than solid material, this results in an overall decrease in the density and thermal conductivity of the material being melted [76].

The second is that, when printing in the core region, the majority of the melt pool is in direct contact with the solid part below and the previously-melted track beside it. This results in rapid cooling of the melt pool, as heat is conducted into the surrounding solid part. While printing in the downskin region, a greater portion of the melt pool is in contact with loose powder, particularly in the underlying layer, which has a much lower thermal conductivity, less than 1% of solid AlSi10Mg [76]–[78], resulting in much slower cooling of the melt pool.

To account for the changes in density and thermal conductivity, a proposed model is implemented, whereby an idealized melt pool is considered with an aspect ratio of 0.5, a depth 3 times the nominal layer height, and a hatch distance 3.3 times the nominal layer height. This assumption is based on measurements previously reported in literature for focused beam AlSi10Mg process parameters [26]. The density of the material in the melt pool is assumed to be proportional to the solid fraction of the melt pool, which is the amount of solid material vs powder overlapped by the melt pool. The thermal conductivity is assumed to be proportional to how much of the melt pool border is in contact with solid

material vs loose powder. Since the complex geometry introduced by overlapping melt pools cannot easily be expressed as a function, the model was manually computed by designing the melt pools using parametric CAD software (SolidWorks, Dassault Systemes, France) and measuring the border length and overlap areas at each downskin angle. The geometry for 90° (sideskin) and 20° (steep downskin) are presented in Figure 3.3. For angles greater than 90° (upskin) or core printing there is no change in the overlap or border length values compared to the 90° case. This means that the model predicts no difference between sideskin, upskin, and core printing. As such, the results for solid fraction and conductivity are normalized against the measurements of the 90° case to enable compatibility with the previously discussed models. Figure 3.4 shows the relative solid fraction, R_{sf}, and relative conductivity, R_K, as a function of downskin angle based on the overlap model. Since the thermal conductivity of powder is so low, its contribution to cooling is neglected and the effective thermal conductivity, K_{eff} can be approximated using Equation 3.5. While the density of powder is much lower than solid material, it is still significant. As such, the effective density, ρ_{eff} can be approximated using Equation 3.6, where R_{powder} is the relative density of the powder bed.

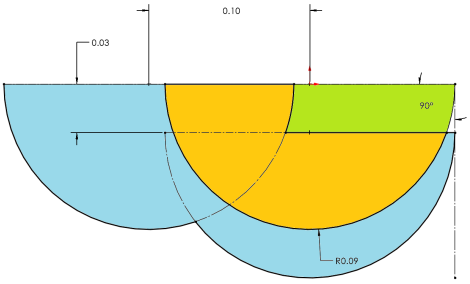
$$K_{eff} = R_K * K \left[\frac{W}{mK}\right] \tag{3.5}$$

$$\rho_{eff} = \rho(R_{sf} + (1 - R_{sf}) * R_{powder}) \left[\frac{kg}{m^3}\right] \tag{3.6}$$

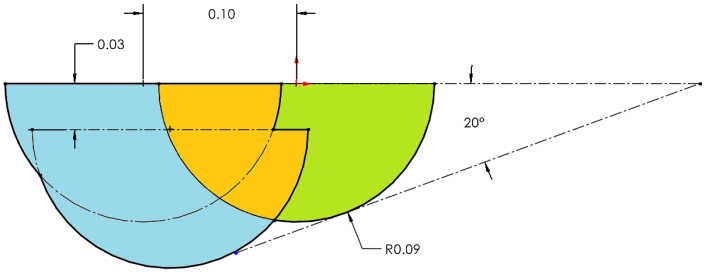
Thermal diffusivity, α, is a derived property based on thermal conductivity, density, and specific heat capacity, C_p. As such, it is dependent on the downskin angle. The effective thermal diffusivity, α_{eff}, can be approximated using Equation 3.7.

$$\alpha_{eff} = \frac{K_{eff}}{\rho_{eff} C_p} \left[\frac{m^2}{s}\right] \tag{3.7}$$

These estimated effective material properties can then be used in the previously discussed models to predict the performance of any set of process parameters at any given angle; as will be explained later in this work. The detailed numerical values used are presented in Appendix B.1.



(a)



(b)

Figure 3.3: Graphical diagram of the melt pool overlap model at two different angles. The meltpool is represented by the orange and green areas, while the solid part is shown in blue. Solid fraction is the amount of re-melted part (orange) vs fresh powder (green) in the melt pool. Conductivity is assumed proportional to the length of the melt pool border contacting the solid part (the border between the blue and orange areas): (a) 90° sideskin printing: most of the meltpool is dense, re-melted part and there is high conductivity to the surrounding solid part. (b) 20° downskin printing: most of the meltpool is less dense fresh powder and there is much less contact with the solid part for heat to conduct away.

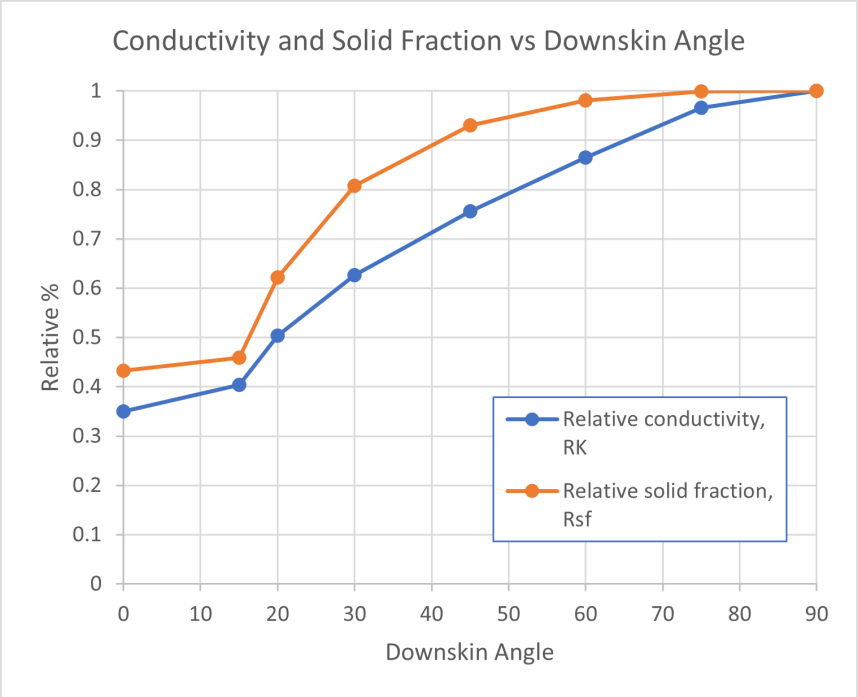


Figure 3.4: Relative material conductivity and solid fraction based on melt pool overlap model. Numerical values provided in Appendix B.1.

Volumetric Energy Density

Volumetric energy density (VED) is a commonly used metric for describing the amount of energy input into a material; as such, VED is used evaluate the performance of LPBF process parameters [79]. VED can be defined by Equation 3.8, although some other works use the beam diameter instead of hatch distance [15], [80]. It is important to note that this VED approach does not take into account material properties. While there are limitations to its usefulness as a single parameter to predict process performance, it is a useful tool when combined with other metrics [80].

$$VED = \frac{P_{eff}}{v_{eff} h l} \left[\frac{J}{mm^3} \right] \tag{3.8}$$

3.2.3 Test Sample Geometry

Three different test sample geometries were used to evaluate the surface roughness performance of various process parameters, as shown in Figure 3.5. The first is a thick facet geometry that has been used previously by Rogalsky et al. [71]. It has a wall thickness of 3 mm and provides downskin and upskin angles of 30°, 45°, 60°, and 75°, as well as sideskin. In addition, the same facet design was printed with a wall thickness of 1 mm to investigate if part thickness has a significant effect on surface roughness. To enable the testing of downskin angles as low as 20°, dedicated 20° samples were printed since the likelihood of print failure at this angle is much higher. Based on the available space, ten of each type of sample could be fit in the RBV, allowing ten different combinations of process parameters to be tested. Figure 3.6 shows the build layout of the samples on the RBV.

3.2.4 Process Parameter Selection

A total of seven different sets of process parameters (also referred to as recipes) were used in this work, as summarized in Table 3.2. Process codes # 1 through # 3 operate at the limit of the LPBF system's power and velocity capabilities and are based on previous work which is included in Appendix B.2 and literature [81], [82], which has shown promising results using high scan speeds for downskin surfaces. Process codes # 4 through # 6 are based on the work of Brock et al. who identified and characterized a set of process parameters which provide good part density and sideskin surface roughness [31]. Specifically, process code # 4 is optimized for low sideskin roughness, process code # 5 was identified as resulting in

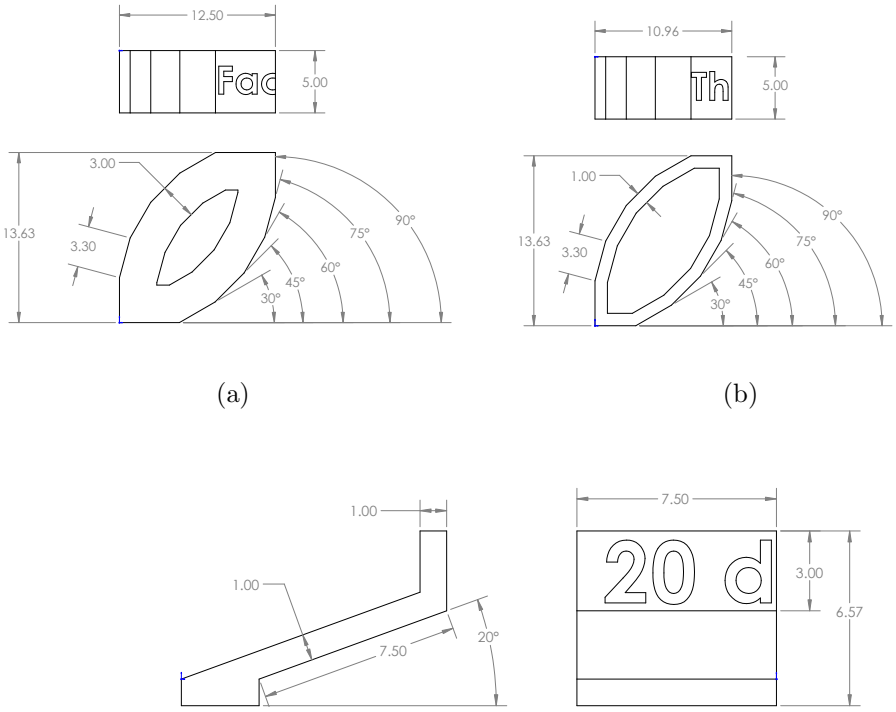


Figure 3.5: Sample geometries: (a) 3mm thick facet (b) 1mm thick facet (c) 1mm thick 20° sample.

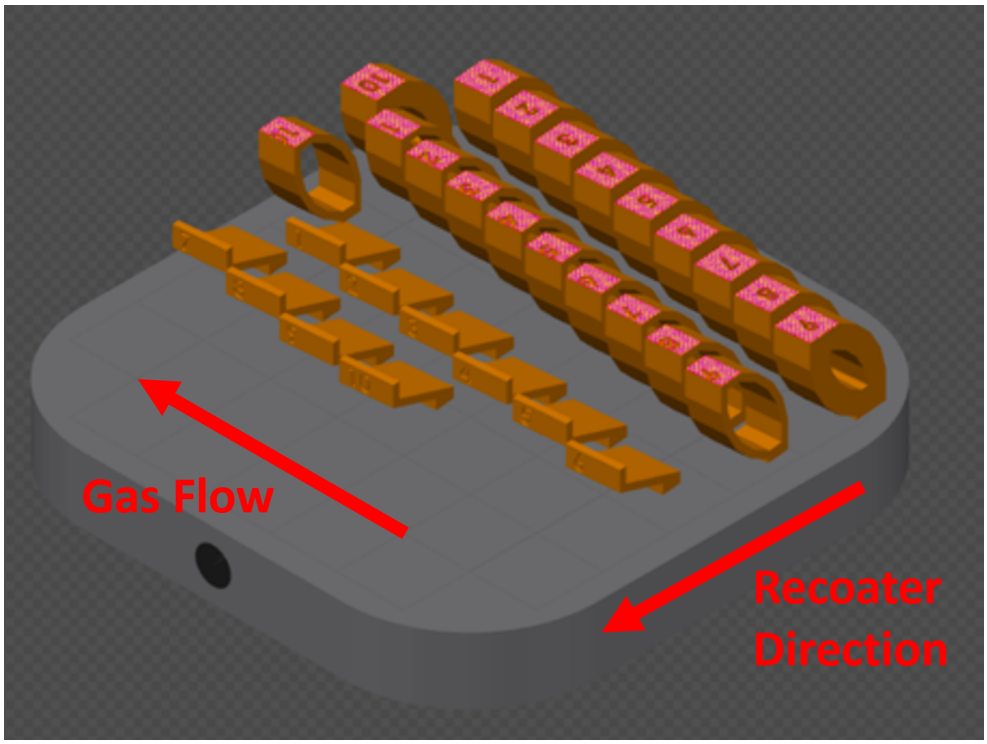


Figure 3.6: Reduced Build Volume build plate with 10 of each sample geometry.

excellent core part density, while process code # 6 was selected as it provided good density at higher scan speeds and therefore higher productivity. Finally, process code # 7 is a set of downskin process parameters that were developed based on a hypothesis that the use of a defocused beam to created low aspect ratio melt pools [26] may allow improved downskin roughness by increasing the overlap between melt pools [83]. Process code # 7 has seen use for industry parts despite not being properly characterized and as such was of interest since it visually appeared to give poor results. Figure 3.7 shows the tested process codes plotted on a process map of their effective power, P_{eff}, and effective velocity, v_{eff}.

Table 3.2: LPBF process parameters used in design of experiment. Laser power - P, beam radius - r_b, point distance - p_d, exposure time - t_e, hatch distance - h, effective laser power - P_{eff}, effective velocity - v_{eff}, and Volumetric Energy Density - VED. The drill delay time, t_d, is constant at 10 µs. A standard hatch angle rotation of 67° was used.

Process Code	P **[W]**	r_b **[µm]**	p_d **[µm]**	t_e **[µs]**	h **[µm]**	P_{eff} **[W]**	v_{eff} **[mm/s]**	VED **[J/mm^3]**	Description
# 1	400	35	50	10	100	200	2500	45.7	Highest velocity
# 2	400	35	50	15	100	240	2000	57.1	Intermediate velocity vs power
# 3	400	35	50	20	100	267	1667	68.6	Highest power
# 4	270	35	60	50	142	225	1000	54.3	Low roughness sideskin [31]
# 5	176.8	35	60	110.1	142	162.1	500	71.2	High core density [31]
# 6	255.3	35	60	50	145	212.8	999	50.4	High core productivity[31]
# 7	125	90	70	70	100	109.4	875	40.8	Defocused beam experiment

Table 3.3 shows a summary of which process parameters were used for each of the ten

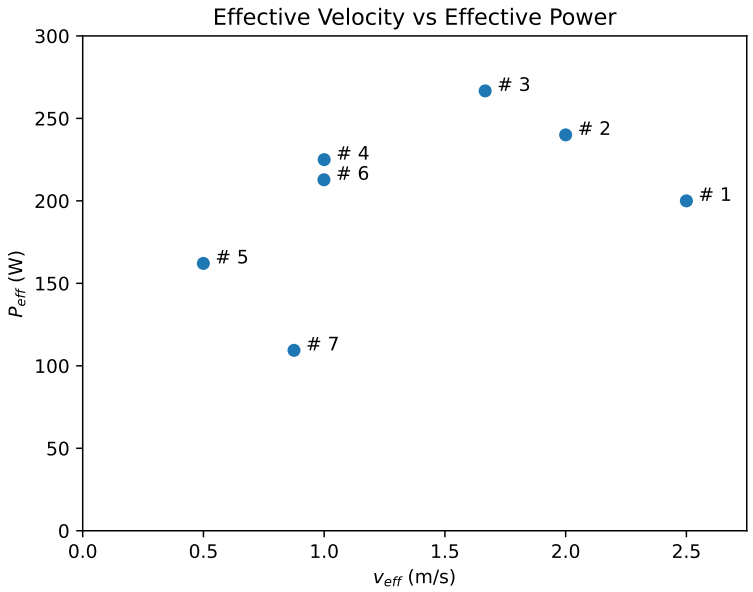


Figure 3.7: Process map of tested process parameters.

samples. To evaluate if the core process parameters had a significant effect on downskin roughness, two different process parameters were used for the core. The first four samples used the high density parameters (process code # 5), while the remaining six samples used the high productivity parameters (process code # 6) since it was predicted that they may perform better. The same process parameters were used for both the sideskin and downskin such that they would be used for every angle, though the downskin hatching strategy was only activated at 45° and below. Process codes # 1, # 3, # 4, and # 5 were used as downskin process parameters on both the # 5 and # 6 cores, while process codes # 2 and # 7 were only tested as downskin process parameters on the # 6 productivity core.

Table 3.3: Summary of core and skin process codes used for each sample.

Sample code:	**1**	**2**	**3**	**4**	**5**	**6**	**7**	**8**	**9**	**10**
Core process code:	# 5				# 6					
Skin process code:	# 4	#5	# 1	# 3	# 4	# 5	# 1	# 2	# 3	# 7

3.2.5 Surface Roughness Measurement

The surface roughness of each sample was measured using a laser optical profilometer (VK-X250, Keyence, Japan). At the 10x magnification used, the profilometer has an image size of only 1450.7 µm by 1087.4 µm, which is not sufficient for accurately measuring large scale surface roughness. To form each measurement, a set of images were stitched together using post-processing software (VK Image Stitiching, Keyence, Japan). For the facet samples, the measurement was 3 images wide and 2 images tall resulting in a measurement area of 3.48 mm by 1.85 mm, given 30 % overlap for alignment. For the 20° samples the larger size allowed the usage of a larger measurement 4 images wide and 5 images tall resulting in a measurement area of 4.50 mm by 4.13 mm. Roughness measurements were computed using post-processing software (VK Multifile Analyzer, Keyence, Japan). The software was used to level the image plane but otherwise the surface was assumed to be flat and no waviness filter was used.

3.2.6 Computed Tomography

To investigate the effect of process parameters on part porosity, select samples were scanned using X-ray computed tomography (CT) with an X-ray Microscope (Xradia 520 Versa, Zeiss, Germany). A scan resolution of 12 µm was used with two stitched together scans

being used for the taller facet samples and a single scan used for the 20° samples. Data visualization and processing was then conducted using commercially available post-processing software (Dragonfly, Comet Xylon, Germany). While this software enables the calculation of density across a region of interest, due to the thin and complex nature of most of the printed parts, it is difficult to identify a large enough region of interest to calculate accurate density values. As such, CT data is used primarily for qualitative comparison between samples in this work.

3.3 Results and Discussion

3.3.1 Prediction of Process Parameter Performance

Before the samples were printed, the models presented in Section 3.2.2 were used to predict the performance of each set of process parameters. Using the downskin melt pool overlap model the keyhole number was estimated for each combination of process parameters to be deployed at a respective downskin angle. The results are shown in Figure 3.8. It can be seen that while the keyhole number increases as the print angle decreases, none of the process parameters are expected to result in keyholing, although many of the process codes (# 3, # 4, # 5, # 6) move into the transition mode when printing at 20°. As such, it is expected that there should not be significant keyholing for any of the process parameters even when printing at very low angles.

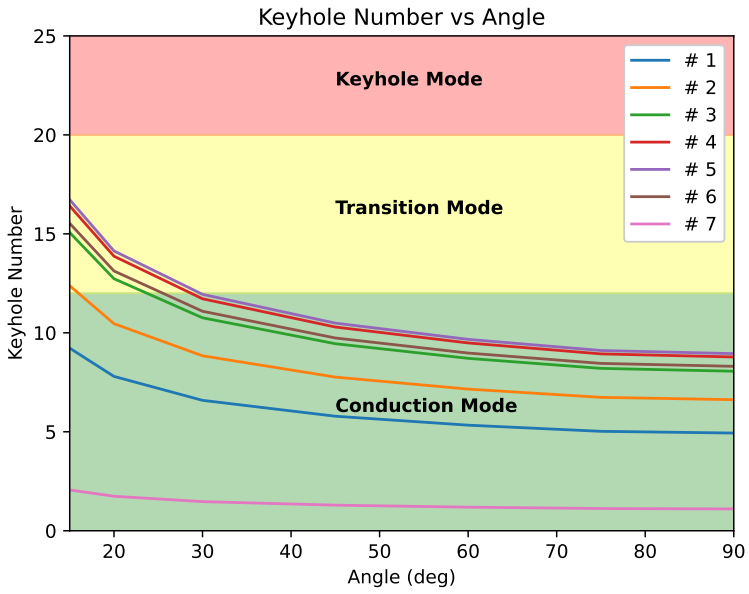


Figure 3.8: Estimated keyhole number vs angle for each set of process parameters as a function of downskin angle.

Similarly, the downskin melt pool overlap model combined with the thermophysical melt pool simulation was used to estimate the MDR for each set of process parameters across the tested range of downskin conditions. The results are shown in Figure 3.9. It can be seen that all of the process parameters which are predicted to give a good MDR at 90° are predicted to have an excessive MDR at low angles. As such, it is expected than no single set of process parameters will perform best across all angles. This predicts the importance of changing the process parameters as a function of angle, as is common practice with the use of downskin scan strategies.

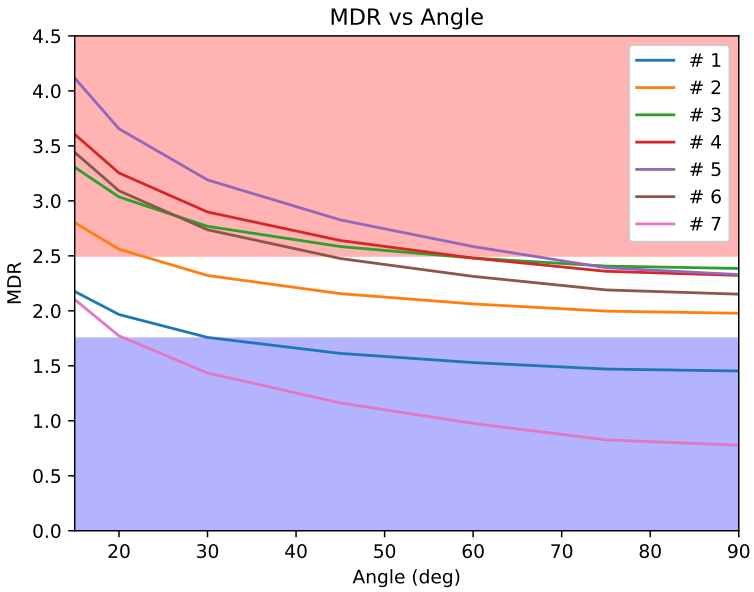
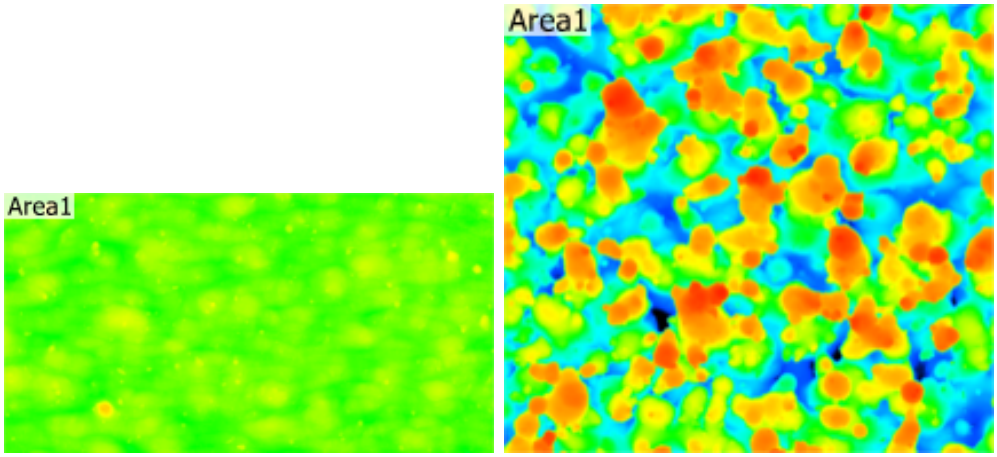


Figure 3.9: Estimated MDR vs angle for each set of process parameters. The blue region indicates too low an MDR, likely to result in lack of fusion, while the red region indicates a high MDR likely to result in excessive heat input.

3.3.2 Surface Roughness Results

All of the parts were printed as previously described. While some minor warping was observed during the printing process, all of the parts printed successfully. The parts were then cut from the build plate using electrical discharge machining (EDM) and their surface roughness was measured. Figure 3.10 shows the height map for the best and worst measured surfaces along with the corresponding angle. The complete measurements for all samples are presented in Appendix B.3. Figure 3.11 shows a plot of the roughness vs angle for each sample code based on the measured roughness of the thin and 20° samples.



(a) (b)

Figure 3.10: Best and worst surfaces measured. (a) Best roughness: sample 6, thin structure, 75°, $R_a = 8.1\mu m$ (b) Worst roughness: sample 2, 20° structure, 20°, $R_a = 98.6\mu m$.

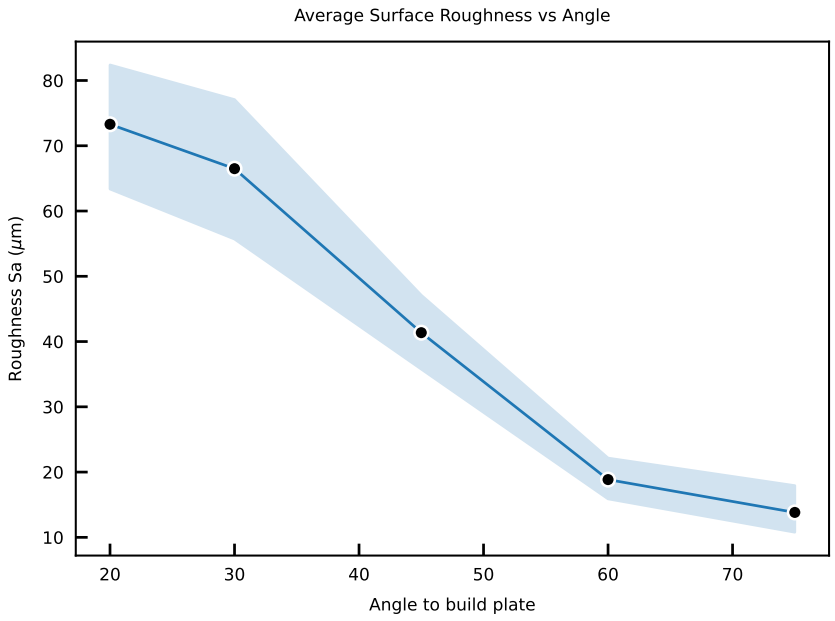


Figure 3.11: Average measured downskin roughness vs angle for thin and 20° samples with standard deviation.

Tables 3.4 and 3.5 show the measured surface roughness for each sample across each angle. Sample code # 7 has the best roughness at 20° and 30° downskin angles, while sample code # 8 has the best performance at 45°, and sample code # 6 performs the best at 60° and 75°. As such, it can be noted that a unified process parameter combination cannot be reasonably applied across all downskin inclination angles to achieve the best performance at each inclination.

Table 3.4: Surface Roughness (Sa) measurements for thin facets and 20° samples in µm. The lowest roughness at each angle is in bold text.

Angle	1	2	3	4	5	6	7	8	9	10
20°	72.6	98.6	65.5	76.1	69.9	97.8	**48.5**	51.8	71.6	80.5
30°	60.1	97.8	51.5	79.0	60.1	87.5	**44.3**	44.9	70.6	69.1
45°	35.3	44.3	37.6	55.8	35.3	36.7	31.5	**30.9**	49.5	56.7
60°	13.7	14.1	23.7	17.5	14.8	**12.5**	23.8	22.8	17.7	27.9
75°	10.7	8.9	13.7	13.5	10.3	**8.1**	13.5	14.8	14.4	30.3
Core	# 5				# 6					
Downskin	# 4	#5	# 1	# 3	# 4	# 5	# 1	# 2	# 3	# 7

Table 3.5: Surface Roughness (Sa) measurements for thick facets in µm. The lowest roughness at each angle is in bold text.

Angle	1	2	3	4	5	6	7	8	9	10
30°	67.1	92.5	47.1	68.9	55.5	92.0	**40.1**	40.7	65.9	62.3
45°	40.5	50.2	45.2	48.5	**30.8**	35.6	37.6	35.8	49.9	66.8
60°	13.9	18.3	25.7	18.2	**13.8**	14.2	22.8	23.1	21.1	24.2
75°	10.3	11.2	14.3	13.0	10.1	**9.8**	13.5	13.5	14.7	26.7
Core	# 5				# 6					
Downskin	# 4	#5	# 1	# 3	# 4	# 5	# 1	# 2	# 3	# 7

Analysis of Variance

An analysis of variance (ANOVA) was run on the roughness results, the code for which is presented in Section Appendix B.4. Unsurprisingly an extremely significant effect was found for the effect of angle ($p = 8.6 \times 10^{-33} < 0.05$) and downskin recipe ($p = 5.8 \times 10^{-12} < 0.05$) on surface roughness. The interaction between downskin parameters and angle was also found to be highly significant ($p = 9.3 \times 10^{-17} < 0.05$) which was expected since it was observed that different process codes performed best at different downskin angles.

Effect of Core Process Parameters

Despite the five downskin layers used, a significant effect on roughness due to the core recipe was found ($p = 0.00012 < 0.05$), along with the interaction between core process parameters and downskin angle ($p = 0.005 < 0.05$). Figure 3.12 shows the average roughness at each angle of all samples which used process code # 5 for the core vs those that used process code # 6 for the core, excluding samples # 8 and # 10, which used downskins only tested with core # 6. It is observed that as the downskin angle decreases, there is a larger difference in surface roughness between the two tested cores. This aligns with the ANOVA results, and shows that the effect of core process parameters becomes more pronounced at low downskin angles.

Effect of Sample Thickness

Based on the ANOVA results, no significant effect was found due to the thickness of samples ($p = 0.88$) and the average difference in roughness across all thin vs. thick samples was $0.01 \mu m$. Given that even at a 1 mm sample thickness the majority of the cross section is representative of core process parameters, it is anticipated that this may not hold true for

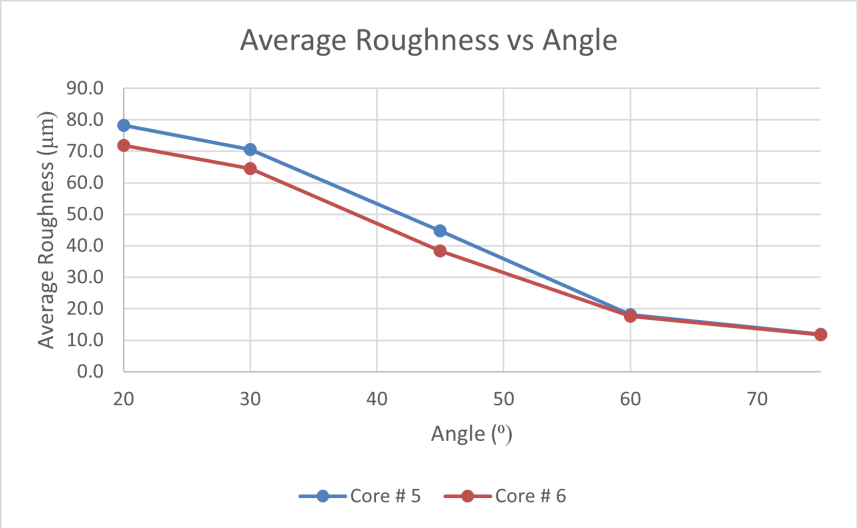


Figure 3.12: Average roughness vs angle for tested core process parameters.

even thinner samples; the investigations to corroborate this statement are out of scope for the present work.

3.3.3 Comparison Between Modeling and Results

To investigate the alignment between the results of process parameter modeling and the measured surface roughness, a 2nd order polynomial function was fitted to the measured roughness data plotted against angle and predicted MDR, as shown in Figure 3.13. It can be seen that, at each angle, there is a clear MDR which results in a minimum roughness. This ideal MDR was then computed, and the results are shown in Figure 3.14. Based on this surface fit, the ideal MDR varies from 2.15 at 20° to 1.95 at 75°. This agrees very well with the predicted ideal MDR of 2.0, and also demonstrates that the downskin melt pool overlap model introduced in this work appears to be doing a good job of compensating for the effects of downskin printing when predicting MDR.

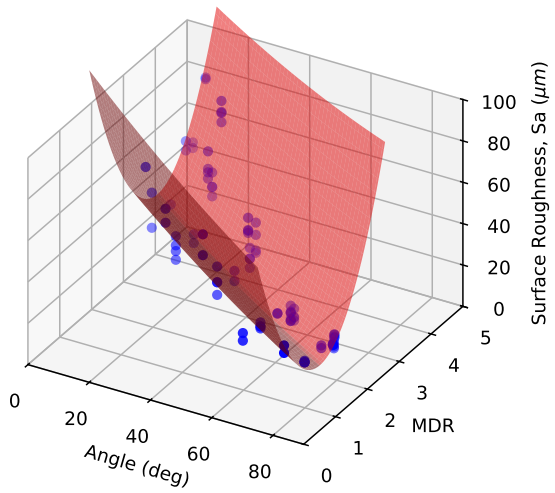


Figure 3.13: 2nd order polynomial surface, of the form $z = a + bx + cy + dx^2 + ey^2 + fxy$, fit to measured roughness data as a function of angle and MDR, with $R^2 = 0.876$. The steep convex curvature indicates a clear ideal MDR at each angle corresponding to the lowest surface roughness.

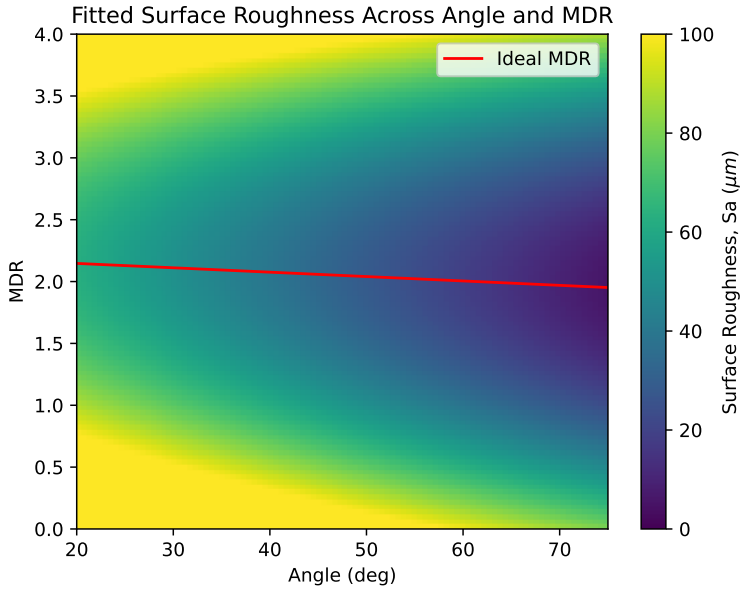


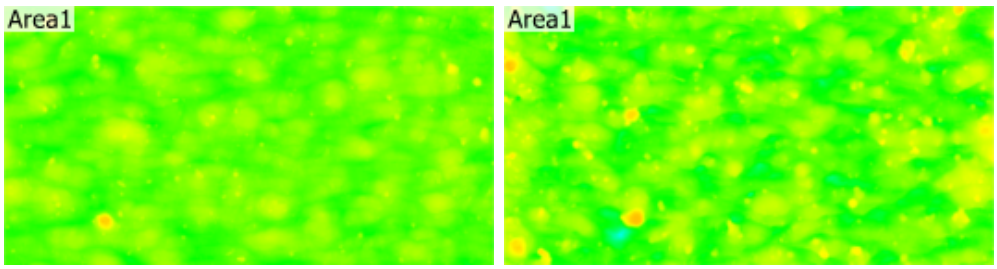
Figure 3.14: Ideal MDR for lowest surface roughness based on fitted surface. The fitted surface is plotted as a height map. The ideal MDR varies from 2.15 at 20° to 1.95 at 75°.

Effect of Powder Adherence at High Downskin Angles

While the usage of the MDR model to optimize downskin roughness appears to be promising, one notable discrepancy was observed. It appears that the model is not able to resolve some differences in roughness at high downskin angles. For example, process code # 4 and # 5 have very similar MDR and keyhole numbers to process code # 3 at 75°. However, averaging the results for each sample which used process code # 3 for downskin gave a roughness value 34 % worse than the average for process code # 4 and 46 % worse than the average for process code # 5. Comparing the surfaces for a sample using process code # 3 vs # 5, as shown in Figure 3.15, it appears that there is significantly more powder adhesion on the sample using process code # 3. While the MDR model is useful for ensuring a stable high density process, it does not seem to be effective for differentiating process parameters that result in optimized surface roughness for high downskin angles or sideskin. In these cases, roughness is relatively low compared to steep downskin and powder adhesion appears to be a more dominant factor. It is recommended that methods used by other works for sideskin roughness optimization should also be considered when attempting to optimize high angle downskin, such as the usage of transition mode process parameters to reduce powder adhesion presented by Patel et al. [84].

3.3.4 CT Scan Analysis

To further investigate the performance of the tested downskin process parameters, a select number of the printed parts were CT scanned to investigate their porosity. Specifically, all the parts for samples # 3 and # 7, which both use process code # 1 for the downskin were selected since process code #1 provided the best low angle downskin roughness. Sample # 3 uses process code #5 for the core, while sample #7 uses process code #6, which



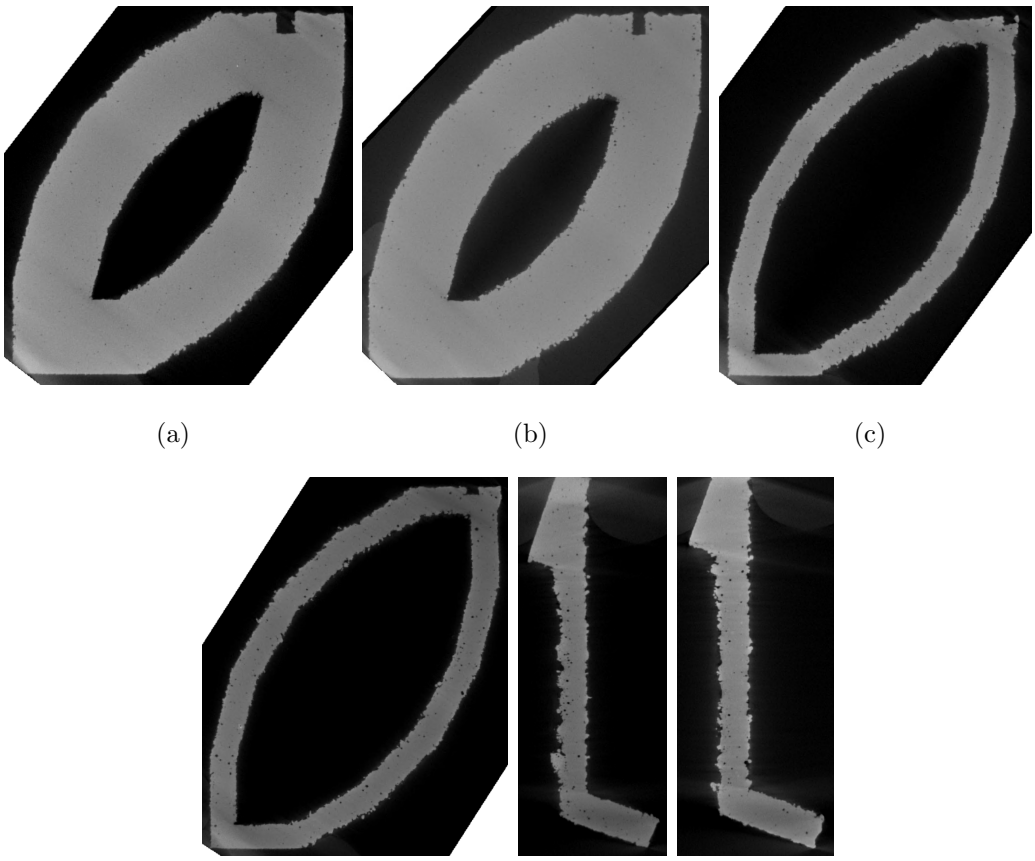
(a) (b)

Figure 3.15: Height map comparison of powder adhesion on 75° downskin. (a) Sample # 6, thin coupon, with minimal powder adhesion, $S_a = 8.1\mu m$. Roughness is dominated by gradual waviness from the underlying texture with occasional particle adhesion. (b) Sample # 9, thin coupon, with significant powder adhesion, $S_a = 14.4\mu m$. Roughness is dominated by adhered particles, visible as circular yellow and orange regions.

has a lower VED. Cross sections of the scanned parts are shown in Figure 3.16. The thick samples are observed to have good density, comparable to what is expected from past work with the same core process parameters [15].

It is observed that there is higher porosity in the thin samples. For sample # 3, thin sample, this additional porosity seems to be mostly localized to near the 30° downskin surfaces. for sample # 7, thin sample, there appears to be additional porosity throughout the entire part. For the 20° parts, both sample # 3 and # 7 exhibit significant porosity near the downskin surface. All of the observed porosity appears to be nearly spherical, indicating keyhole porosity [85]. This contradicts the prediction that both process code # 5 and # 6 should lie well within the conduction mode during core printing. The presence of porosity in small cross sections is likely related to the short scanning vector. This increases the local temperature as there is a significant reduction in time between the melting of adjacent scan tracks, resulting in less time for the area to cool. As such, based on the

keyhole number equation, Equation 3.3, it can be seen that the keyhole number is related to the substrate temperature and, if the substrate temperature increases, so will the keyhole number. So far, in this work, it has been assumed that the substrate temperature, T_0, is constant at ambient (293 K). The short scan tracks due to the thin walls, combined with the overhanging geometry which may result in poor local cooling, lead to a much higher substrate temperature, leading to keyholing and increased porosity [86], [87].



(a) (b) (c)

(d) (e) (f)

Figure 3.16: CT cross sections of samples. Thick samples maintain a high density while significant keyhole porosity is observed in thin samples, particularly at low downskin angles. (a) Sample # 3 thick. (b) Sample # 7 thick. (c) Sample # 3 thin. (d) Sample # 7 thin. (e) Sample # 3 20°. (f) Sample # 7 20°.

3.3.5 Core Power Investigation

Based on the keyhole porosity observed in the CT scans of the initial roughness samples discussed above, it was decided to further investigate the effect of core power on surface roughness and porosity. An additional five samples with a 20° downskin inclination were printed, with process code # 1 used for the downskin. All of the core process parameters were held identical to process code # 6, with the exception of power, which was varied between 255.3 W and 180 W, as shown in Table 3.6. Sample A uses identical process parameters to sample # 7, with samples B through E using increasingly lower powers. The samples were printed on a full build as part of a later work (Chapter 4). Table 3.6 also shows the measured surface roughness for the samples. All 5 samples were CT scanned and Figure 3.17 shows cross sections from these scans.

Based on CT scan observations, Sample A shows clear and significant near surface keyhole porosity, as well as some pores throughout the part. Similar but lesser porosity is observed for sample B. Sample C performs best and has minimal porosity across the entire volume. Sample D has good density near the downskin surface, but the top half of the part shows significant irregularly shaped pores, indicative of lack of fusion [85]. This effect is exacerbated for sample E, with good density near the downskin and severe lack of fusion near the top of the part. This agrees with the simulated MDR for each sample, which predicts that samples A through C should be stable with good density ($MDR > 1.75$), while D and E are expected to be unstable for core printing ($MDR < 1.75$).

As seen in Table 3.6, there is a clear correlation between the core power and the surface roughness, with lower core powers resulting in a lower downskin surface roughness. Comparing sample A to sample E there is a 13% reduction in surface roughness. There also appears to be improved dimensional accuracy, with sample E matching the constant 1mm

thickness of the CAD geometry much better than sample A. A balance between improved surface roughness performance, shape fidelity, and acceptable density is achieved in Sample C.

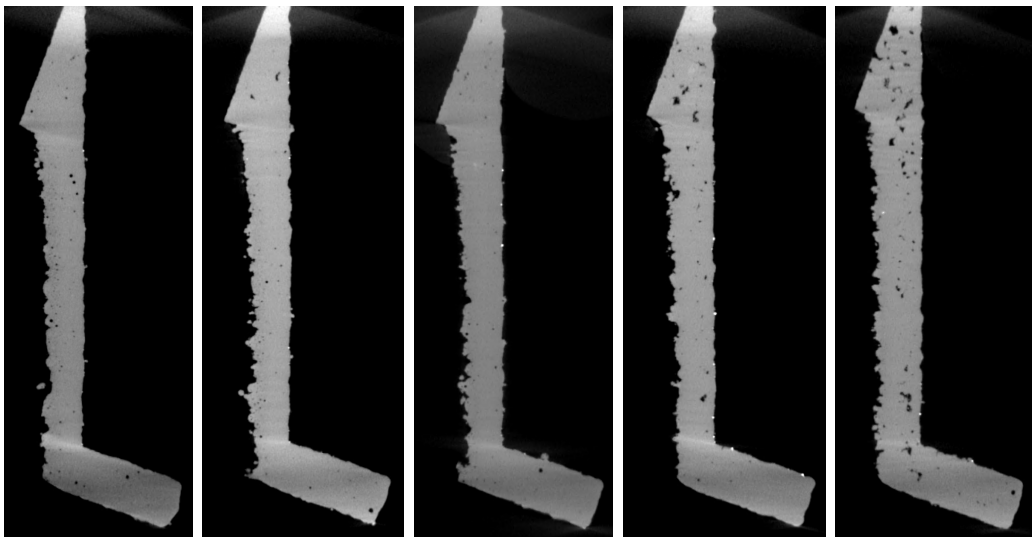
Based on these results, it appears that even within a relatively thin 1 mm sample, there is no single ideal core power that performs best across all criteria (density, geometric fidelity, surface roughness) and a compromise is required. Ideally, if it is possible to smoothly vary the process parameters to transition from a downskin strategy into a core strategy, it may be possible to combine the best of both worlds, achieving excellent downskin roughness while also maintaining a high core density.

Table 3.6: Surface Roughness (Sa) measurements for 20° samples printed with reduced core powers.

Sample Code	A	B	C	D	E
Roughness (μm)	51.2	50.9	48.2	46.2	44.5
Core Power (W)	255.3	240	220	200	180
Core P_{eff} (W)	212.8	200	183.4	166.7	150
Core MDR	2.15	2.00	1.79	1.55	1.29
Approximate Density (%)	99.15	99.84	99.83	99.27	97.74

3.3.6 Recommended Process Parameters

Unfortunately, given the limitations of most current LPBF build software, it is not usually possible to achieve smooth transitions between various process parameters across different surface inclinations (to control downskin process parameters) and feature cross-sectional



(a) (b) (c) (d) (e)

Figure 3.17: CT cross sections of modified core power samples. Surface roughness and dimentional accuracy improve as power decreases, while porocity transitions from keyhole to high density, to severe lack of fusion: (a) Sample A, core power 255.3 W (b) Sample B, core power 240 W (c) Sample C, core power 220 W (d) Sample D, core power 200 W (e) Sample E, core power 180 W.

area (to control core parameters). Instead, a fixed set of core, sideskin, and downskin process parameters must be selected. Based on the results presented in this and past work, Table 3.7 presents the recommended process parameters, given the limitations of available build software.

Process code #1 is recommended for downskin, since it provides the best results at low angles, although, once again, better control of process parameters would be ideal since process code #2 performs better at 45°. While process code # 4 provided slightly worse roughness compared to #5 at 60° and 75°, it was selected since the difference is quite small and previous work identified it as having better sideskin (90°) performance [15]. Process code # 6 is recommended for the core, since it results in better downskin roughness; however, in applications where material properties are more critical than surface roughness, process code #5 may be preferable, based on the higher reported density [15].

Given these recommended parameters, Figure 3.18 presents a comparison of the roughness achieved using the recommended process parameters identified in this work, compared with those published by a major machine manufacturer for AlSi10Mg at a layer thickness of 30 µm [41]. It can be seen that the process parameters identified in this work result in significantly lower downskin surface roughness, and printing has been achieved at angles lower than what is typically recommended.

Table 3.7: Recommended process parameters for AlSi10Mg. Laser power - P, beam radius - r_b, point distance - p_d, exposure time - t_e, hatch distance - h, effective laser power - P_{eff}, effective velocity - v_{eff}, and Volumetric Energy Density - VED. The drill delay time, t_d, is constant at 10 µs. A standard hatch angle rotation of 67° should be used.

Use	Process Code	P [W]	r_b [µm]	p_d [µm]	t_e [µs]	h [µm]	P_{eff} [W]	v_{eff} [mm/s]
Downskin	# 1	400	35	50	10	100	200	2500
Sideskin	# 4	270	35	60	50	142	225	1000
Core	# 6	255.3	35	60	50	145	212.8	999

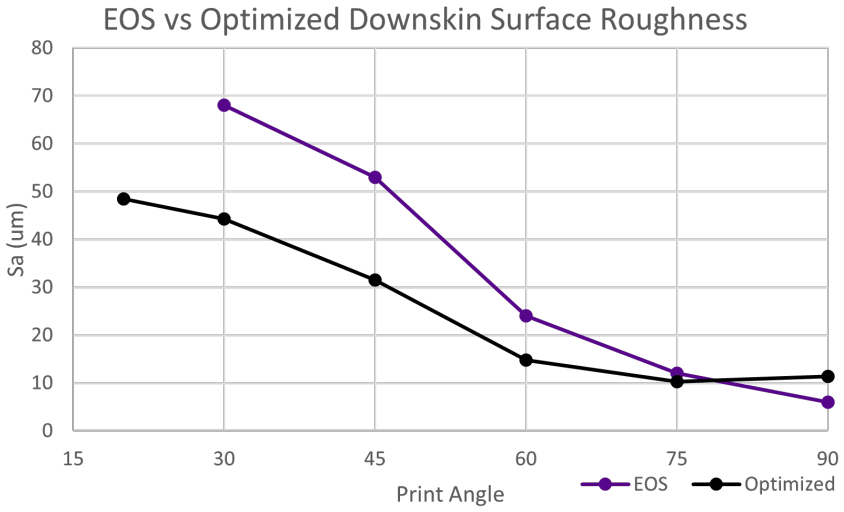


Figure 3.18: Comparison of downskin surface roughness data published by EOS vs roughness measurements from optimal process parameters [41].

3.4 Conclusions

In this work, the downskin surface roughness of parts manufactured from AlSi10Mg using LPBF was investigated. A set of process parameters based on previous work were tested to identify an optimal combination for low angle downskin printing, with thin and thick features. Modeling was used to predict the performance of each set of process parameters and comparisons were made between the modeled results and the measured performance. The key findings of this work are summarized as follows:

1. A new downskin melt pool overlap model was proposed to estimate the change in effective material boundary conditions (solid vs. powder) in the underlying layer, as a function of downskin angle. This enables the use of previously developed techniques for predicting process parameter performance in the core of parts to be applied when developing strategies for downskin printing.

2. The use of melt depth ratio (MDR) presented in past works to predict performance was further expanded upon, and the results found in this work aligned well with past observations. Combined with the downskin melt pool overlap model, MDR was found to be effective for predicting the performance of process parameters at low downskin angles, with an MDR of 2 consistently leading to the best outcomes across all downskin angles. It was found that at high downskin angles, it alone is likely not sufficient to predict good surface roughness performance and other factors must also be considered.

3. A significant corelation was found between the core process parameters used and the downskin surface roughness ($p = 0.00012 < 0.05$), particularly at low angles, despite the usage of five downskin layers.

4. No significant effect on downskin roughness due to part thickness could be measured ($p = 0.88$), though this may not hold for parts thinner than the 1 mm minimum thickness tested in this work.

5. It appears that considerable amounts of keyhole porosity were present in the samples, despite predictions that the process parameters should lie well within the conduction mode. This may be due to poor cooling in the thin parts, resulting in higher localized temperatures. By reducing core power, it was possible to further reduce downskin roughness at 20° by 13% and reduce near surface porosity; however, further from the surface, the reduced power results in a significant lack of fusion.

6. A set of process parameters have been identified which allow the printing of AlSi10Mg with good density and significantly lower surface roughness that that published by industry. These parameters have been used to successfully print parts at angles as low as 20°.

Chapter 4

Investigation of Part Thickness and Orientation on the As-Built Tensile Properties of AlSi10Mg Manufactured using Laser Powder Bed Fusion

Abstract

In this study, the tensile properties of thin-walled structures printed from AlSi10Mg using LPBF are considered. Significant research has been completed, both on the characterization of LPBF bulk material properties, as well as the design of optimized lightweight structures which often rely on the use of fine features. However, there has been little investigation into how material properties are affected when printing thin, complex structures.

In this work, the tensile properties of samples ranging from 1 mm to 3 mm in thickness are considered, as well as the effect of build orientation. The tensile properties of samples printed at angles ranging from 90° down to 20° are tested to investigate the effect of print angle on these thin-walled structures. The surface roughness of samples is measured and ranges between 9.3 μm and 56.5 μm as a function of print angle. CT scanning is used to investigate and correct the true cross-section of as-printed samples. The tensile properties of a set of process parameters optimized for high productivity and low roughness are characterized, achieving a yield strength of 265.6 $\pm$ 1.0 Mpa and an ultimate tensile strength of 422.1 $\pm$ 4.1 MPa. Samples printed at steep overhang angles are found to have significantly degraded tensile properties, which may have significant implications for the design of TPMS heat exchangers and other complex thin structures. Finally, comparisons are made between as-printed and machined tensile coupons, demonstrating that as-printed coupons may provide more representative tensile data when designing LPBF parts that are used in the as-printed state.

4.1 Introduction

Additive manufacturing (AM) has seen widespread adoption over the past decades in part due to its unique ability to create extremely complex geometry with no need for specialized tooling and very few design constraints [11]. In particular, laser powder bed fusion (LPBF), a type of metal AM that allows the printing of parts with very high density and good feature resolution has become very popular for the manufacturing of complex fluid components such as hydraulic manifolds and heat exchangers [1], [10].

A common material used in these components is the aluminum alloy AlSi10Mg. Aluminum alloys are often a good choice for fluid and thermal applications since they provide

a good balance of high strength, light weight, and high thermal conductivity. AlSi10Mg specifically is popular for LBPF since it provides reasonably good material properties while being significantly less prone to cracking during printing compared to other popular aluminum alloys such as 6061 [63], [64].

Some past work on additively manufactured hydraulic manifolds includes the work of Schmelzle et al. [18] who demonstrated the usage of LPBF to re-design a 5,000 PSI hydraulic manifold used for maintenance of the Bell Boeing V-22 Osprey. They successfully consolidated a 17 part assembly into a single component, resulting in a 60 % mass reduction [18]. Another example is the work of Olaf et al. [20] who achieved a 92 % reduction in mass by re-designing a hydraulic manifold for an underground drilling rig, although notably they used a different material and had a reduced maximum operating pressure from the original design.

Another application of LPBF that has gained significant attention and research is the use of LPBF to manufacture triply periodic minimal surfaces (TPMS) for high performance heat exchangers. TPMS heat exchangers are easily manufactured using AM, but are otherwise impractically complex to produce. However, they enable significantly higher heat transfer rates and the usage of significantly more compact and therefore lightweight heat exchangers [88]–[91].

LPBF has also seen consistent research and industry adoption for the manufacturing of closed impellers. Closed impellers are a critical component in many high-performance rotodynamic pumps used across a number of industries from water pumping to rocket engine turbopumps [92]–[94]. Due to the need for complex and accurate internal channels, they have traditionally been made using investment casting or by fixing together multiple machined parts using brazing or other methods. All of these options require expensive and specialized tooling and expertise [94]. In comparison, LPBF presents the option of

manufacturing closed impellers without the need for tooling [95].

A common trend among these additively manufactured fluid power components is a reliance on the ability of LPBF to create thin channels and walls. These thin walls must resist significant stress due to fluid pressure, centripetal forces, and other applied loads. It is therefore critical for designers to have good data on the structural properties of thin-walled parts produced with LPBF.

To address this, many studies have been published on the mechanical properties of various materials manufactured using LPBF, including AlSi10Mg [96], [97], and many suppliers conduct testing and publish results for their systems and materials [41], [98], [99]. To ensure consistent results, these studies typically investigate the bulk properties of printed parts based on coupons machined from larger printed blanks to eliminate the effect of surface roughness and other inconsistencies. This approach is beneficial for providing material data that is well standardized and that aligns with data published for other conventional manufacturing methods. The results are useful when designing large components where the effects of surface defects are minimal and the assumption of bulk material properties is valid. However, many practical AM designs rely on fine features for cooling, weight optimization, or other functional requirements. This results in a disconnect between the available material properties and the applications for which they are needed.

This work looks to address this disconnect by investigating the effect of wall thickness on the tensile properties of as-printed AlSi10Mg samples which have not been machined. Thin samples 1 mm thick, along with thick samples 3 mm thick are printed in a variety of orientations and build plate locations. The Young's modulus, yield strength, ultimate tensile strength (UTS), and elongation at break of these samples are measured and discussed. In addition to investigating the effect of wall thickness, a number of secondary variables are considered; to provide a better baseline against results published in literature, the

measured mechanical properties for machined and as-printed samples are compared, along with the effect of two different sets of process parameters. The effect of part orientation relative to the gas flow and recoater and the effect of height above the build plate on tensile properties are discussed, along with the effect of these variables on the surface roughness of the printed samples. Finally, the effect of overhang angle on the tensile properties of thin samples is investigated by testing a set of samples printed at angles ranging from 75° down to 20° relative to the build plate.

4.2 Materials and Methods

4.2.1 Printing Process and Paramerters

Parts were printed on a modulated beam LPBF system (AM400, Renishaw, UK) with a layer thickness of 35 µm. Plasma atomized AlSi10Mg powder (AP&C, Montreal, Canada) with a size distribution of D10-D90 of 20-63 µm and a D50 of 45 µm was used.

Since the goal of this work is to gain an understanding of the effect part thickness on tensile properties, targeting applications which rely on complex, thin structures, process parameters appropriate for such were considered. The selected process parameters, referred to as Recipe 1, were optimized to give a low surface roughness across a wide range of print angles while maintaining a high density of 99.88% as shown in previous work (Chapter 3) [15]. Two border scans were used, as well as 5 downskin layers at angles steeper than 45°. Table 4.1 shows a summary of the selected process parameters. A hatch angle rotation of 67° per layer was used.

Table 4.1: Recipe 1: Low roughness optimized LPBF process parameters used for most samples [15]. Laser power - P, beam radius - r_b, point distance - p_d, exposure time - t_e, hatch distance - h, effective laser power - P_{eff}, effective velocity - v_{eff}, and Volumetric Energy Density - VED. The drill delay time, t_d, is constant at 10 µs and a layer height of 35 µm is used.

Region	P [W]	r_b [µm]	p_d [µm]	t_e [µs]	h [µm]	P_{eff} [W]	v_{eff} [mm/s]
Core	255.3	35	60	50	145	212.8	999
Sideskin	270	35	60	50	142	225	1000
Downskin	400	35	50	10	100	200	2500

Additionally, Patel et al. [26] reported the use of a de-focused beam to achieve a part density over 99.98%. Based on this very high density, these parameters have been used for a number of structural applications (Chapter 2); however, the mechanical properties have not been tested prior. To resolve this and compare the tensile properties of two different sets of high density process parameters, a subset of the printed samples used the parameters identified by Patel et al. Referred to as Recipe 2, they are shown in Table 4.2. These parameters were originally printed with a layer height of 30 µm, but had to be printed with 35 µm layers in this work for compatibility with the other set of process parameters. This is not expected to have a significant impact due to the minor difference and large melt depth associated with these parameters [26].

Table 4.2: Recipe 2: Alternate high density optimized LPBF process parameters as reported by Patel et al. [26]. Laser power - P, beam radius - r_b, point distance - p_d, exposure time - t_e, hatch distance - h, effective laser power - P_{eff}, and effective velocity - v_{eff}. The drill delay time, t_d, is constant at 10 µs and a layer height of 35 µm is used.

Region	P [W]	r_b [µm]	p_d [µm]	t_e [µs]	h [µm]	P_{eff} [W]	v_{eff} [mm/s]
Core	350	54	55	60	100	300	786
Sideskin	270	35	60	50	100	225	1000
Downskin	125	90	70	70	100	109	875

4.2.2 Design of Experiment

To investigate the effect of part thickness on tensile properties, a set of coupon blanks were printed at a thickness of 1 mm (thin) and 3 mm (thick). The blanks are shown in Figure 4.1. Each blank is 110 mm long and 26 mm tall, allowing for two coupons to be cut from each blank. Three replicates of the thick and thin blanks were printed in the X and Y directions to assess any effect of orientation due to the recoater or gas flow direction. This results in a total of 12 blanks or 24 coupons. These samples, referred to henceforth as the horizontal samples, are given a code to easily distinguish them based on their properties. First is the replicate number (1, 2, or 3), followed by the orientation (aligned with the X or Y axis), the thickness (thin - TN or thick - TK), and the vertical position (top - T or bottom - B). For measuring the roughness an additional tag is added to refer to the front - F or the back - B face. For example: 2YTN-B-F refers to the front face of the bottom

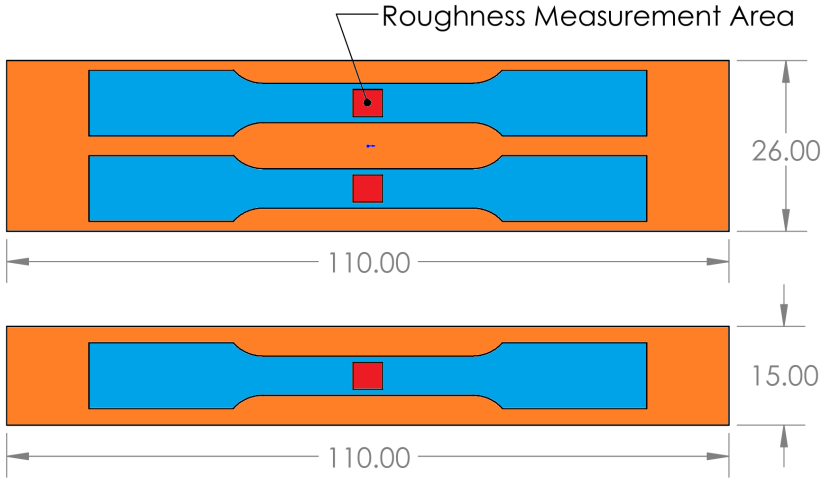


Figure 4.1: Layout of tensile samples (blue) on sample blanks (orange). The area used for measuring surface roughness is shown in red. Top: horizontal coupon blank use for thick (3 mm) and thin (1 mm) samples. Bottom: overhang sample blank used for 75°, 60°, 45°, 30°, and 20° samples, 1 mm thick.

section of the second thin replicate printed along the Y axis.

To investigate the effect of print angle, a set of 1 mm thick overhang samples were printed at overhang angles of 75°, 60°, 45°, 30°, and 20° relative to the plane of the build plate (90° is vertical). Blanks were used as shown in Figure 4.1. Each overhang blank is only tall enough to cut out a single coupon and two replicate blanks were printed at each angle. The overhang samples are named based on their angle and replicate number with an additional tag used for roughness measurement indicating the downwards - Dw or upwards - Up facing surface. For example 30-2-Dw refers to the downward facing surface of the second replicate printed at an angle of 30° relative to the build plate.

The horizontal and overhang samples were printed as a single build, the layout for which is shown in Figure 4.2, including the gas flow and recoater directions. In addition to

the samples used in this work, a series of lattices and fluid channels for use in other works were included on the same build. For the horizontal samples, the front of the sample is considered to be the side that faces into the recoater for the X samples and the side that faces into the gas flow for the Y samples. After printing, the sample blanks are cut from the build plate using electrical discharge machining (EDM). After the surface roughness is measured, the samples are then waterjet cut from the blanks. Often sheet metal samples cut this way would then have their edges machined to improve surface finish; however, the waterjet cuts have significantly better surface finish than the rough as-printed surface and this step adds significant cost so it was deemed uneconomical.

Due to the substantial additional powder and build time required to print vertical test samples on an otherwise vertically short build, it was not economical to include vertical samples as part of the main build. Instead, a set of samples were included with a different build, shown in Figure 4.3. To allow comparison between as-printed and machined samples, ten flat dogbone samples matching the geometry shown in Figure 4.4 were printed, along with ten cylinders. The cylinders are 7mm in diameter and are then machined into cylindrical subsided samples which follow the ASTM E8M standard [100] and have the exact same geometry used by a large machine manufacturer for their tensile testing [101]. The dimensions for the round samples are shown in Figure 4.4. The samples are labeled F1 through F10 and R1 through R10 to denote the flat vs round samples. To compare the properties of the two recipes of interest, the odd numbered flat and round samples use Recipe 1, while the even numbered samples use Recipe 2.

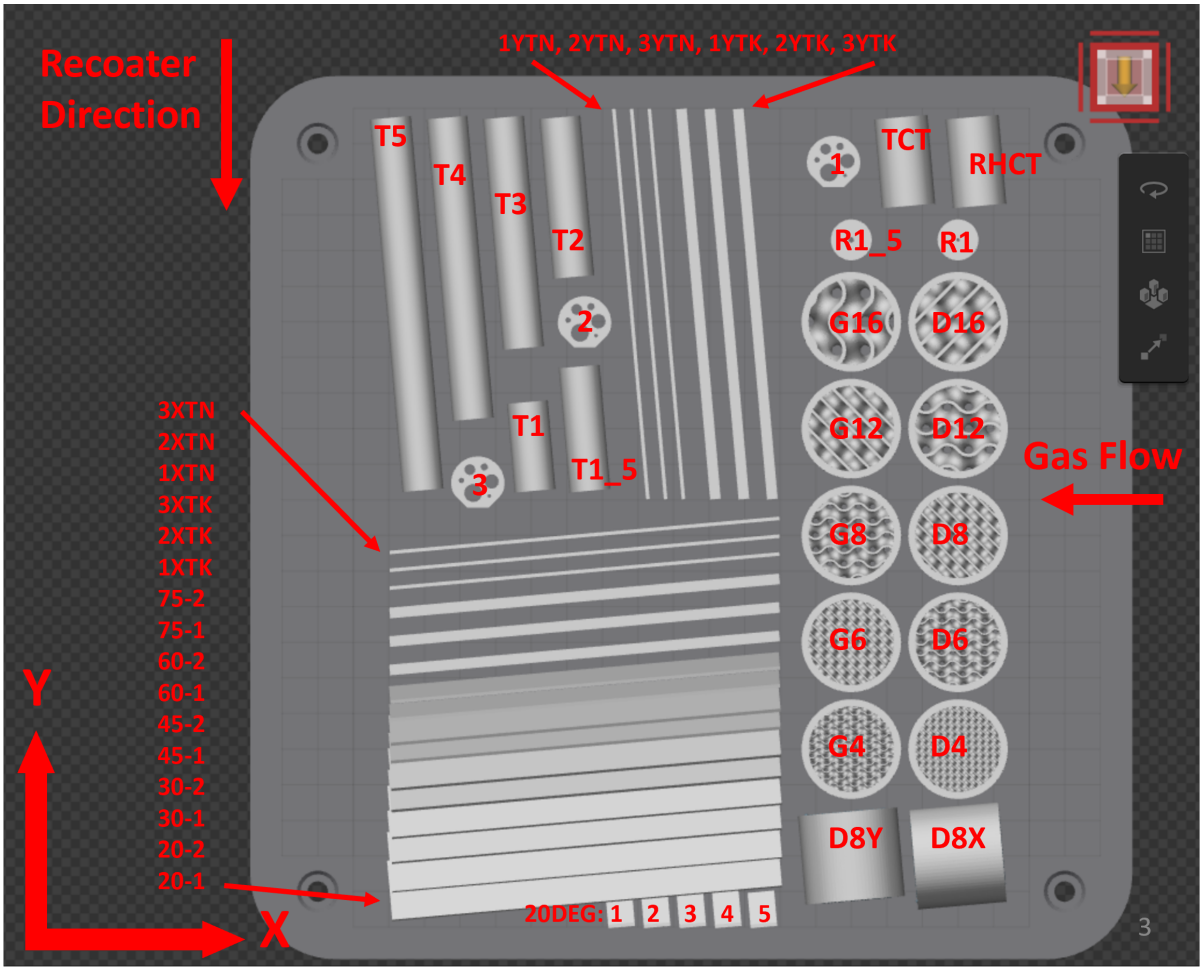


Figure 4.2: Build plate layout for horizontal and overhang tensile experiment indicating X and Y axis, along with the recoater and gas flow directions. Only samples 1YTN - 3YTK, and samples 3XTN - 20-1 are used in this work.

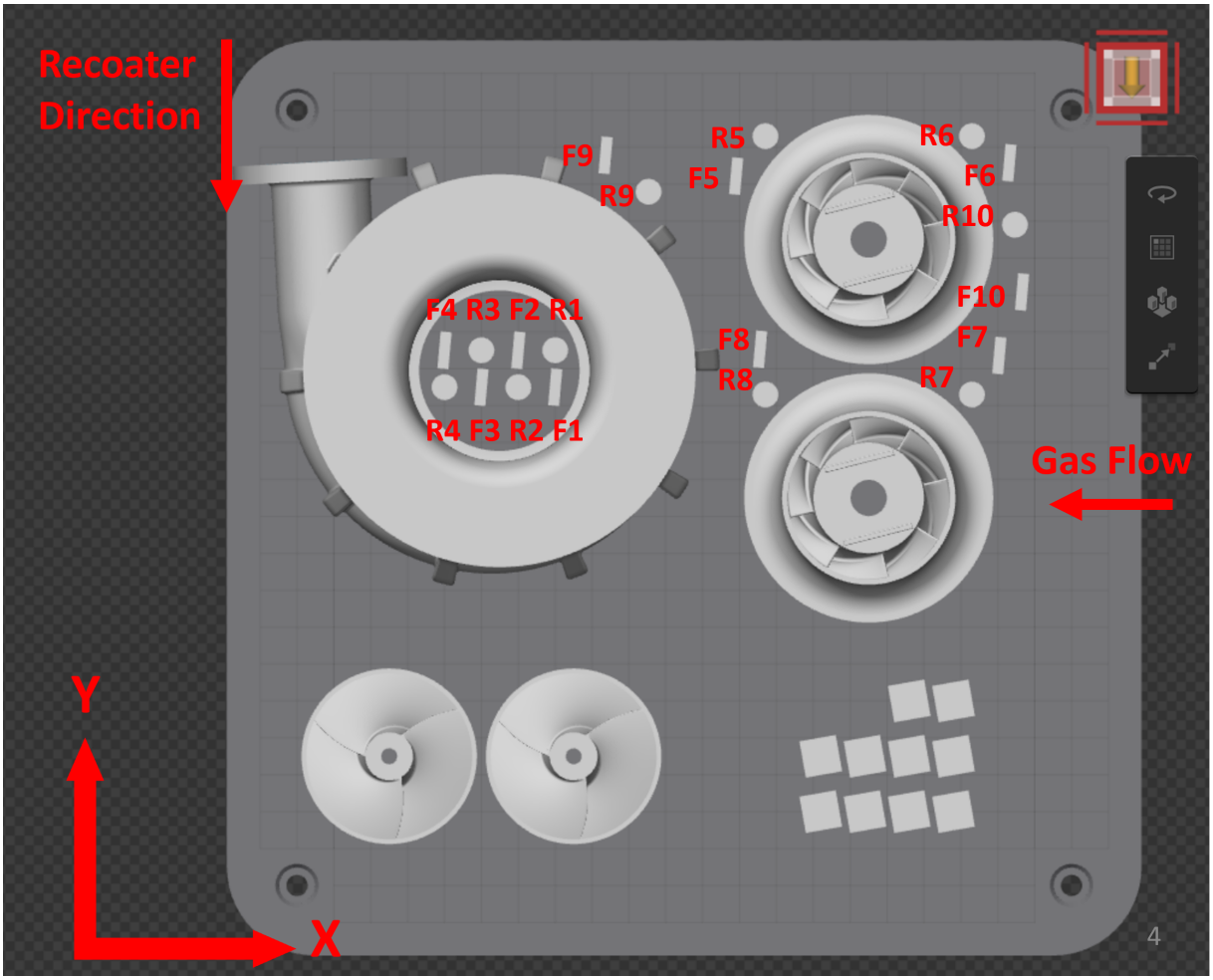
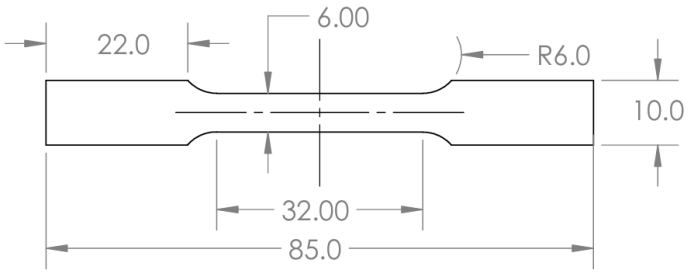
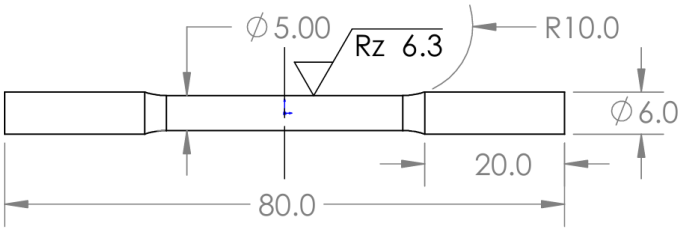


Figure 4.3: Build plate layout for vertical sample coupons showing the recoater and gas flow directions. Only the labeled samples (R1 - R10 and F1 - F10) are discussed in this work.



(a)



(b)

Figure 4.4: Sample geometry and dimensions. (a) Subsized ASTM E8 sample geometry with reduced grip length used for horizontal, overhang, and vertical flat samples. (b) round subsized ASTM E8M sample geometry with dimensions matching those used by a major machine manufacturer [100], [101].

4.2.3 Characterization

Coupon Measurement

Sample thickness and width were manually measured using a set of digital calipers (CD-6" CSX, Mitutoyo, Japan). The flats of the calipers were used and the minimum value along the reduced section of the sample was used to minimize the effect of large spatter on the recorded sample size. For the thicker 3 mm samples, the waterjet cutter results in coupons with a very slightly trapezoidal profile, since the cut has more kerf at the bottom than at the top. Both the narrower and wider sides were measured and the average of the two values gives the effective width of the sample.

Surface Roughness

A side effect of the large set of tensile coupons is that a large amount of flat side skin material was printed in various orientations and locations on the build plate. To enable an investigation of the effects of orientation and location on surface roughness, a laser optical profilometer (VK-X250, Keyence, Japan) was used to measure the surface roughness. For each sample blank, two measurements were taken on each side of the blank, corresponding to the locations of the cut coupons as shown in Figure 4.1. Since each profilometer image is only 1450.7 µm wide by 1087.4 µm tall, a single image is not sufficient to accurately capture the surface roughness. To ensure accurate roughness measurements, a 4.50 mm by 4.13 mm area was measured by stitching together a 4x5 grid of images, with 30 % overlap for alignment. Data analysis was done using proprietary image analysis software (VK Multifile Analyzer, Keyence, Japan). Software leveling of the surface was done, but no form of waviness or noise filter was applied.

Computed Tomography

A select group of samples were analyzed using X-ray computed tomography (CT) scanning to more accurately measure their effective cross-sectional area. An X-ray Microscope (Xradia 520 Versa, Zeiss, Germany) was used with a scan resolution of 9.74 µm. Due to the cost of CT scanning and the limited field of view when scanning at high resolution, only the center region of each selected sample could be scanned. By scanning the middle of the samples it was then possible to determine the true average cross-sectional area of each sample. Using commercially available post processing software (Dragonfly, Comet Xylon, Germany), each sample was aligned, and the ends of the scan were cropped off to remove unwanted scan artifacts. The volume of the remaining region (which is 800 layers, or approximately 7.8 mm tall) was then measured, along with the exact height of the region. The average cross-sectional area of the region of interest was then found by dividing the volume by the height.

Tensile Testing

Tensile testing was done according to the ASTM E8 standard for tension testing of metallic materials [100]. Subsized coupons as defined by the standard were used, although the grip lengths were reduced from 30 mm to 22 mm to minimize print time and sample cost. The geometry used is shown in Figure 4.4. Per the standard, a gauge length of 25 mm is used for the coupons. To verify the performance of the test setup, verification coupons were water jet cut from 5052-H32 aluminum, 2.53 mm thick. The purpose of these coupons was to practice and refine the test methodology, as well as confirm that the measured values agreed with the published material properties for 5052-H32 [102].

Testing was done using an electromagnetic load frame with a 30 kN load cell (C43-304,

MTS Systems, United States). An extensometer with the required 25 mm gauge length was used to measure elongation during the tests (634.31F-24, MTS Systems, United States). The complete test setup is shown in Figure 4.5. Given a reduced section length of 32 mm as shown in Figure 4.4 and the ASTM E8 requirement of 0.015 mm/mm/min, the crosshead speed was set to 0.48 mm/min. The test procedure is as follows:

- A tensile coupon is placed into the test jaws. Plastic 3D printed guides are used to ensure that coupons sit centered in the jaws. The lower jaw is then tightened onto the coupon.
- The extensometer is then mounted to the coupon with elastic bands, and visually aligned with the center of the reduced section of the coupon. Once mounted, the locking pin is removed from the extensometer.
- The load cell and extensometer are zeroed.
- The upper jaw is tightened onto the coupon.
- The protective shield is placed around the sample, and the test is conducted using the control software (MTS TestSuite TW Elite, MTS Systems, Uninted States)
- Once the test is complete, the data is exported. The extensometer is then removed, along with the broken coupon, and the system is reset for the next test.

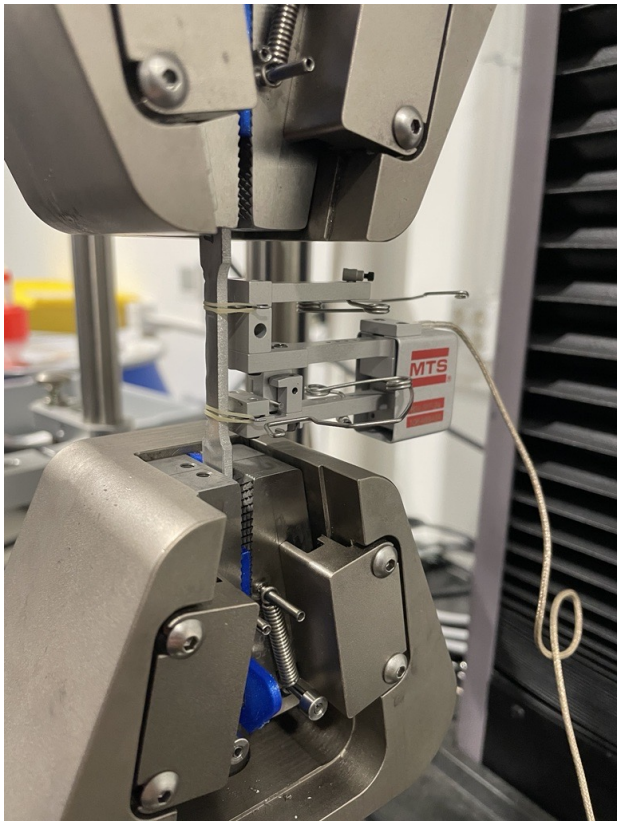


Figure 4.5: Tensile tester setup with extensometer attached to a verification sample via elastic bands. 3D printed jigs are used to aid the alignment of samples (seen in blue).

Tensile Data Processing

Custom python code, loosely based on that presented by Kazarinoff [103], was written to process the raw load cell and extensometer data. The code is presented in Appendix C.1. The ultimate tensile strength (UTS) is found by dividing the highest measured force by the cross sectional area. Since all of the samples suffered brittle failure, the UTS point and the break point are the same. Therefore elongation at break is found based on the measured strain at the point of maximum force. The standard 0.2% offset method was

used for estimating yield, wherein a line is fit to the linear elastic region of the stress strain data and the yield point is considered to be the intersection between the stress strain data and the fitted line offset by a strain of 0.002 mm/mm. The linear region was considered as any data where the stress and strain was less than 25% of what was measured at the UTS point. The measured Young's modulus is given by the slope of this fitted linear elastic line. Figure 4.6 shows a visual of this data for one of the measured samples.

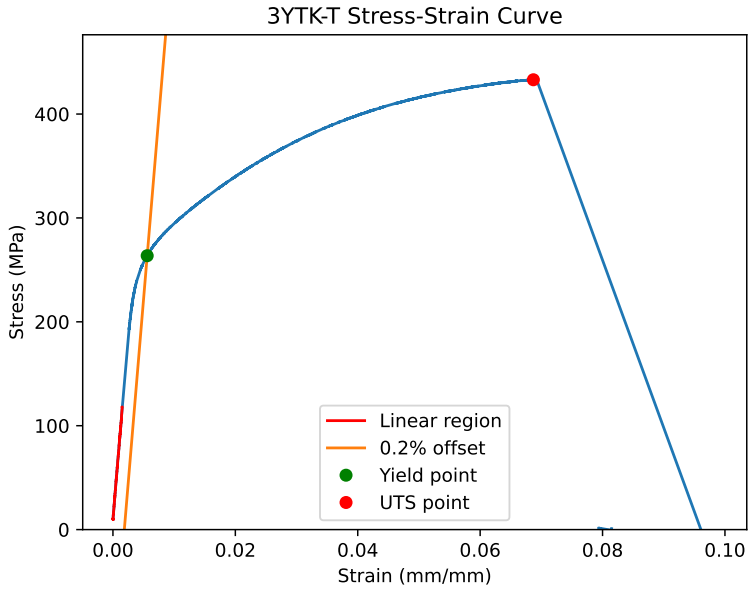


Figure 4.6: Stress Strain curve for sample 3YTK-T, showing the raw data, as well as the calculated linear region used to compute the 0.2% offset, the 0.2% offset line, the intersection point defining the yield strength, and the UTS point.

4.3 Results and Discussion

4.3.1 Surface Roughness

After the parts were printed as previously described, they were EDM cut from the build plate and the arithmetical mean height surface roughness, $S_a[\mu m]$, of each horizontal and overhanging sample was measured. Table 4.3 presents the measured roughness for the horizontal samples and Table 4.4 presents the measured roughness for the overhang samples. The roughness of the overhang samples closely matches previous observations (Chapter 3) and discussion is beyond the scope of this work. The roughness of the vertical samples was not measured. The average surface roughness of the horizontal samples was 11.01 $\pm$ 0.34 µm. To investigate the effect of thickness, orientation, and height above the build plate on surface roughness, an analysis of variance (ANOVA) was run, the code for which is presented in Appendix C.3.1.

Effect of Part Orientation

A highly significant ($p = 4.8 \times 10^{-8} < 0.05$) effect on surface roughness was found for the part orientation (X vs. Y), contributing to 40 % of the measured variance. The parts printed along the Y direction had a surface roughness 1.49 µm less than those printed in the X direction on average, corresponding to a 13.5 % improvement.

Effect of Side Relative to Recoater and Gas Flow

The effect of side (front vs. back) alone was not found to be significant ($p = 0.84$); however, this is unsurprising since front vs back is arbitrary without the context of the orientation.

Table 4.3: Measured surface roughness of the horizontal test coupons with no waviness filtering. The sample naming scheme is described in Section 4.2.2.

Thick							
Sample	S_a (μm)	Sample	S_a (μm)	Sample	S_a (μm)	Sample	S_a (μm)
1XTK-T-F	10.38	1YTK-T-F	10.66	1XTK-T-B	9.72	1YTK-T-B	9.34
1XTK-B-F	12.56	1YTK-B-F	10.27	1XTK-B-B	13.04	1YTK-B-B	10.49
2XTK-T-F	10.55	2YTK-T-F	10.41	2XTK-T-B	12.21	2YTK-T-B	10.02
2XTK-B-F	11.89	2YTK-B-F	10.59	2XTK-B-B	12.48	2YTK-B-B	10.75
3XTK-T-F	10.85	3YTK-T-F	10.12	3XTK-T-B	11.43	3YTK-T-B	9.74
3XTK-B-F	10.76	3YTK-B-F	9.88	3XTK-B-B	15.42	3YTK-B-B	9.44
Thin							
Sample	S_a (μm)	Sample	S_a (μm)	Sample	S_a (μm)	Sample	S_a (μm)
1XTN-T-F	11.55	1YTN-T-F	10.76	1XTN-T-B	11.78	1YTN-T-B	9.78
1XTN-B-F	10.99	1YTN-B-F	11.48	1XTN-B-B	11.33	1YTN-B-B	9.92
2XTN-T-F	11.68	2YTN-T-F	11.1	2XTN-T-B	11.46	2YTN-T-B	9.68
2XTN-B-F	12.57	2YTN-B-F	10.72	2XTN-B-B	13.06	2YTN-B-B	9.49
3XTN-T-F	11.34	3YTN-T-F	11.83	3XTN-T-B	11.87	3YTN-T-B	9.7
3XTN-B-F	10.71	3YTN-B-F	10.12	3XTN-B-B	12.54	3YTN-B-B	10.11

Table 4.4: Measured surface roughness of the overhang test coupons with no waviness filtering. The sample naming scheme is described in Section 4.2.2.

Downskin		Upskin	
Sample	S_a (μm)	Sample	S_a (μm)
20XTN-C-Dw	50.93	20XTN-C-Up	14.5
20XTN-C-Dw	56.47	20XTN-C-Up	13.65
30XTN-C-Dw	42.34	30XTN-C-Up	16.9
30XTN-C-Dw	39.76	30XTN-C-Up	17.6
45XTN-C-Dw	30.32	45XTN-C-Up	16.93
45XTN-C-Dw	32.98	45XTN-C-Up	16.67
60XTN-C-Dw	16.07	60XTN-C-Up	14.54
60XTN-C-Dw	16.79	60XTN-C-Up	13.93
75XTN-C-Dw	12.62	75XTN-C-Up	13.09
75XTN-C-Dw	13.06	75XTN-C-Up	10.77

The combination of side and orientation was found to be significant ($p = 0.00039 < 0.05$). To gain a better understanding of the effect of side relative to the recoater and gas flow, the ANOVA was run again for just the X axis samples and just the Y axis samples. For samples printed aligned with the X axis, a slightly significant effect due to the side was found ($p = 0.034 < 0.05$). The side facing the recoater had, on average, 0.88 µm, or 7.9% smoother than the side facing away from the recoater. This may be explained by the recoater pushing spatter towards the back side of the part, leading to a rougher surface. For samples printed aligned with the Y axis, a more statistically significant effect due to the side was found ($p = 0.00062 < 0.05$). It was found that the side facing into the gas flow had a surface roughness on average 0.79 µm or 7.2% worse than the side facing away from the gas flow. This was a contradiction to the expectation that the gas flow would push spatter towards the back face and might result in a worse roughness on the back face. There are two possibilities that may be worth investigating as to why the gas flow side roughness is worse. The first is that spatter from parts upstream of the sample may have an increased tendency to catch on the front face of the sample. The second is that gas flow may affect the tendency of powder to adhere to the side of the part.

Effect of Height from the Build Plate

A significant effect due to the height of the sample above the build plate was observed ($p = 0.017 < 0.05$) with the top sample of each blank having a surface roughness on average 0.53 µm, or 4.8% lower than the bottom sample printed closer to the build plate. The reason for this is difficult to determine since there are a number of possible explanations. A change in cooling rate as the print height gets further from the build plate could have an effect. Alternatively, there is a significant change in layer print time (or equivanelty the print latency time) between when the bottom sample is printed and the top which may

affect part cooling. This is because the overhanging samples, as well as a number of fluid channels, finish printing before the top sample is printed. Similarly, since there are fewer parts being printed near the top, there is less spatter generation from nearby parts.

This last possibility seems particularly likely, as it was found that there is a significant effect due to the combination of part position and orientation on surface roughness ($p = 0.019 < 0.05$). Comparing the average difference in roughness between the top and bottom for the X axis samples gives an improvement of 1.05 µm for the top samples, while comparing the top vs bottom for the Y axis samples gives an insignificant average improvement of 0.01 µm. Referring to Figure 4.2, it can be seen that the X axis samples lie behind a set of teardrop channels (T1 - T5) which are 12 mm tall and therefore finish printing after the roughness measurement area of the bottom samples (Shown in Figure 4.1) but before the top samples. It seems likely that this may have led to a significant reduction in the amount of spatter being pushed onto the samples by the recoater, causing a significant change in surface roughness. A significant effect due to the combination of thickness and height above the build plate was also observed ($p = 0.028 < 0.05$), which could likely be attributed to this same phenomenon, as the thin samples are closer to the teardrops and likely to receive more of the spatter.

Effect of Part Thickness

No significant effect due to the thickness of samples was found on the surface roughness ($p = 0.62$). This aligns with observations on the effect of thickness on downskin roughness from previous work (Chapter 3).

4.3.2 Tensile Measurement

After the surface roughness of the samples was measured, the samples were then waterjet cut and measured. A subset were CT scanned, as described in Section 4.2.3. Table 4.5 presents the results of these measurements for the horizontal and overhanging coupons. Notably, the thicknesses measured with calipers are appreciably higher than those measured with CT for any given sample. There is also an obvious reduction in sample thickness at overhang angles of 45° or less, with the thinnest measured samples being the 20 degree overhang coupons. Figure 4.7 shows the complete set of test samples. Once the coupons were measured, tensile testing was conducted as previously described. First, five of the verification coupons were tested and it was confirmed that the setup was operating as intended. Then, all of the experimental samples were tested. Once all of the data was collected, it was processed using the code presented in Appendix C.1.

Table 4.5: Summary of measured sample dimensions for horizontal and overhang coupons. Width and Thickness are based on manual measurement with calipers. Deviation is the difference between the designed thickness, and the true thickness measured via CT.

Coupon	**Width** (mm)			**Thickness**	**CT Area**	**CT thickness**	**Deviation**
	min	max	average	(mm)	(mm^2)	(mm)	(μm)
1XTK-T	5.9	5.98	5.94	3.24	-	-	-
1XTK-B	5.82	5.93	5.88	3.35	-	-	-
2XTK-T	5.81	5.92	5.87	3.28	-	-	-
2XTK-B	5.9	5.99	5.95	3.25	-	-	-
3XTK-T	5.89	5.98	5.94	3.24	-	-	-
3XTK-B	5.81	5.92	5.87	3.29	-	-	-

1YTK-T	5.8	5.9	5.85	3.22	-	-	-
1YTK-B	5.87	5.97	5.92	3.22	-	-	-
2YTK-T	5.81	5.9	5.86	3.18	-	-	-
2YTK-B	5.9	5.96	5.93	3.22	-	-	-
3YTK-T	5.87	5.97	5.92	3.18	18.017	3.043	43.36
3YTK-B	5.79	5.89	5.84	3.25	17.871	3.060	60.02
1XTN-T	-	-	5.95	1.24	-	-	-
1XTN-B	-	-	5.94	1.34	-	-	-
2XTN-T	-	-	6.00	1.19	-	-	-
2XTN-B	-	-	5.94	1.36	-	-	-
3XTN-T	-	-	5.99	1.32	6.337	1.058	57.85
3XTN-B	-	-	5.96	1.34	6.301	1.057	57.23
1YTN-T	-	-	5.98	1.2	-	-	-
1YTN-B	-	-	5.95	1.24	-	-	-
2YTN-T	-	-	5.95	1.16	-	-	-
2YTN-B	-	-	5.93	1.2	-	-	-
3YTN-T	-	-	5.90	1.19	6.221	1.054	54.34
3YTN-B	-	-	5.99	1.21	6.300	1.052	51.70
20-1	-	-	5.88	1	4.054	0.689	-310.60
20-2	-	-	5.88	1.01	4.091	0.696	-304.23
30-1	-	-	5.94	1.21	5.397	0.909	-91.36
30-2	-	-	5.94	1.16	5.456	0.919	-81.47
45-1	-	-	5.93	1.22	5.816	0.981	-19.30
45-2	-	-	5.91	1.22	5.851	0.990	-10.06
60-1	-	-	5.94	1.28	6.316	1.063	63.27

60-2	-	-	5.91	1.27	6.302	1.066	66.25
75-1	-	-	5.92	1.22	6.275	1.060	60.02
75-2	-	-	5.92	1.25	6.277	1.060	60.27

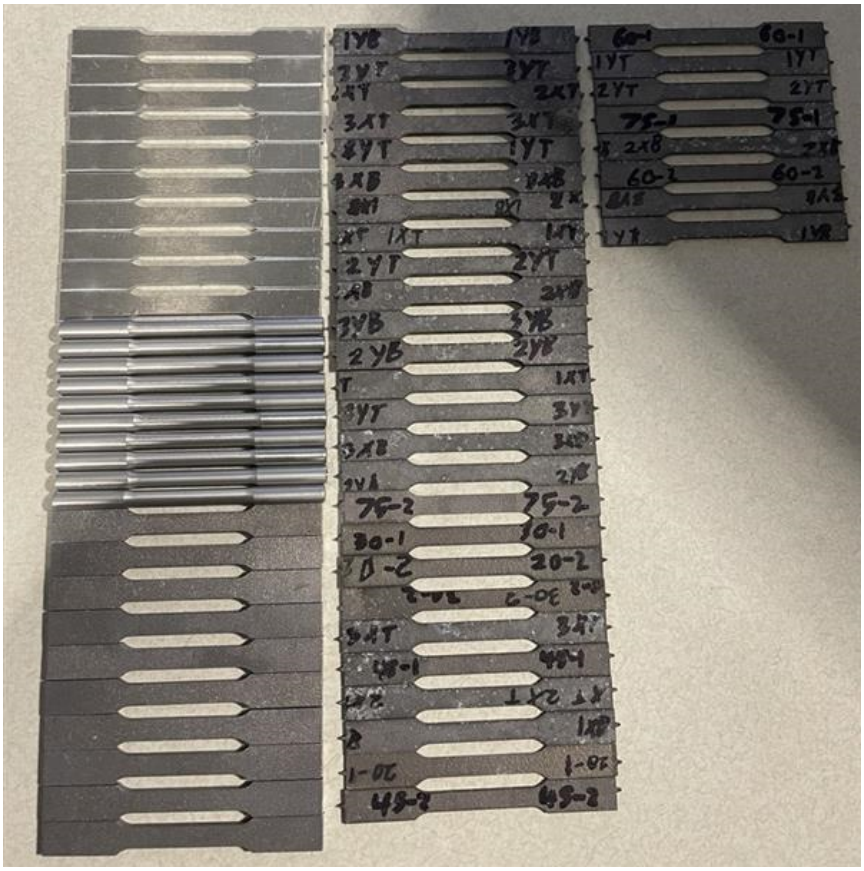


Figure 4.7: Complete set of tensile coupons after machining. Top left: verification samples, middle left: machined vertical round samples, bottom left: flat unmachined vertical samples. Middle and right are the waterjet horizontal and overhang samples.

4.3.3 Young's Modulus and Correction of Cross-sectional Area Error

Figure 4.8 shows the calculated Young's modulus based on the measured area of each horizontal sample. It is observed that there is significant deviation across samples. This is unexpected as at ambient temperature aluminum alloys typically have a relatively constant Young's modulus of approximately 70 GPa [40], [98], [104]. Running an analysis of variance (ANOVA), the code for which is presented in Appendix C.3.2, a significant effect due to thickness (1mm vs 3mm, $p = 2.3 \times 10^{-8} < 0.05$), orientation (X vs Y, $p = 0.00080 < 0.05$), and position (Top vs Bottom, $p = 0.033 < 0.05$) was found. These effects are similar to the effects found for surface roughness and it was suspected that this may be caused by measurement error from the surface roughness of the as-printed parts. Figure 4.9 shows the average surface roughness of each sample plotted against the deviation between the measured and designed thickness of each sample. There is a clear trend of an increased surface roughness leading to an increase in error between measured and designed thickness. This will in turn be propagated into the tensile measurement results, resulting in erroneous results.

Rather than continuing to rely on the manual measurement values for cross-sectional area, the CT scan data was considered since it should provide the true average cross-section of the parts. Based on the six scanned horizontal samples, the true thickness of the horizontal samples was $54.1 \pm 4.5 \mu m$ greater than the as-designed thickness. Since not all of the horizontal samples could be scanned, it was therefore assumed that the thin samples all have a thickness of 1.0541 mm and the thick samples have a thickness of 3.0541 mm. Since the waterjet cut edges result in a smooth surface, with some variation in width, the manual measurements of width were trusted and only the thickness was corrected.

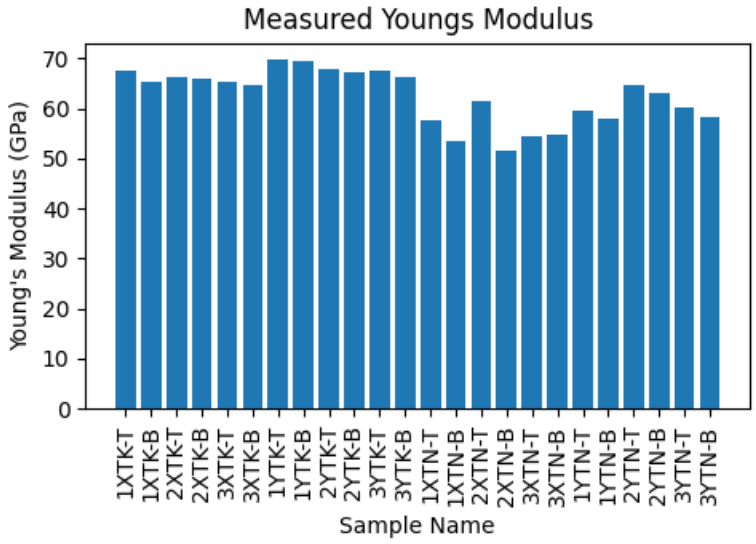


Figure 4.8: Calculated young's modulus of horizontal samples based on physically measured cross-sectional area.

Using the corrected cross-section, the tensile properties of the horizontal samples were then re-calculated. Figure 4.10 shows a comparison of the updated Young's modulus based on the corrected cross-section compared with the values calculated using the manually measured thickness. The average Young's modulus using the corrected cross-section is 69.8 $\pm$ 0.7 GPa, which very closely matches results published by the LPBF machine manufacturer [98]. Re-running the ANOVA, only the effect of part thickness was found to be significant on the young's modulus ($p = 0.0021 < 0.05$), with the thick samples having a modulus 1.7% higher than the thin samples.

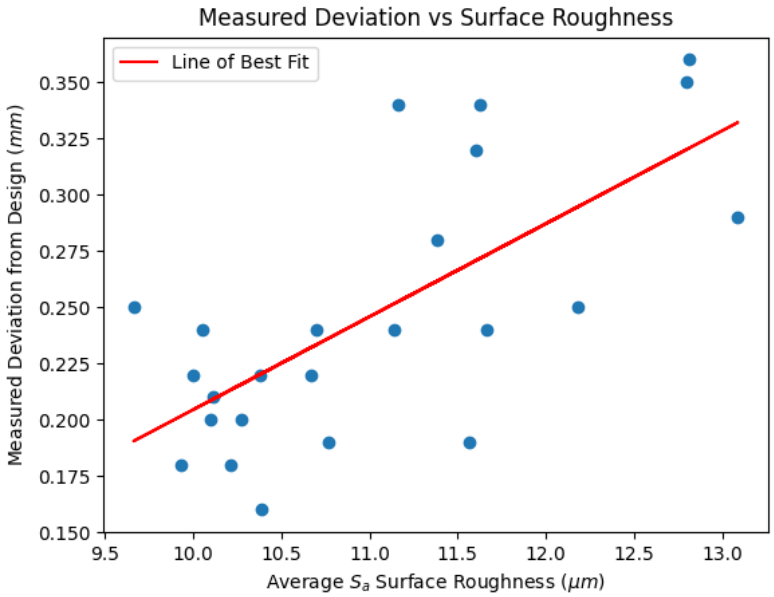


Figure 4.9: Deviation between the sample CAD design and measured sample thickness against average surface roughness of each horizontal sample. A linear line of best fit is used, with an R^2 of 0.481.

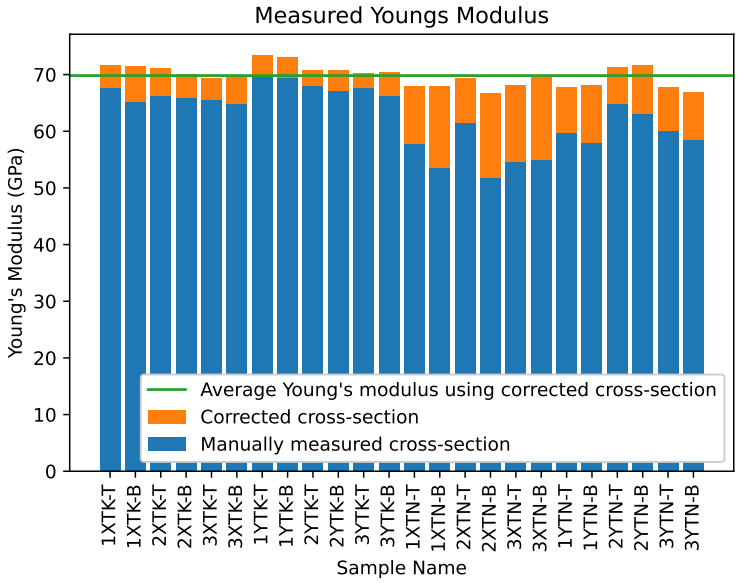


Figure 4.10: Comparison of calculated Young's modulus based on manual cross-section measurements vs. corrected cross-section based on CT results. The average Young's modulus using the corrected cross-section is 69.8 ± 0.7 GPa.

4.3.4 Effect of Thickness and Orientation on Tensile Properties

Using the corrected cross-section, the UTS and yield strength were then found for each horizontal sample, the results for which are shown in Figure 4.11. The average UTS was found to be 422.1 ± 4.1 MPa and the average yield strength is 265.6 ± 1.0 MPa. ANOVA results show a significant effect on yield strength due to thickness ($p = 6.6 \times 10^{-5} < 0.05$) and orientation ($p = 0.0040 < 0.05$).

Given the low variance of the yield data, these correspond to relatively minor effects. The thinner samples had an average yield strength 1.7 MPa, or 0.64%, higher than the thicker samples, while samples printed along the Y axis had an average yield strength 1.1 MPa, or 0.40%, higher than those printed along the X axis. While these results were found to be statistically significant, given the degree of accuracy required for most engineering applications, these minor differences of less than 1% are likely of minimal concern to most designers. ANOVA also showed no statistically significant effects due to thickness, orientation, or height above the build plate on UTS. The measured % elongation at break for each sample is shown in Figure 4.12. The average elongation at break was found to be 6.1 ± 0.4%, with ANOVA showing no significant effect due to the tested variables.

4.3.5 Effect of Part Angle on Tensile Properties

All ten of the overhang samples were scanned using CT, allowing direct measurement of their cross-section. This was an important choice since the first observation made was that there is a significant change in dimensional accuracy as a function of overhang angle, as shown in Figure 4.13. At shallow overhang angles of 75° and 60°, the thickness closely matches that of the horizontal samples. The thickness at 45° is slightly lower, but still near the as-designed dimensions. At steep overhang angles of 30° and 20°, there is a

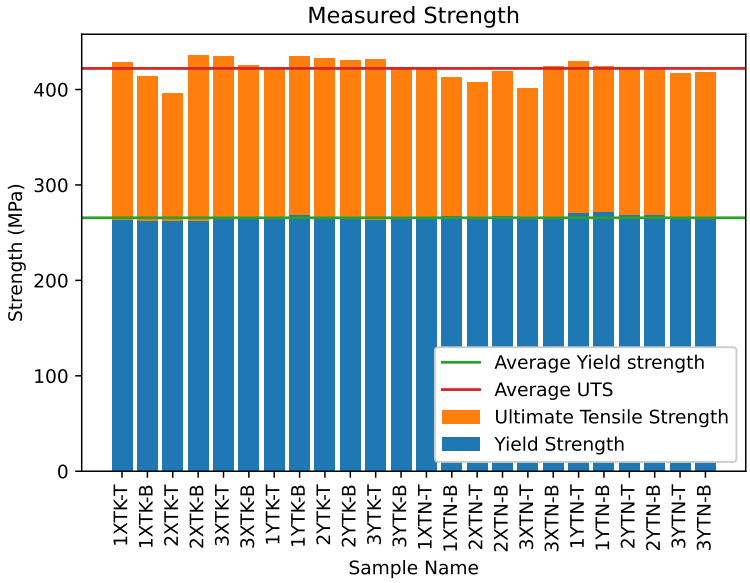


Figure 4.11: Measured UTS and yield strength of horizontal samples based on corrected cross-section. The average UTS is 422.1 ± 4.1 MPa, and the average yield strength is 265.6 ± 1.0 MPa.

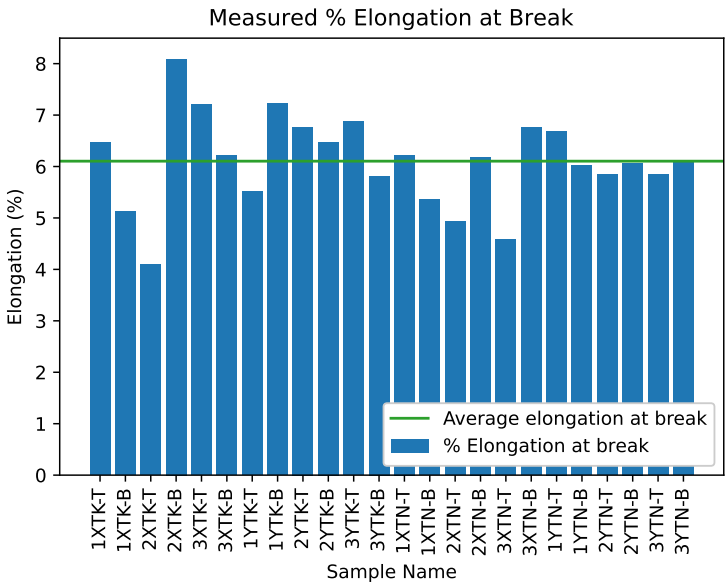


Figure 4.12: Measured % elongation at break for all horizontal samples. The average is $6.1 \pm 0.4\%$.

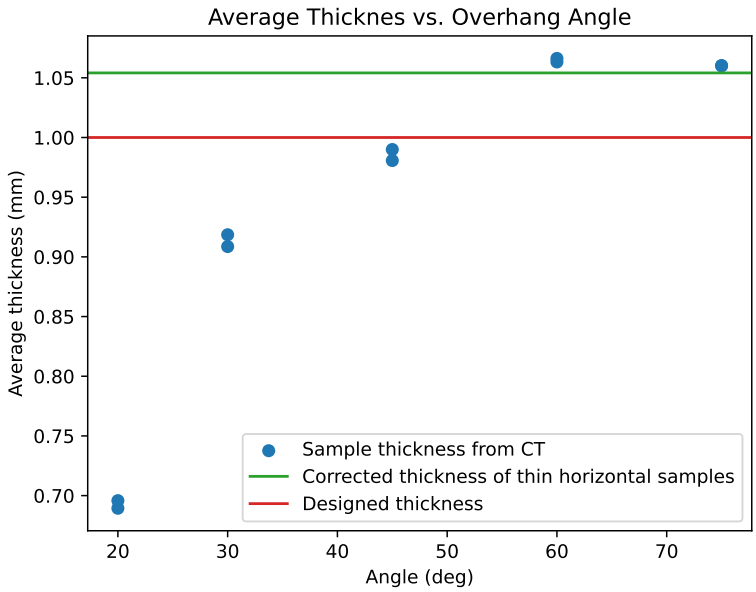


Figure 4.13: Average thickness of overhang samples based on CT vs print angle relative to the build plate. There are two replicates at each angle.

significant reduction in the thickness of the parts. Independent of the effects of overhang angle on tensile properties, this is of notable concern since parts that are printed thinner than expected will experience higher stresses than the designed geometry.

Calculating the tensile properties of the overhang samples, significant effects due to print angle are found for Young's modulus ($p = 0.0045 < 0.05$), UTS ($p = 6.0 \times 10^{-6} < 0.05$), yield strength ($p = 8.8 \times 10^{-9} < 0.05$), and elongation at break ($p = 0.01 < 0.05$). The measured values for Young's modulus, UTS and yield strength, and elongation at break are shown in Figures 4.14, 4.15, and 4.16 respectively.

The impact of angle on the Young's modulus is very significant, but moderate. The samples printed at 20° have an average Young's modulus of 52.3 GPa, 76% of what was

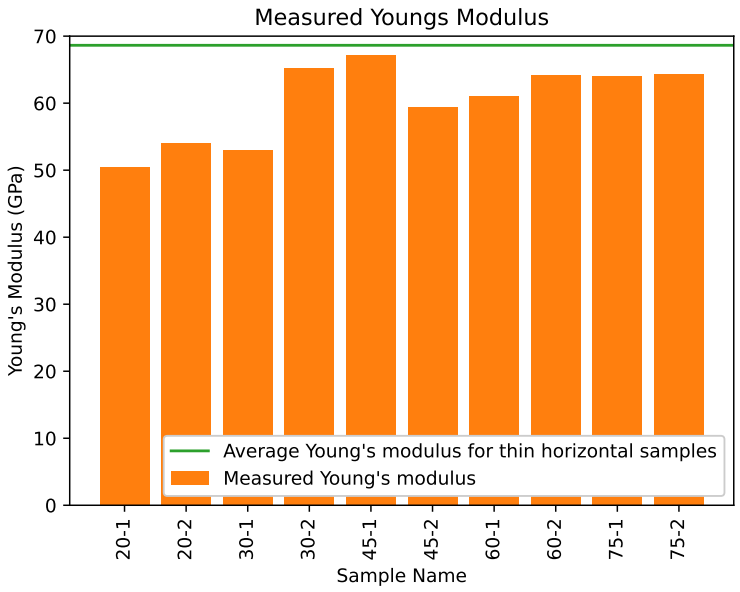


Figure 4.14: Young's modulus measured for each overhang sample using cross-section from CT.

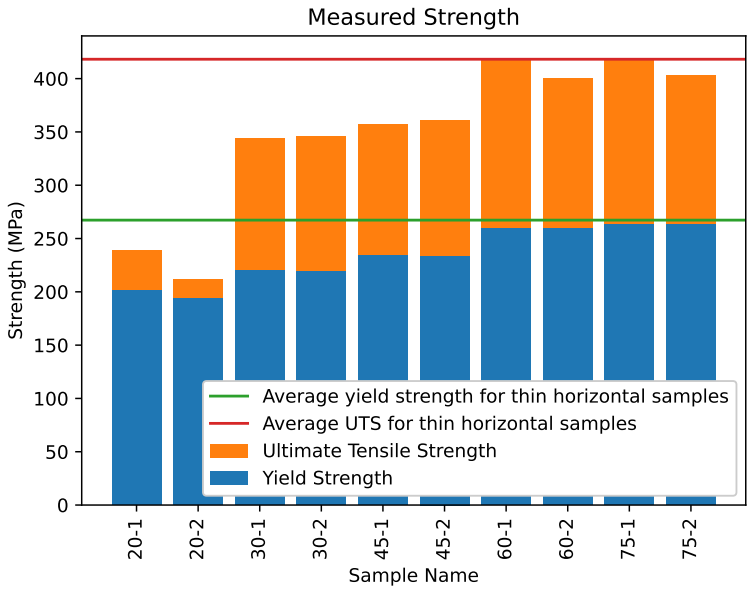


Figure 4.15: Measured UTS and yield strength for overhang samples.

measured for samples printed at 90° (the thin horizontal samples), while the average yield strength of the 20° samples is 197.67 MPa, 74% of the average for the thin horizontal samples. In comparison, the effect on ultimate tensile strength and % elongation at break is severe. The samples printed at 20° have an average UTS of 225.1 MPa, only 54% of the 418.2 MPa observed for the thin horizontal samples. The average elongation at break was 1.1%. This is only 19% of the 5.9% observed for the thin horizontal samples and is extremely concerning from a design perspective as it indicates very low fracture toughness [105].

There are a number of factors which are expected to contribute to these results. The first is the significant increase in surface roughness at steeper overhang angles. High surface roughness results in larger amounts of bumps, spatter, and voids, which result in material

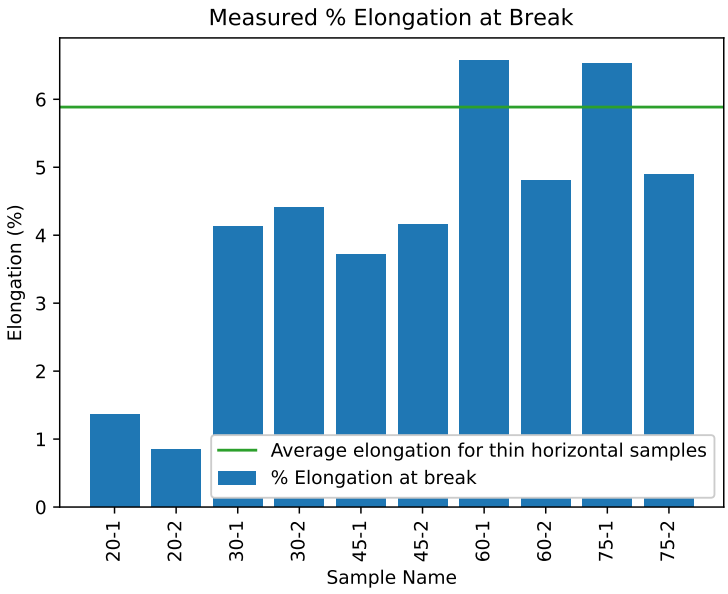


Figure 4.16: Measured elongation at break for overhang samples.

that does not effectively contribute to the load path and creates stress concentrations within the sample. Previous work also observed higher levels of subsurface porosity for these process parameters at steep overhang angles (Chapter 3). In addition to reducing the functional cross-section of the sample, which will effect yield and Young's modulus, these defects also encourage crack propagation, further reducing the UTS and elongation at break [106], [107].

Printing at steep overhang angles also has a significant effect on cooling rates as discussed in previous work (Chapter 3). As such, there may be a change in microstructure that will affect the material properties [108]. When the 20° samples were cut from the build plate, they were visually warped towards the upward facing surface. This indicates that the difference in cooling rates during the printing of the samples likely resulted in residual

stress buildup within the sample which is likely to affect the measured tensile properties.

These results indicate that extreme caution should be exercised when designing thin overhanging structures that must handle significant loading. The coupling of reduced cross-sectional area measured at steep angles with the reduction in tensile properties means that parts are likely to have less strength than expected while enduring higher than expected stress, increasing the chances of failure.

4.3.6 Effect of Coupon Type and Process Parameters on Tensile Properties

Due to costs, none of the vertical samples were scanned using CT. For the round samples, this is not a concern since they were precision post-machined on a CNC lathe, and the smooth surface finish allows accurate measurement with calipers. For the flat coupons, the same correction based on the average deviation of 54.1 µm between CT and designed dimensions was used. Since the sides of the flat samples are as-printed, and not waterjet cut, the correction is also applied to the width of the sample, with the cross-section of all the flat samples being assumed as 6.0541 × 3.0541 mm. Figures 4.17, 4.18, and 4.19 show the measured Young's modulus, UTS and yield strength, and elongation at break respectively.

Effect on Young's Modulus

A significant effect on the Young's modulus due to both the coupon type (round and machined vs. flat and as-printed, $p = 0.0029 < 0.05$) along with recipe used (Recipe 1 vs Recipe 2, $p = 0.012 < 0.05$) was found. The round coupons had an average measured

Young's modulus of 68.3 ± 0.9 GPa, 4.0% higher than the 65.6 ± 1.4 GPa measured for the flat coupons. Given that the two coupon types are printed directly beside each other and are of similar size, there should be no difference in the actual material properties. Instead, the error is likely due to a combination of three factors. The first is that the assumed cross-section correction based on the CT scans of the horizontal samples may be slightly off. The second is that, as discussed in Section 4.3.5, the measurement of cross-section using CT gives the true average area, including from spatter and other parts of the surface roughness which are not in the load path of the sample. Therefore even if the cross-section correction based on CT is correct, part of the area of the flat samples will not be fully stressed. Finally, the nature of a round coupon may more evenly distribute stress through the sample. Coupons printed with Recipe 1 had a Young's modulus of 68.0 ± 1.0 GPa, 3.2% higher than the 65.9 ± 1.5 GPa measured for coupons printed with Recipe 2. Research has shown that material properties can be tailored by modifying the process parameters used for printing [27], [97]. Given the two recipes use significantly different laser powers and speeds, this minor difference is unsurprising.

Effect on Strength

A highly significant effect on yield strength due to the recipe used was observed ($p = 1.97 \times 10^{-12} < 0.05$), although no effect due to coupon type was found. Samples printed with Recipe 1 were found to have an average yield strength of 242.0 ± 1.7 MPa, while samples printed with Recipe 2 had an average yield strength of 220.0 ± 1.5 MPa, 9.1% less than those printed with Recipe 1. Notably, Recipe 2 operates at considerably higher power and lower speed than Recipe 1. While modeling of the cooling rate of these process parameters is beyond the scope of this work, it is expected that Recipe 1 achieves a higher cooling rate, which has been shown to increase yield strength [97].

Interestingly, the opposite was found for UTS, with only a significant effect due to coupon type being measured ($p = 4.5 \times 10^{-5} < 0.05$). The round coupons had an average measured UTS of 443.5 ± 12.3 MPa, 11.3% higher than the 398.3 ± 10.2 MPa measured for the flat coupons. A similar significant effect on % elongation at break due to coupon type was also observed ($p = 1.3 \times 10^{-4} < 0.05$). The round coupons had an average elongation at break of 6.6 ± 0.9%, 72% higher than the 3.9 ± 0.4% measured for the flat coupons. This aligns with literature, which has shown that an increase in surface roughness leads to a reduction in UTS and elongation [107], [109]. Given that in Section 4.3.4, no correlation between UTS and sample thickness could be found, it may be more accurate for engineering applications designing parts that retain an as-printed surface finish to rely on the UTS results from as-printed tensile samples, since machined samples may over-predict part strength.

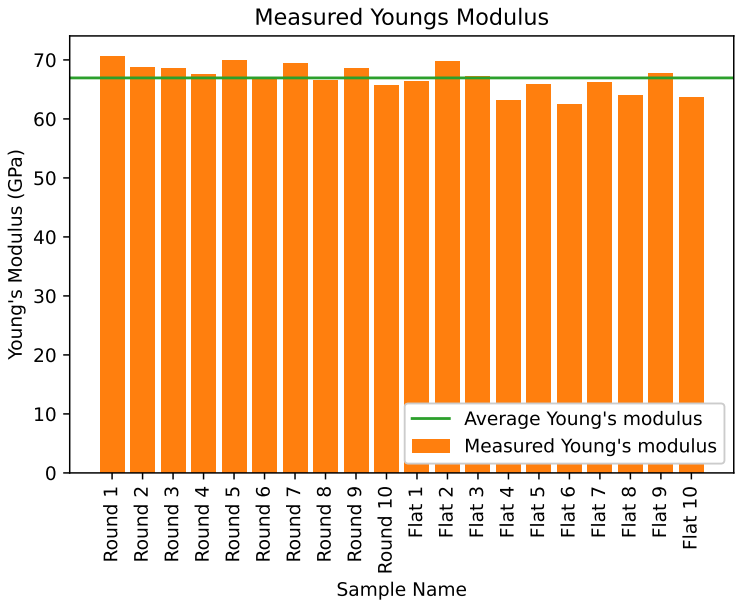


Figure 4.17: Measured Young's modulus for all vertical samples. The average Young's modulus is 66.9 ± 1.0 GPa.

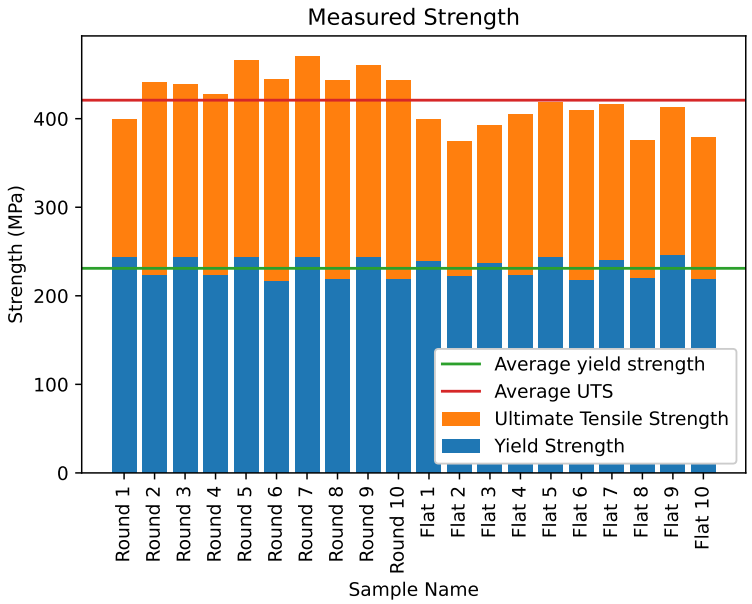


Figure 4.18: Measured UTS and yield strength of vertical samples. The average UTS is 420.9 ± 12.9 MPa, and the average yield strength is 231.0 ± 5.0 MPa.

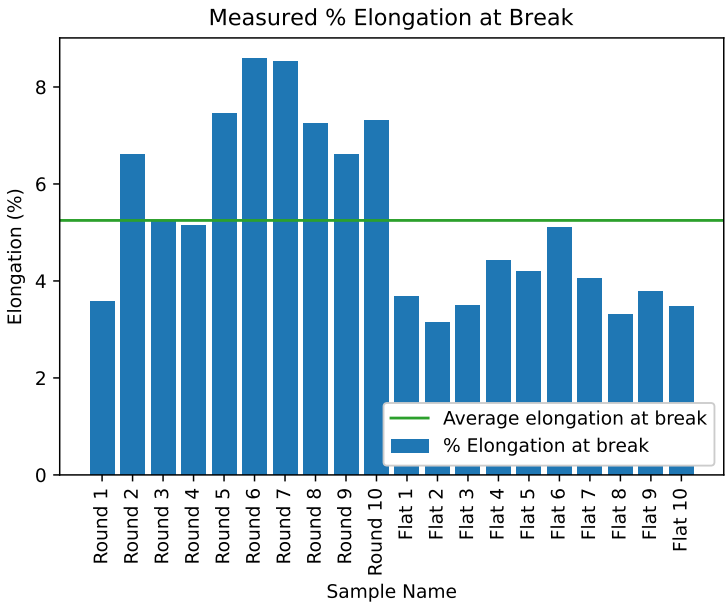


Figure 4.19: Measured elongation at break for all vertical samples. The average elongation is 5.2 ± 0.8 %.

4.4 Conclusions

In this work, the tensile properties of as-printed AlSi10Mg samples have been investigated to determine the effect of wall thickness, part orientation, and height above the build plate. A number of other factors have been investigated, including the effect of part angle relative to the build plate, as well as a comparison of two different sets of process parameters and machined vs as-printed tensile samples. The key findings of this work are summarized as follows:

1. Significant effects due to part orientation on surface roughness were found. Samples printed along the Y axis had a 13.5% reduction in surface roughness compared to

those printed along the X axis. For parts along the X axis, the face pointing into the recoater was 7.9% smoother, while along the Y axis parts facing into the gas flow were found to be 7.2% rougher. No effect on roughness due to part thickness was measured and while a significant effect due to height above the build plate was found, it is expected that this is erroneous and due to spatter generation from shorter samples.

2. Manual measurement of as-printed tensile coupon thickness was found to result in significant error correlated to the surface roughness of the part which results in erroneous tensile property measurements. By using limited CT measurements, a dimensional correction could instead be made against the as-designed dimensions to provide an accurate cross-section from which to work.

3. The tensile properties for a set of process parameters optimized for low surface roughness and the ability to print complex structures as presented in previous work have been characterized (Chapter 3), [15]. A summary of the Young's modulus, yield strength, UTS, and elongation at break in both the X-Y plane, and along the Z axis can be found in Table 4.6. No significant effect due to orientation in the X-Y plane, and sample thickness was found on the UTS, and while a significant effect on yield strength was found, this was due primarily to the very low variance in the yield strength data, and the differences of 0.4% and 0.6% are unlikely to be worth consideration for practical engineering applications.

4. Samples printed at steep overhang angles relative to the build plate were found to have significantly reduced thickness and tensile properties. At 20°, not only were the samples 34% thinner, but there was a 26% reduction in yield strength and a 24% reduction in Young's modulus. Even more concerning was the 46% reduction in

UTS and the 81% reduction in elongation at break. This shows that significant care should be taken when designing thin overhanging structures which must withstand significant loading, such as the TPMS heat exchangers and closed impellers discussed in the introduction of this work.

5. Recipe 1, which was optimized for low surface roughness, productivity, and overhang angle performance, was found to have a 9.1% higher yield strength than Recipe 2, which was optimized for high part density, with no significant difference in UTS or elongation at break.

6. While coupon type did not have an effect on measured yield strength, it had a significant effect on UTS and elongation at break. Flat, as-printed samples had a UTS 11.3% lower than was measured for round, machined samples and as-printed samples also had a 41% reduction in elongation at break. While this demonstrates why most literature and industry prefer to machine printed tensile coupons, it also shows how this may lead to the over-prediction of the tensile properties of as-printed structures and demonstrates the need for tensile properties that are representative of end use applications.

Table 4.6: Summary of tensile properties for as-printed parts manufactured using Recipe 1.

Property	**X-Y Plane**	**Z Axis**	**Units**
Young's Modulus	69.8 ± 0.7	66.6 ± 0.6	GPa
Yield Strength	265.6 ± 1.0	242.0 ± 1.7	MPa
Ultimate Tensile Strength	422.1 ± 4.1	408.0 ± 9.2	MPa
Elongation at Break	6.1 ± 0.4	3.8 ± 0.2	%

Chapter 5

Research Applications

The purpose of this chapter is to provide practical examples of how the research presented in the previous three papers has been applied to solve real world problems. It is meant to present a less formal demonstration of some interesting examples of how this research has been applied and to provide some empirical observations that may be of use in directing future research.

Many of the projects discussed in this chapter are in collaboration with the Waterloo Rocketry team. Waterloo Rocketry is a student design team based out of the University of Waterloo comprised of approximately 100 undergraduate students in various engineering disciplines and other programs. The mission of the team is to enable its members to become better engineers by providing students with the opportunity to gain practical hands-on experience working on aerospace projects. Currently, the team competes in the advanced division of the Launch Canada student rocketry competition, held each year in Timmins Ontario. Since its inception in 2009, the team has achieved a number of remarkable successes. The team has won countless awards, placing between first and

third in every competition since 2017. Most notably, the team launched the first ever Canadian-built liquid rocket, Borealis, at the 2024 Launch Canada competition[1][2]. This is a significant milestone in the history of Canadian aerospace as liquid rockets, which use a combination of liquid fuel and liquid oxidizer to produce thrust, are the most widely used type of propulsion for satellite launches due to their high efficiency. At the time of writing, the team is finishing their next rocket, Aurora, slated to fly in August 2025. Aurora will be the second Canadian-built liquid rocket to fly from Canadian soil. It aims to set a new record for performance with a target apogee of 50,000 ft. To do so, it features multiple components manufactured using AlSi10Mg as discussed later on in this chapter.

5.1 Turbopump

In 2024, a group of five Waterloo Rocketry members set the goal of successfully testing the first ever amateur-built turbopump for their capstone project. A turbopump is a critical piece of machinery used in large rocket engines to pump fuel and oxidizer into the combustion chamber of the engine. It consists of a hot gas generator which burns a small amount of fuel and oxidizer to produce large volumes of hot gas. This gas is then directed through a series of de Laval nozzles which accelerate it to supersonic velocities before impinging on a turbine blade, generating substantial torque at very high rotation rates. The turbine blade is coupled to a pump assembly via a shaft through a complex assembly of bearings and seals. The pump consists of three primary components: the inducer, which induces flow in the pumped propellant to prevent cavitation, the impeller,

[1]Media about the launch can be found at: https://uwaterloo.ca/engineering/news/student-rocketry-team-launches-canadas-first-liquid-rocket

[2]Video of the flight can be found at: https://www.youtube.com/watch?v=Z126ZESX3uA

which is responsible for accelerating the fluid radially outwards, converting the mechanical energy from the shaft into fluid power, and the pump housing, which encases the inducer and impeller and contains a volute which directs the flow out of the inducer and into the plumbing downstream of the pump. Turbopumps are notoriously difficult to successfully design and build. They operate at extremely high speeds and temperatures, and many of the components require tolerances on the order of 10 µm to prevent the pump from leaking severely or shaking itself apart.

The team aimed to build a turbopump capable of operating at 35,000 RPM, powered by a 64 kW gas turbine. This would pump 9.36 kg/s of water (a proxy for the ethanol fuel used when integrated into a complete rocket engine), while generating a pump head pressure of 40 Bar. Figure 5.1 shows a cross-section of the complete turbopump assembly. Given the budget and scale of the project, there were four key parts that the team identified as needing to be manufactured via LPBF: the turbine housing containing the hot gas manifold and de Laval nozzles, the impeller, the inducer, and the pump housing. The Multi-Scale Additive Manufacturing (MSAM) lab sponsored the printing of these components and, as a member of both Waterloo Rocketry and the MSAM lab, this author served as the principle design for additive manufacturing (DfAM) engineer for the project. One interesting aspect of the project was its very large scope. The other design applications discussed in this chapter could be completed by a single designer incorporating both the functional and DfAM components of the design work. Due to the complexity of a turbopump, this was not possible and instead design responsibilities for each part were split between the turbomachinery designer, and the AM designer.

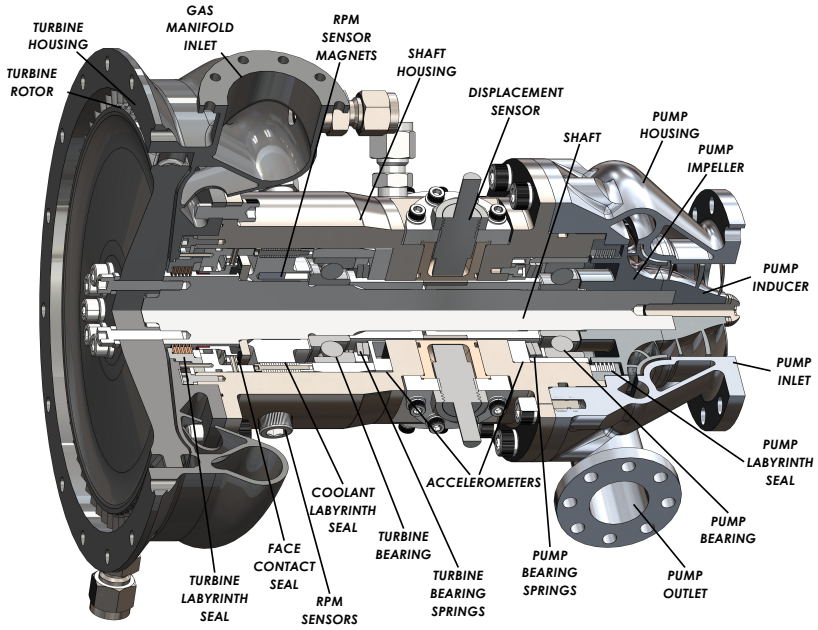


Figure 5.1: Cross-section of the Waterloo Rocketry turbopump assembly. The turbine housing, pump inducer, pump impeller, and pump housing were manufactured using LPBF.

5.1.1 Turbine Housing

The turbine housing is the largest single component of the turbopump. Designed to direct the 730 °C hot gas from the generator to power the turbine, it was printed from Inconel 625 to ensure it could handle the high operating temperature. The part design incorporates a number of key DfAM considerations and a cross-section of one of the printed housings is shown in Figure 5.2. A teardrop-shaped manifold was used to eliminate steep internal overhang angles where supports could not be removed. The top flange was designed to use a 45° flare to eliminate the need for supports. Holes that needed to be post-machined used a diamond shaped pilot hole, which eliminates steep overhangs but is still symmetrical to prevent the drill bit from wandering during machining, as has been used in literature [18]. To reduce weight and, more importantly, material usage and print time, solid sections of the housing were replaced with a diamond TPMS lattice which still supported the surrounding structure while reducing material usage.

Since the turbine housing is a very large part and Inconel 625 is a very expensive material, ensuring the part would print successfully was of very high importance. Due to post-machining and assembly requirements, it was decided that it was best to print the housing with the turbine recess facing upwards. This meant that the complex curvature of the hot gas manifold faces downwards and most of the part needed to be printed on support material. Due to the size of the part, it was deemed that traditional, easily-removed supports may crack and fail, as has been observed in other projects, and that this risk needed to be eliminated due to the price of the part. As such, a set of thin diamond TPMS lattices, similar to those used within the part were designed to support the part. While they require significantly more labor to cut off using a rotary tool, this was deemed a worthwhile tradeoff, as the student project had more volunteered time than funding.

Another concern was the hot gas nozzles which resulted in steep overhangs. While minor adaptations to the hot gas nozzles could be made to improve manufacturing, their geometry was largely fixed by the performance requirements of the system and resulted in slightly concerning overhangs. To address this, another DfAM technique used was a geometry test sample. A short print was run using the reduced build volume of the LPBF system (AM400, Renishaw, UK) to test if the nozzles would print correctly or were likely to cause the print to fail. A small cross-section of the housing was taken, including many features of concern, such as the nozzles, overhanging de-powdering holes, and the lattice supports. Not only did printing this sample confirm that the nozzles and other difficult geometry would print successfully, but it also allowed testing removal of the novel high strength lattice supports, confirming they could be cut off reasonably quickly.

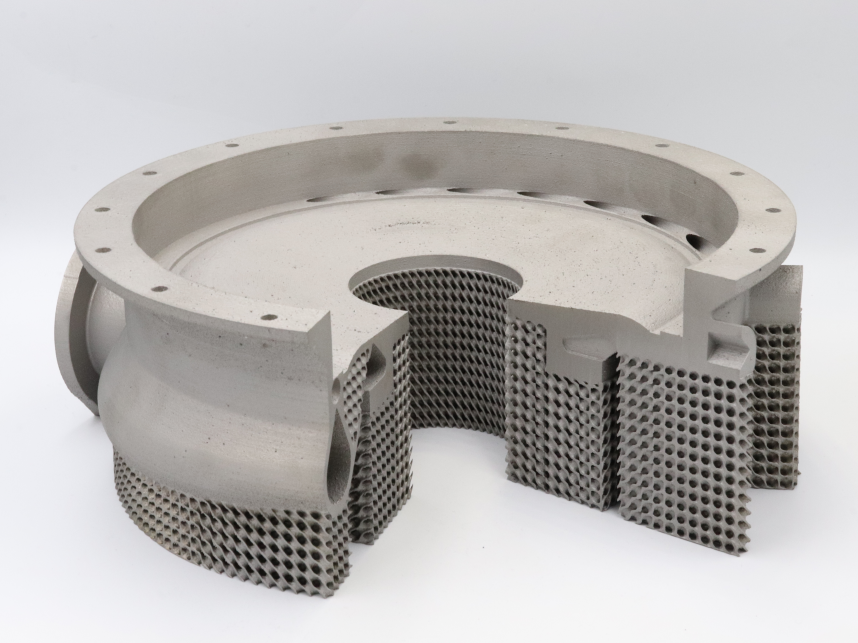


Figure 5.2: Cross-section of turbopump turbine housing printed from Inconel 625 with lattice supports still attached. A teardrop shaped manifold is used to direct hot gas to the nozzles.

5.1.2 Inducer and Impeller

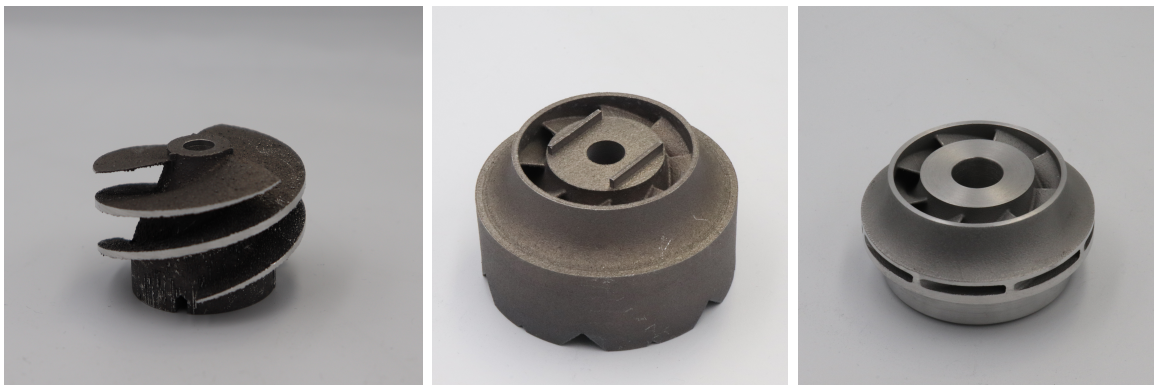
Printed from AlSi10Mg and shown in Figure 5.3, the inducer and impeller were the two most difficult components of the turbopump to print. This was because their geometry was almost entirely defined by fluid dynamics and the required pump flow rate, pressure, and rotation speed. Any attempt to modify the internal geometry of these parts to improve manufacturing resulted in a drastic reduction in simulated pump performance.

Known as a closed impeller, the impeller features a shroud over the main pump vanes which drastically increase efficiency compared to an open impeller. This however results in

a series of narrow internal channels which require good surface finish, and bend 90° between the axial inlet at the top of the impeller, and the radial outlet around the perimeter of the impeller. As such there is no print angle which does not require a near horizontal (0°) overhang angle. Due to the thin bent nature of the internal channels supports deep inside cannot be accessed for removal. While also desirable for other industry projects, this need for low angle, support free printing was one of the primary drivers for the research conducted in Chapter 3.

Based on the successful identification of process parameters in Chapter 3 which allowed printing as angles low as 20° with reasonably good surface finish, it was possible to print the impellers with only very thin support structures that penetrated only 2.5mm deep into the channels. A sacrificial shroud was placed around the exit of the impellers during printing to ensure that the upper shroud was well supported and did not warp given the extremely minimal supports. Figure 5.3 (a) and (b) show the impeller before and after machining respectively. Once the sacrificial shroud was machined away, the supports could easily and quickly be removed with nothing more than a precision flat-head screwdriver, as well as a diamond file used to smoothen rough faces.

Like the impeller, the inducer also used a sacrificial shroud which was printed around the blades to support them and then latter machined away. The inducer is the part of the turbopump that could use the most improvement from an AM perspective. While it was successfully printed, due to the very low angle of the blades, even with optimized downskin parameters tested down to 20 degrees, it still required supports under the entirety of the blades. These supports then required significant manual post-processing to remove, made particularly difficult by the need for a smooth and accurate surface on the supported faces. If process parameters could be identified capable of printing at angles as low as 10°, this would the allow the inducer to be printed nearly support free. Given the findings of



(a) (b) (c)

Figure 5.3: Turbopump inducer and impellers printed from AlSi10Mg: (a) Inducer after machining and support removal. (b) Un-machined impeller in the as-printed state. (c) Impeller after machining and minimal support removal.

Chapter 3, it is believed that this may be possible with further research. Similar to the turbine housing, the most difficult cross-sections of the inducer and impeller where printed using a short reduced build volume print, which confirmed that the process parameters developed in Chapter 3 would be successful.

5.1.3 Pump Housing

Also printed from AlSi10Mg, the pump housing is likely the simplest printed component of the turbopump, although this is in part because it is a good example of effective design for AM. With AM and turbomachinery designers working together as a team and considering AM from the start, any need for complex support structures or difficult to print geometry was eliminated. Print orientation was considered throughout the design process and the part was designed around a tear-dropped shaped volute similar to the turbine housing.



Figure 5.4: Turbopump pump housing printed from AlSi10Mg. Supports have been removed but post-machining has not been completed.

Additional material for bolt holes and support ribs were angled to avoid the need for any unnecessary supports, while standard supports were used on the inlet flange since they were easy to access and minimized material use. The final part is shown in Figure 5.4.

There is one notable feature on the pump housing that warrants discussion. As shown in Figure 5.5, there is a very obvious and sharp line along the part where the scan strategy abruptly transitions from downskin to sideskin. While in this case it is only cosmetic and not of concern, the transition line creates a detectable protrusion and it can be seen that there is attached spatter at the transition point. This could be a concern for some high precision part designs and demonstrates the importance of developing strategies that allow smooth transition across donwskin angles, as discussed in Chapter 3.



Figure 5.5: Turbopump housing showing showing distinct line artifact at the point where the downskin scan strategy is disabled.

5.1.4 Results and Future Work

The team of students behind the project accomplished a truly staggering amount of work, designing not only all of the turbopump hardware but also all of the infrastructure, plumbing, electrical, and control systems required to test and operate it. The team successfully used this infrastructure to test the bearings and seals of the turbopump at the full speed of 35,000 RPM with full simulated pressure loading. Unfortunately, the team ran our of time before they could test the AM components of the pump described in this section. However, since the project was associated with the Waterloo Rocketry team, it is expected that another generation of students will pick up where the original team left off within the next couple years. While it is likely that some or all of the parts will be re-designed for the next iteration of the project, most of the work spent developing the methodologies required to design these parts will be retained and applied to the new designs. In particular, the ability to successfully manufacture high quality closed impellers is a significant milestone

that is expected to be needed for future projects.

5.2 Flight Longerons

Based on the result of the first paper presented in this work (Chapter 2), which showed that significant performance improvements could be made by optimizing structural member geometry via additive manufacturing, Waterloo Rocketry, in collaboration with MSAM, chose to print the longerons for their 2025 rocket, Aurora. The Aurora longerons are based on the design originally described in Chapter 2, but with a different load case and mounting requirements. The maximum compressive load per longeron for Aurora is 11.03 kN. Figure 5.6 shows the Aurora injector section in which the longerons are mounted. Unlike the Leviathan of the Sky (LotS) longerons described in Chapter 2, these longerons are asymmetrical along their length since the upper and lower bulkheads to which they mount have two different diameters and mounting configurations on Aurora. They are also slightly shorter at 129 mm long compared to 161 mm for LotS. Finally, one of the biggest differences is that the aurora longerons incorporate mounting points for the aerodynamic panels that cover the injector section.

Since the structural optimization work presented in Chapter 2 predated the roughness optimization and tensile property characterization presented in Chapters 3 and 4, reasonable assumptions had to be made about appropriate process parameters and assumed material properties. As such, the process parameters referred to as Recipe 2 in Chapter 4 were selected since they provided a slightly better density despite significantly inferior surface roughness. It is now known that the optimized parameters referred to as Recipe 1 provide superior tensile properties in addition to lower surface roughness and therefore better accuracy. This gives two additional benefits. Since the surface roughness is lower,

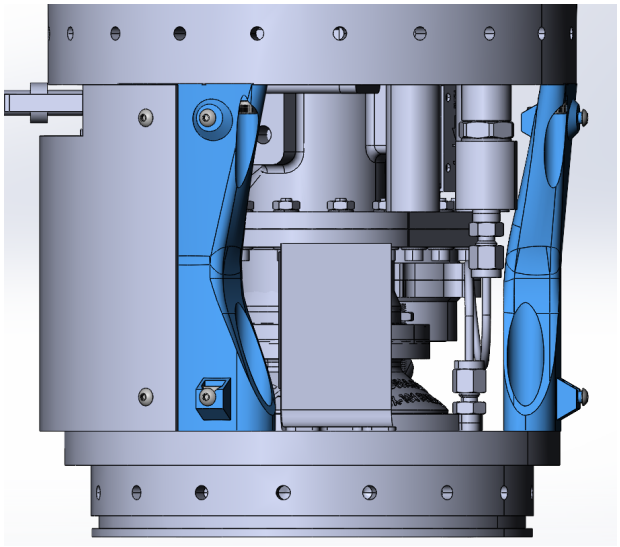


Figure 5.6: Aurora injector section assembly. Longerons are highlighted in blue. Note that the top coupler has a wider diameter than the bulkhead at the bottom, resulting in eccentric loading on the longerons.

the top of the longeron does not require post-machining as in Chapter 2. Second, since this recipe has been proven down to angles as low as 20°, more design flexibility is available for overhangs. For mounting of the aerodynamic panels, it was decided to use slots with T-nuts to eliminate the need to thread the longerons. Combined with no facing operation for the top of the longeron, this means that no post-machining is required and the longerons can be cut from the build plate and installed directly in the rocket. Because steeper overhangs have been well characterized, these T-nut slots make use of a number of steep 30° overhangs to reduce material use and therefore weight.

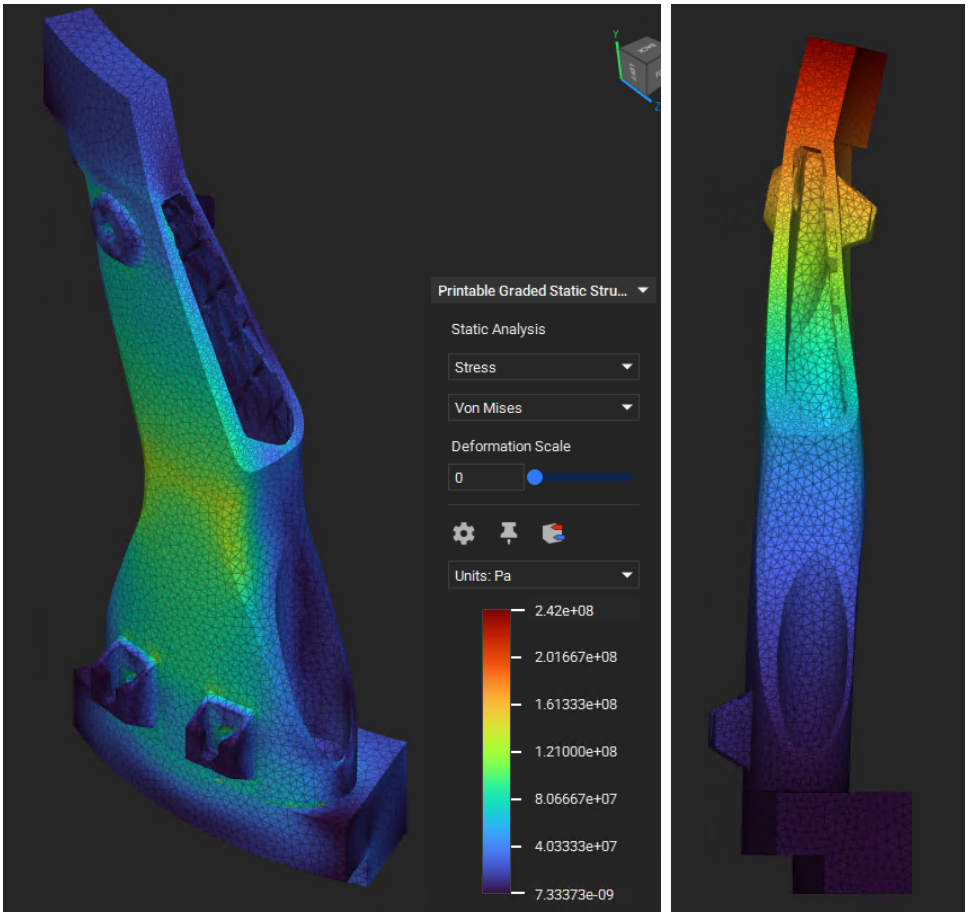
As a backup due to tight timelines, the team also developed a machined longeron for Aurora. Due to the difference in mounting location and shape between the top and bottom of the mount, the team struggled to design a machined longeron that could handle the load

while being easily machined. The result is a heavy block of aluminum weighing 276 g per longeron. In comparison, the printed Aurora longerons were designed very quickly and easily, since the methodology developed in Chapter 2 could be easily re-applied to this adjusted design space. The design was performed as follows:

- Starting from the initial outer CAD geometry used for the LotS printed longerons, the design was adjusted to match the new length and mounting locations for Aurora.
- The majority of the design effort was then devoted to design of the new aerodynamic panel mounting features.
- Once the design of the initial outer geometry was complete, it was imported into the previously developed workflow in the DfAM software package (nTop, NY, USA). Minor adjustments and fixes were quickly made to inputs to account for the geometry change and new loads.
- The software then automatically followed the procedure of running an initial stress simulation, computing a shell based on those results, applying latticing and design tweaks for printing, and finally simulating the performance of the final design. Since this is a practical design problem, there were unsuprisingly a few minor tweaks such as adjusting reference planes and other features that had not been well generalized to any input. In addition, the stress-thickness mapping function used to generate the functionally graded shell is somewhat input dependent and so required a few iterations of tweaking values to produce good results. Despite these minor fixes and adjustments, the majority of the workflow simply re-calculated a new design without intervention, resulting in a manual iterative optimization process that took many minutes instead of many hours.

Stress and buckling simulations for the final design of the Aurora longerons are shown in Figure 5.7. While the eccentric loading of the new longerons results in a less even stress distribution than originally achieved in Chapter 2, it is expected that the design will still significantly outperform any conventional design, while requiring minimal design effort. The final mass of the Aurora printed longerons is 113 g per longeron, representing a 59% reduction in weight compared to the proposed conventionally machined design.

With the updated design complete, the longerons were then printed. Figure 5.8 show the longerons after being de-powdered. At time of writing the longerons are in the process of being cut from the built plate and integrated directly into the rocket for final testing before flight in mid August 2025.



(a) (b)

Figure 5.7: Aurora longeron simulations with section view: (a) Von Mises stress analysis result. Scale maximum is set to 242 MPa, the Z axis yield strength identified in Chapter 4. (b) First buckling mode based on linear buckling simulation. The buckling load factor (BLF) is 7.99.

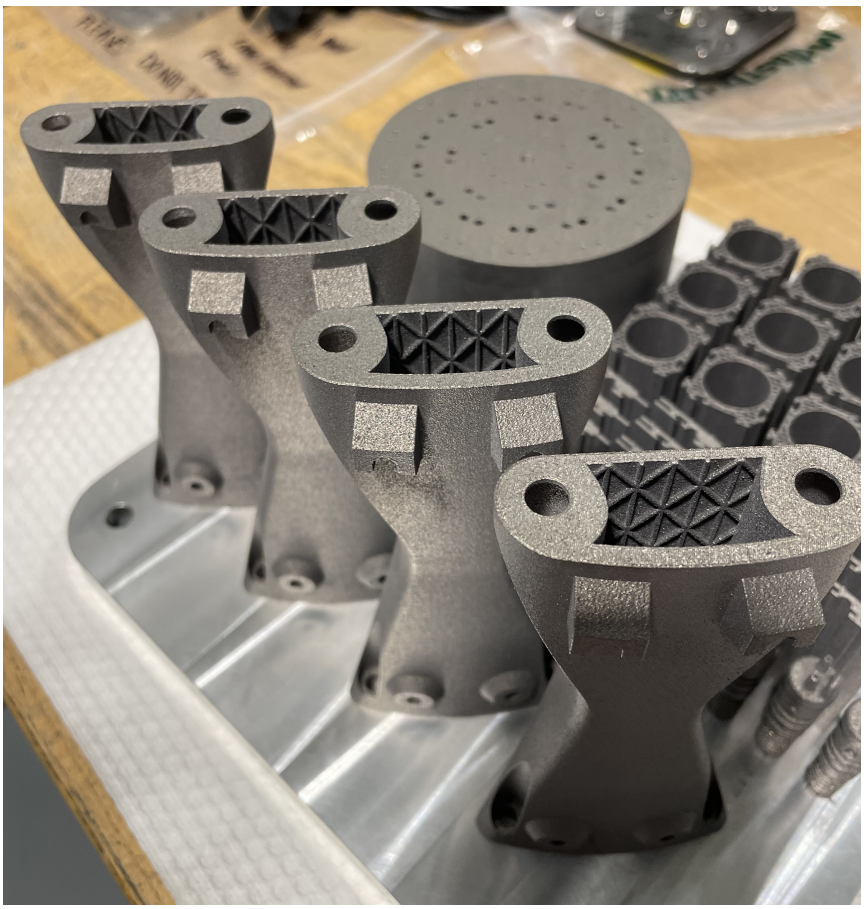


Figure 5.8: Aurora longerons on the build plate after de-powdering.

5.3 Printed Injectors

In January of 2025, Waterloo Rocketry approached MSAM due to difficulties with manufacturing the injector for the Eridium liquid rocket engine, which powers the Aurora rocket. The injector is the most complex component in the Eridium engine and is responsible for injecting the liquid fuel (ethanol) and liquid oxidizer (nitrous oxide) into the combustion chamber. This must be done at a precise rate and in such a way that combustion is even, efficient, and stable. To do this, a large number of small individual injector elements are required to ensure the propellants are rapidly atomized and mixed. The team had planned to manufacture the injector using a set of hypodermic needles brazed into brass plates to direct the fuel flow, with a small annular gap in the injector face around these needles providing the metering orifice for the oxidizer. Referred to as a co-axial shear injector, it uses the shear forces due to the two different exit velocities of the propellants to promote mixing. The planned assembly, shown in Figure 5.9, was comprised of over 50 parts and while the team had been successful in small scale brazing tests, they were having extreme difficulty perfecting a process that would alow all of the elements to be brazed successfully into a larger plate without blockages or other defects.

Given the difficulties encountered with traditional manufacturing, the team decided to collaborate with MSAM and attempt to manufacture the injector using LPBF. The team decided to use AlSi10Mg to manufacture the injectors. The usage of an aluminum alloy with a melting temperature of 590 °C for use inside a combustion chamber with temperatures exceeding 2,000 °C may seem counterintuitive, but the relatively high thermal conductivity of aluminum alloys, combined with the high flow rate of cool propellants through the injector, has allowed the development of a number of aluminum injectors for much more powerful rocket engines [110]. In addition, the work presented in Chapters 3 and 4 meant

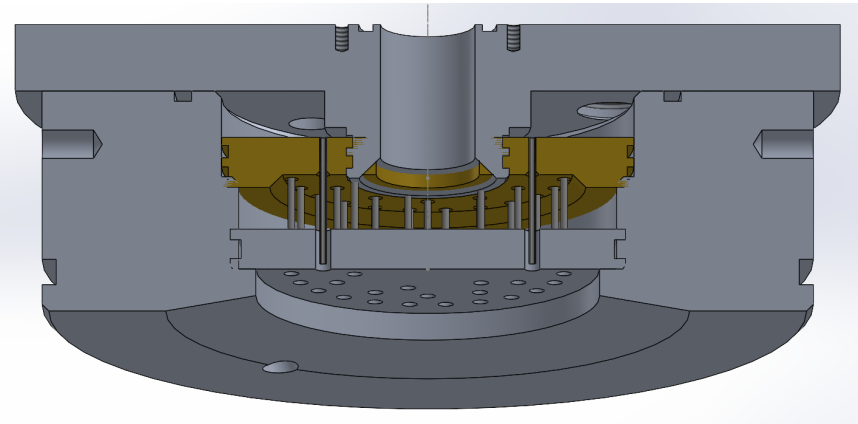
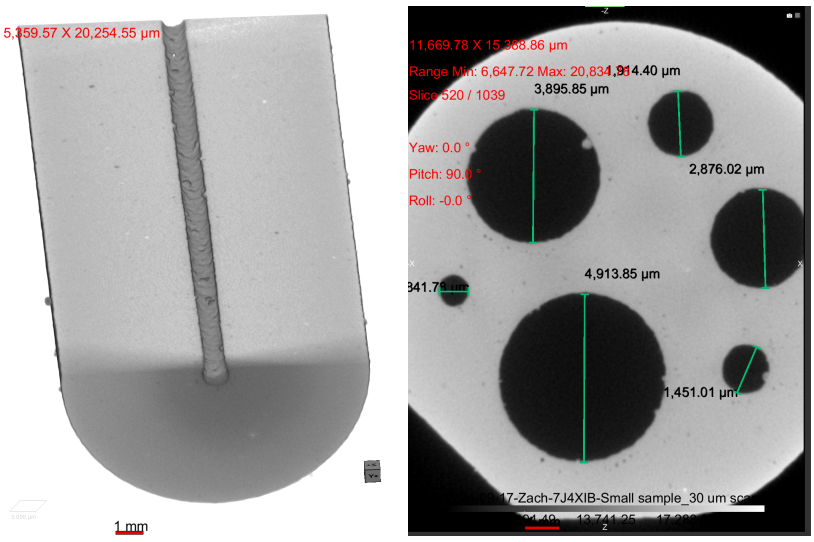


Figure 5.9: Initial brazed injector concept. 55 hypodermic needle tubes are brazed into a brass plate to form the fuel injector. These tubes pass through holes in a lower plate, forming an annular gap for oxidizer to flow through. A series of O-ring seals are used to ensure propellants don't mix.

that AlSi10Mg had the best available characterization data on its mechanical properties and surface roughness which were crucial to the project.

5.3.1 Channel Diameter Calibration

By far the the most difficult requirement of the project was the fuel injection orifices. To achieve the correct flow rate, fluid channels 0.9 mm in diameter were required. Channels as small as 0.5 mm have been printed using AlSi10Mg and confirmed to not be fully blocked [15]. However, printing 42 0.9 mm channels in a large component such that not only are none of them blocked but are also of accurate size and give the required flow rates is a significant additional challenge. Fortunately, a series of small diameter fluid channels ranging in size from 1 mm to 5 mm had been printed using the optimized Recipe 1 as part of the build presented in Chapter 4, and these samples had been CT scanned to



(a) (b)

Figure 5.10: CT scan results for small diameter fluid channels. (a) Cross-section of 1 mm as-designed channel 25 mm long. While some spatter is present, overall the channel is very uniform and free of concerning obstructions. (b) CT slice of sample showing measurements of all tested diameters.

investigate the quality of the channels. The results, presented in Figure 5.10, showed that channels with a designed diameter of 1 mm resulted in an average as-printed diameter of 0.86 mm, very close to the target of 0.9 mm. In addition, while some small spatter was observed, it was confirmed that channels as long as 25 mm were free of any obstructions that would significantly impact flow performance. By performing a linear regression on the measured diameters of the various channel sizes, a fixed offset of 105 µm was found between the as-designed and the as-printed channel diameters. This was used to compensate the as-designed size of the fuel and oxidizer orifices to ensure that the final printed channels accurately matched the required hole sizes based on flow-rate calculations.

5.3.2 Injector Design and Testing

Once it had been confirmed that appropriately sized channels could be printed with acceptable quality, the re-design of the injector for AM was commenced. Given the design freedoms enabled by AM, a number of design improvements were made. The largest change was switching from a co-axial shear injector to a more efficient like-unlike impinging injector, which has seen significant use for many decades [110]. In this injector, each element consists of two fuel holes and two oxidizer holes. The fuel and oxidizer hole pairs are angled towards themselves, causing the fuel to impinge on itself and atomize, while the oxidizer does the same. Each pair of elements is angled inwards, causing the streams of unlike atomized propellants to impinge on each other and mix. This provides very efficient mixing, but is traditionally very difficult to machine, a problem that is removed by using AM. Figure 5.11 shows a computational fluid dynamics (CFD) simulation of the injector to help visualize the flow.

The printed injector consolidates the over 50 parts from the original design into a single component. The two inter-propellant O-ring seals required for assembly of the original design are eliminated. This removes leak points that could result in the destruction of the engine. A total of 21 injector elements, each with 2 fuel and 2 oxidizer holes are incorporated into the 4" diameter injector. Since each orifice requires a length to diameter ratio of at least 10 for combustion stability [110], this tight packing is only possible due to the ability of the AM to create curved channels with tighter nesting.

The aluminum injector experiences very high heat flux from the combustion gases and is reliant on the propellant flowing through it to provide cooling and prevent the injector from melting. To ensure sections of the injector further from the orifices are well cooled, a series of regenerative cooling channels were incorporated into the design. Fuel flows

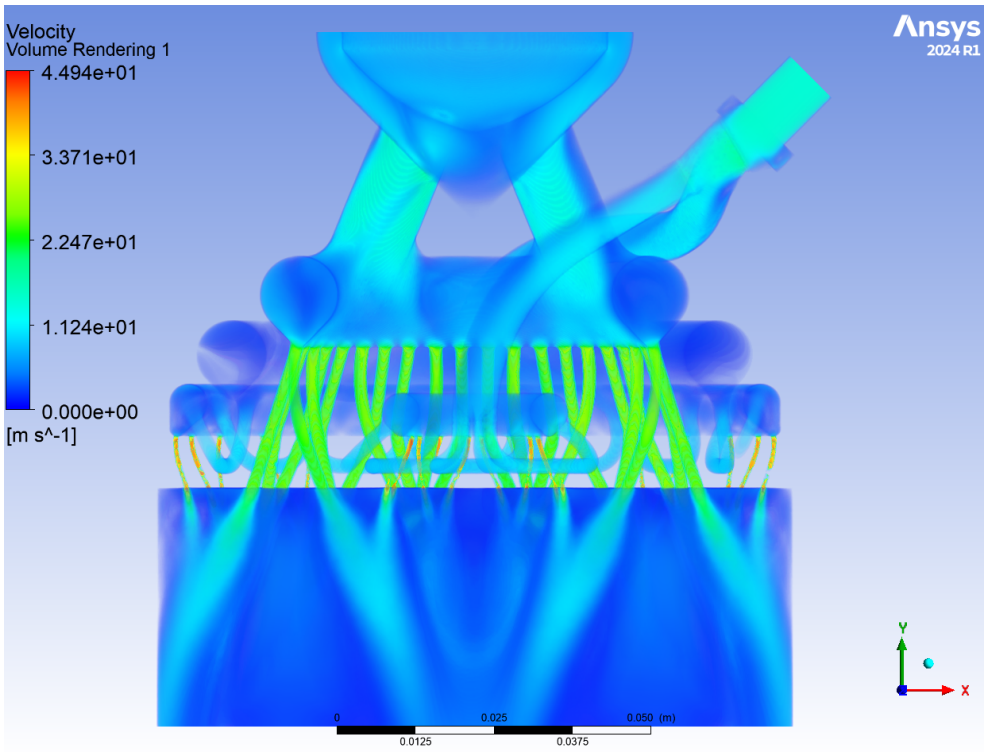
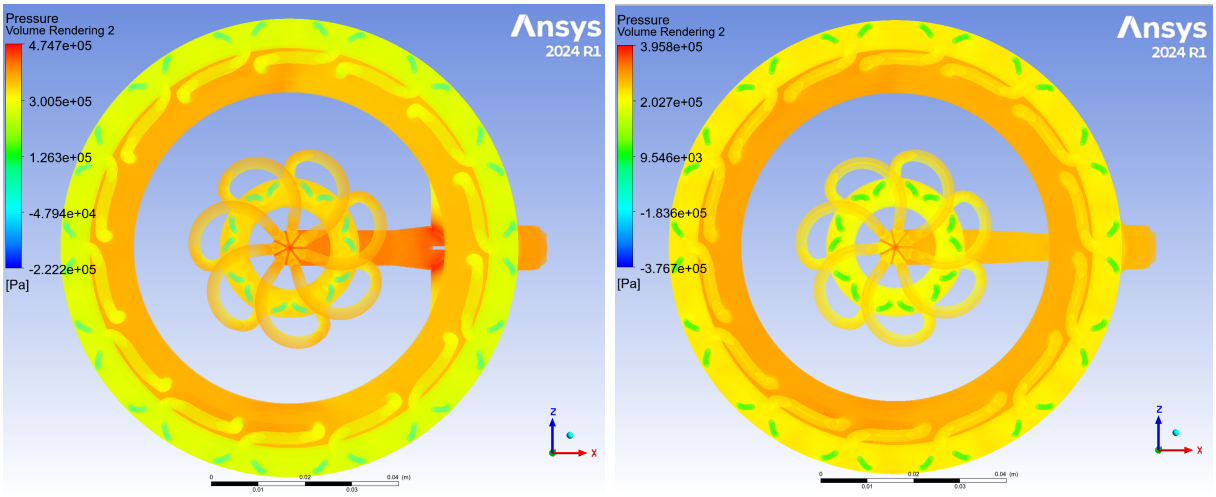


Figure 5.11: CFD flow visualization of printed injector. Oxidizer enters from the top of the injector, while fuel enters from a port in the upper right corner of the image. The rectangular volume at the bottom of the image is the combustion chamber, and the fuel and oxidizer can be observed impinging on one another.

through the injector as follows: Fuel enters through a port on the side of the injector, where it is split into three streams. One stream runs to the inner ring of the injector where 7 of the injector elements are located. The other two streams run to the outside of the injector to feed the other 14 elements. The outer two streams feed into the primary fuel manifold, where the flow is distributed before flowing into 14 cooling channels that run near the injector face. After passing through the outer cooling channels, the flow passes into the secondary outer fuel manifold, before then being injected into the engine via the fuel orifices. Meanwhile, the inner fuel flow is split 7 ways into the inner cooling channels, where it runs near the injector face before entering the inner fuel manifold and is subsequently injected into the engine. An important secondary effect of these manifolds and cooling channels is to ensure that fuel is evenly distributed to every element to prevent hot spots that could burn through the engine, a potential risk for the brazed design. To ensure even fuel distribution between the inner and outer rings, CFD simulation was used to iterate on the fuel inlet geometry as shown in Figure 5.12 and calculations using the roughness data collected in Chapter 4 were completed to ensure the pressure drop in the inner and outer cooling channels was even.

Once the design was completed, two copies of the injector were printed as shown in Figure 5.13. Two slightly different orifice sizes were used to ensure one would provide the required flow rates based on experimental testing. After the injectors were removed from the build plate, they were post-machined to add the required O-ring groves and threads. Testing was then conducted as shown in Figure 5.14[3]. First, a set of cold flow tests were conducted using liquid CO_2 and water as analogs for nitrous oxide and ethanol to confirm the flow rates through the injector. The injector was then integrated into the Eridium engine and a static fire test was conducted. The engine performed well, operating smoothly

[3]Video of the static fire test can be found at: https://www.youtube.com/watch?v=65qts5k77M0



(a) (b)

Figure 5.12: CFD simulation of pressure drop throughout the fuel channels of the injector used to refine the flow distribution. The fuel orifices can be seen as a low pressure region in green: (a) Initial fuel flow simulation. It was found that the fuel splitter resulted in uneven flow, with a disproportionate amount of fuel entering the inner fuel manifold. (b) Final fuel flow simulation. The fuel splitter (hidden from view by the outer manifolds) now results in an even pressure distribution between the inner fuel manifold and the secondary outer fuel manifold.

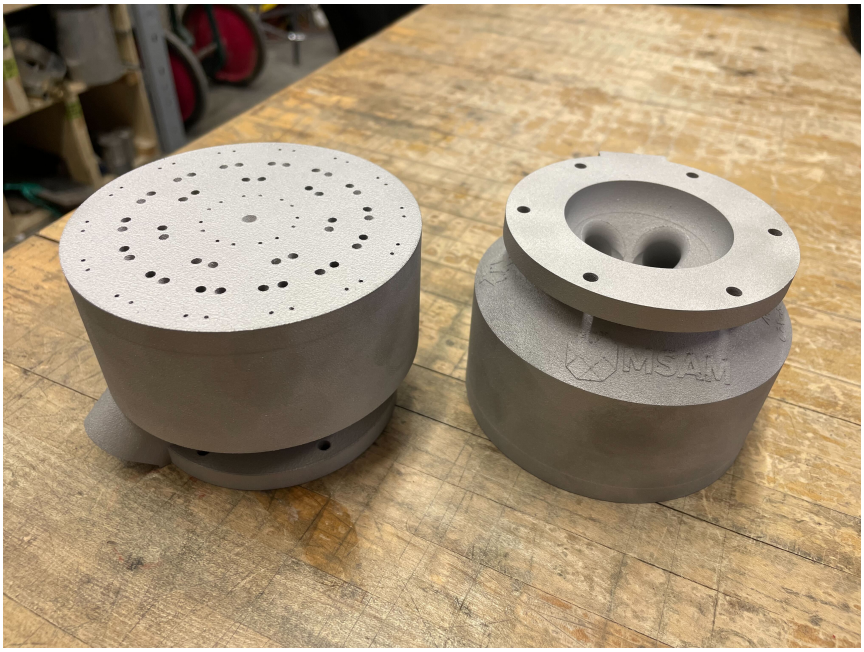
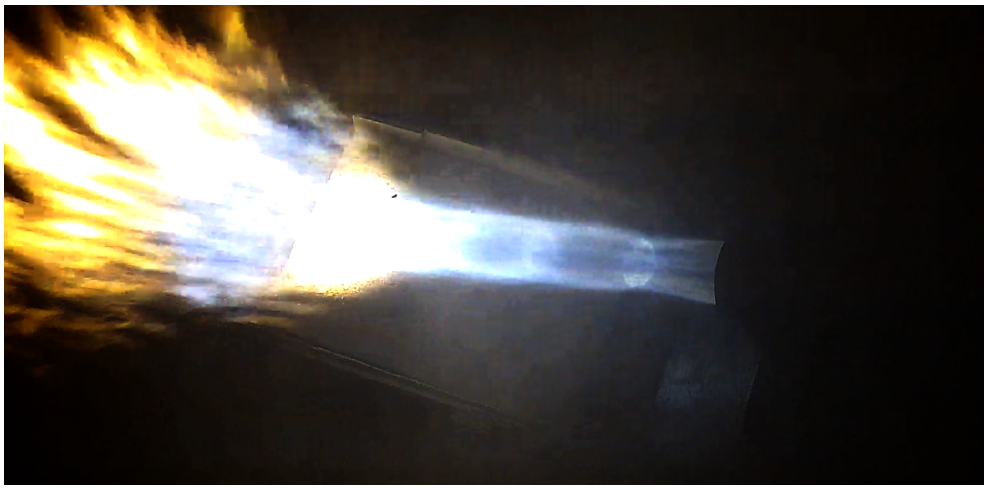


Figure 5.13: Printed injectors after being cut from the build plate but before post-machining.

with no significant combustion instability and achieved high combustion efficiency. The cooling system worked as intended and the injector did not melt. At time of writing the team is preparing for a final flight configuration static fire before integrating the injector into the rocket for flight in August 2025. The success of this design would not have been possible without the design flexibility offered by AM, as well as the optimization and characterization work conducted in the preceding chapters.



(a)



(b)

Figure 5.14: Eridium injector testing: (a) Cold flow testing of the fuel channels using high pressure water. The two fuel streams of each element impinge, resulting in atomization of the fuel. (b) Static fire of the Eridium engine using the printed injector. The engine operated smoothly, with high combustion efficiency.

5.4 Tronosjet Waveguides

In collaboration with Tronos Aviation, a set of waveguide demonstrators, shown in Figure 5.15, were printed to compare the downskin surface roughness of the optimized parameters identified in Chapter 3 (given the label Recipe 1 in Chapter 4), with a set of process parameters provided by the machine manufacturer, as well as to compare the effect of using a different LPBF system (RenAM 500S Flex) and powder. AlSi10Mg powder was used with a particle size distribution (PSD) of D10-D90 of 21-38 µm and a D50 of 31 µm. The process parameters used, along with the measured surface roughness are presented in Table 5.1. Surface roughness was measured using the same methodology previously described in Chapter 3, with a measurement area of 6 mm by 6 mm.

Interestingly, the Renishaw A process parameters performed the worst despite being predicted to have the best MDR[4]. While there are not enough samples to draw any firm conclusions, particularly since there are many differences between each of the tested process parameters, a few possibilities can be identified which would be worth further investigation in future work:

- Error in MDR prediction: It is reasonably likely that there may be errors in the predicted MDR since the absorptivity has not been calibrated for this specific powder. In addition, the work identifying an ideal MDR of 2 has all been focused on powder with a larger PSD and it is possible that it does not hold for all cases.
- Effect of velocity: While the Renishaw A process parameters have a good predicted MDR, they have a very low velocity. It has been empirically observed in past work

[4]Melt depth ratio (MDR) is presented and discussed in Chapter 3. Results found that an MDR of 2 typically lead to the lowest surface roughness for downskin surfaces.

Table 5.1: Process parameters and surface roughness (Sa) measurements for waveguide samples with 45° downskin. The system has a beam diameter of 80 µm. Renishaw B does not use a downskin strategy, so border strategy is listed as downskin.

Sample Code	**Recipe 1**	**Renishaw A**	**Renishaw B**
Core power (W)	255.3	350	350
Core point distance (μm)	60	90	40
Core exposure time (μs)	50	40	20
Core hatch distance (μm)	145	90	90
Core P_{eff} (W)	212.8	280	233.3
Core V_{eff} (mm/s)	999	1800	1333
Downskin Layers	5	6	2 contours
Downskin power (W)	400	100	245
Downskin point distance (μm)	50	40	40
Downskin exposure time (μs)	10	70	20
Downskin hatch distance (μm)	100	80	40
Downskin P_{eff} (W)	200	87.5	163.3
Downskin V_{eff} (mm/s)	2500	500	1333
Core MDR	2.11	2.78	2.82
Downskin MDR at 45°	1.54	2.13	2.62
S_a **Roughness** (μm)	**19.3**	**28.0**	**20.9**

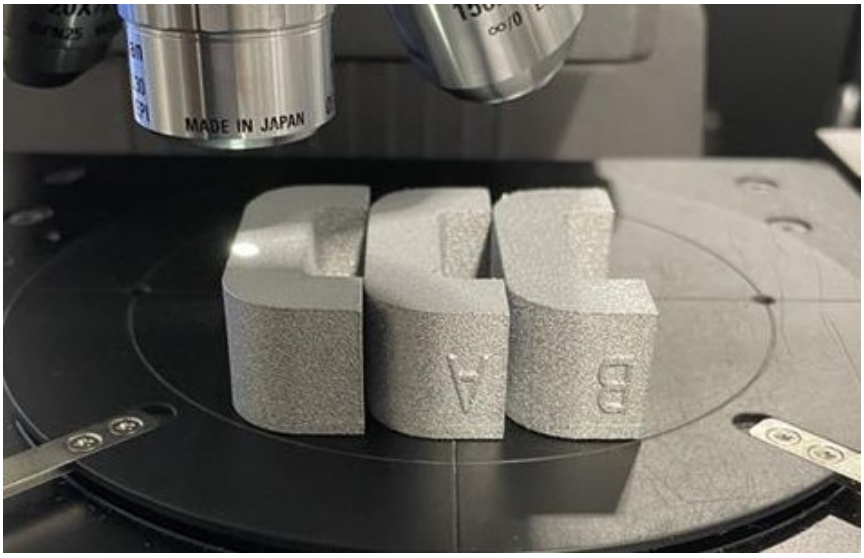


Figure 5.15: Surface roughness measurement of demonstrator waveguides.

that higher velocities tend to result in better surface roughness. Further investigation of the effect of velocity on surface roughness at a fixed MDR may be of value.

- Effect of other process mechanics: As has been identified in Chapter 3, at high downskin angles MDR may not be a good sole predictor of surface roughness since it does not seem to account for powder adhesion. 45° downskin is only moderately steep and it is possible that the ability of the process parameters to reject powder adhesion may also play a significant role.

Despite the difference in machine and powder from the original optimization, Recipe 1 outperformed the other two tested sets of parameters. In addition, Recipe 1 gave significantly better surface roughness than what was measured in the previous experiments presented in this work ($19.3\mu m$ vs $31.5\mu m$ at 45°). Given the largest anticipated difference is the change of PSD, this suggests that further investigation into the effect of PSD on downskin surface roughness may yield valuable results.

Chapter 6

Conclusions and Future Works

In this thesis, three important topics for the LPBF of AlSi10Mg have been explored to fill gaps in the existing body of knowledge related to the design and manufacturing of complex structures. A new approach for the design optimization of compressively loaded structural members was presented, optimized process parameters to enable printing at lower overhang angles were developed, and tensile properties representative of practical thin-walled components were assessed. Building upon previous research, the results of this work enable the printing of complex, high performance AlSi10Mg parts for use in aerospace applications, showcased through relevant demonstrators. Based on the research presented in this thesis, several novel components have been designed, printed, and tested and, at the time of writing, are being integrated into a rocket for flight in August 2025.

The key findings of this work are summarized as follows:

1. A conventionally manufactured structural member was re-designed using AM. The optimized AM design achieved a 98% increase in performance based on experimental testing. In doing so, a novel methodology for the design optimization of a structural

member under buckling conditions was presented, which may have broader applicability for similar applications. This methodology was then applied to a new structural member designed for functional service.

2. A test fixture was developed for the testing of compressive structural members under fixed-end free-end buckling conditions, enabling the experimental evaluation and comparison of their performance.

3. A new downskin melt pool overlap model was proposed which enables the use of previously developed techniques for predicting process parameter performance in the core of parts to be applied to downskin process parameter development.

4. The use of melt depth ratio (MDR) to predict process performance was expanded upon and the downskin melt pool overlap model was used to apply it to the development of downskin process parameters. It was found to be effective for this application, particularly at lower downskin angles. An MDR of 2 was found to be ideal across all downskin angles; however, it was identified that MDR alone is not sufficient for ensuring good surface roughness at high downskin angles.

5. Building upon past work [15], a combination of good process parameters were found which enable high density printing with low surface roughness across a wide range of angles. These process parameters allow printing at angles as low as 20° without supports. The tensile properties of parts printed with these process parameters were characterized and achieved consistent performance comparable to results published by industry with a measured yield strength of 265.6 ± 1.0 MPa in the X-Y plane, and 242.0 ± 1.7 MPa in the Z direction.

6. The tensile properties of thin samples printed at low angles were found to be problem-

atic for the design of complex structures. A significant reduction in part thickness and strength was observed, the combination of which results in parts drastically weaker than designed. In addition, an 81% reduction in elongation at break was observed between horizontal samples and those printed at 20°. This extremely low elongation at break means that features printed at these angles may be highly prone to failure if used for practical applications.

7. While no significant effect on yield strength was observed between as-printed and machined tensile coupons, significant reductions in UTS and elongation at break were measured for as-printed samples. While this demonstrates why most literature chooses to machine their tensile coupons to achieve these higher results, it also demonstrates the challenge of relying on those results for the design of components that will be used in their as-printed state. Given that no considerable difference in the measured tensile properties of 1 mm thick samples and 3 mm thick samples could be measured, it may be possible to apply more representative tensile results based on as-printed samples to the design of functional components.

8. Ultimately, the results of this research have been applied to the design and optimization of a number of aerospace components. This work has had a direct impact on the success of the Aurora rocket, which is slated to be the highest flight of a Canadian built liquid rocket in history and a significant milestone in Canadian aerospace.

6.1 Future work

While this work was successful in identifying and characterizing process parameters which enable high quality printing of AlSi10Mg as well as presenting a new methodology for the

design of compressive structural members manufactured using AM, a number of areas of further research have been identified, which may enable significant improvements upon what has been presented in this work.

6.1.1 Structural Optimization

While the methodology presented in Chapter 2 was capable of achieving significant performance increases using DfAM compared to conventionally manufactured structural members, it is still a relatively manual design process. The designer is required to not only create the outer geometry, but also to iterate upon the mapping between initial stress and shell thickness. As such, there is a need for better automation of this type of workflow, with the ideal being commercially available topology optimization software capable of direct optimization against buckling.

The test fixture presented in this work was an effective tool for experimentally comparing the fixed-end free-end buckling resistance of different designs and for estimating the strength of each. However, there are still a number of refinements that could be made to the fixture. In particular, resolving the tendency of the fixture to occasionally bind and improving the alignment process would aid to achieve more consistent results. Further characterization work to confirm the accuracy of the fixture is also needed if it is to be used for measuring true part strength instead of comparative analysis of performance.

6.1.2 Downskin Surface Roughness and Print Angle Optimization

While the work presented in Chapter 3 was successful in presenting a new approach to predicting downskin surface roughness and identifying a set of process parameters which allow for high quality low angle printing, there are a number of areas that would benefit from additional investigation in the future:

Gradual Process Parameter Transitions for Improved Density and Roughness

Current LPBF build software is relatively limited in the available control of process parameters across a part volume or surface region. This work found that at least three different sets of downskin process parameters gave the best roughness result depending on the angle and, with further refinement, it is likely that a gradient of optimal process parameters could be identified to ensure optimal results across all angles. As such, the ability to define more than a single set of downskin process parameters or the ability to parametrize process parameters as a function of geometry in the build software would be of high value. Similarly, it was found that for a specific downskin angle, no single core power is optimal for both reducing downskin roughness as well as ensuring a high density core. To achieve optimal results, it is likely that a smooth transition from downskin process parameters to core parameters would be needed. Emerging software tools such as Netfabb and Dyndrite can be explored, which may provide the necessary levels of granular control required to enable development of these gradually transitioning process parameters.

Refinement of High Power and Velocity Process Parameters

The optimal low-angle downskin process parameters identified in this work are at the limits of the available speed and power of the LPBF system used. To further refine the optimal process parameters for low angle printing, it is recommended that a design of experiment be carried out on a system capable of higher laser power and velocity.

Downskin Melt Pool Overlap Model

While the downskin melt pool overlap model was shown to be an effective tool, there are a number of refinements that can be made to the modeling approaches presented in this work. As previously discussed, limitations were found in the applicability of MDR for identifying process parameters which result in optimal sideskin / high angle downskin roughness. While an MDR of 2 is still desirable to ensure stable high density printing, identifying a second predictor of roughness that compliments MDR and accounts for the powder adhesion observed at high downskin angles would be of significant value.

For the downskin melt pool overlap model, additional verification efforts should be conducted to confirm the model functions as intended. In particular, it would be valuable to use metallography to investigate the actual printed downskin melt pool geometry and compare the measured dimensions to those predicted by the model.

Currently, the melt pool prediction model has no consideration for the larger surrounding part geometry and only considers the area directly in contact with the melt pool. As was observed with the unexpected keyhole porosity found in the samples, it is expected that this contributes some amount of error to the model since it does not consider the cooling rate of the larger part around it. Adding some form of geometry compensation may allow for improved accuracy.

Finally, since the melt pool overlap model was computed manually, it was difficult to re-compute for different assumed melt pool geometries and hatch spacings. If the model can be better generalized or automated, it may allow for more accurate predictions by enabling estimation of effective material properties specific to the process parameters of interest.

Low Angle Printing

While the work presented in Chapter 3 has been successful in demonstrating good roughness at print angles as low as 20°, there is significant further investigation that should be explored. This work selected 20° as the lowest angle investigated as a reasonable compromise between improving on current capabilities, and minimizing risk of print failure. Similarly, all samples were aligned away from the recoater to reduce risk; this is often not possible for functional components. Given the success of certain process parameters in this work, it is recommended that further research be done into the limits of minimum print angle and recoater orientation using optimized process parameters. Given that even poor process parameters used in this work still successfully printed as low as 20°, it is expected that significant improvement may be possible.

Additional Areas of Investigation

It has been qualitatively observed that the concavity of overhanging structures can have a significant effect on their ability to print successfully. Considerable warping and poor surface roughness has been observed on parts with 45° downskin on convex curves, while printing at low angles has been achieved with much less warping than expected on structures with concave curvature. An example of this is the turbine housing presented in

Section 5.1.1, which experienced warping and degraded surface finish on the convex outer flange, but had good surface finish on the steeper concave overhangs. No literature was readily available on this phenomenon and it may be worthy of investigation. Investigation of downskin process parameter optimization using finer PSDs may also be of value based on the promising results presented in Section 5.4.

Finally, there have been a number of industrially-relevant designs which would significantly benefit from the low angle printing identified for AlSi10Mg, but require a different material class such as Inconel or stainless steel. Application of the methodologies presented in this work for the development of process parameters to enable low angle printing for these materials would be of significant value.

6.1.3 Tensile Property Charaterization

In Chapter 4, the use of CT scanning to determine the true cross-section of samples was critical for successfully compensating for the effects of surface roughness on measurement error; however, the uneconomical nature of scanning every sample presented challenges in this work. This technology is also not readily accessible for many research labs. Further investigation into alternative methods of accurately measuring the cross-section of as-printed samples would be of significant value. One promising option is the use of high-resolution optical scanning. This was originally attempted for this work, but the available equipment struggled to accurately detect small features and, therefore, to correctly stitch together images into a complete model. With further work and refinement, it is likely that optical scanning could be used instead of CT, enabling economical but accurate measurement of each sample.

One of the well known issues associated with the high surface roughness found in

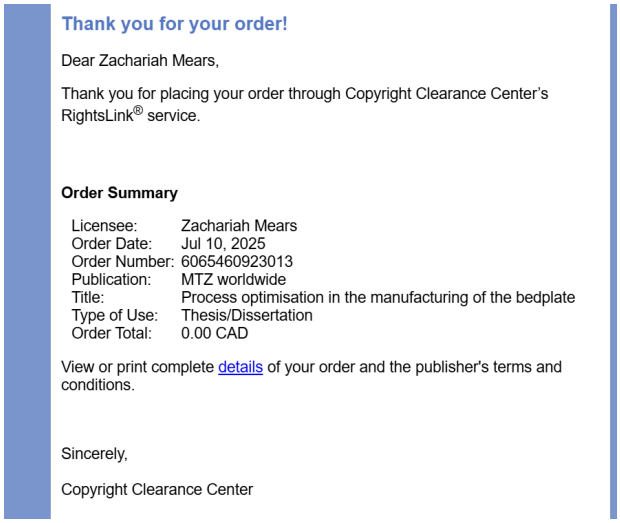
LPBF parts is that it typically leads to a significant reduction in fatigue life for printed components. Conducting low cycle fatigue life testing on samples printed with the low surface roughness process parameters tested in this work would be of significant value, particularly if investigations into the effect of steep overhang angles are conducted.

The lack of difference in tensile properties between thinner and thicker samples within the range being studied indicates that this data may be applicable across a wide range of wall thicknesses. This is a considerable boon for simplifying the design process of AM parts which experience high loads with as-printed surface finishes. However, only two wall thicknesses were tested in this work. It is recommended that the effect on tensile properties of samples thinner than 1 mm and greater than 3 mm be investigated to evaluate if these uniform material properties hold across a wider range of wall thicknesses.

Finally, it was found that the tensile properties of thin samples printed at steep overhang angles are very degraded, likely owing to the presence of porosity, poor surface properties and geometric fidelity, and differences in microstructure properties. Finding a method to improve these properties while still printing at very low angles is of significant value for applications such as closed impellers and TPMS heat exchangers. The use of process parameters which smoothly transition between downskin and core strategies to reduce porosity and improve dimensional accuracy, as discussed in Section 3.3.5, may help mitigate this effect. Other approaches may include heat treatment of the part, either via post-processing or in-situ stress relief via a re-scanning strategy [111], [112].

Letters of Copyright Permission

Figure 2.3 is reproduced under licence from Springer Nature, see Figure 6.1 for a copy of the letter confirming the license order [34].



Thank you for your order!

Dear Zachariah Mears,

Thank you for placing your order through Copyright Clearance Center's RightsLink® service.

Order Summary

Licensee:	Zachariah Mears
Order Date:	Jul 10, 2025
Order Number:	6065460923013
Publication:	MTZ worldwide
Title:	Process optimisation in the manufacturing of the bedplate
Type of Use:	Thesis/Dissertation
Order Total:	0.00 CAD

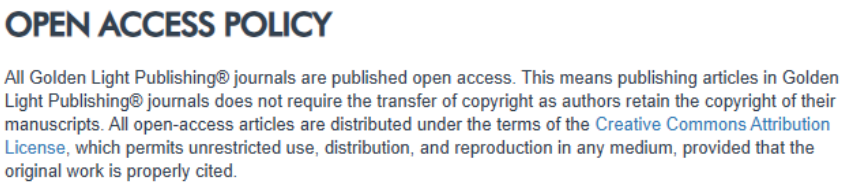
View or print complete details of your order and the publisher's terms and conditions.

Sincerely,

Copyright Clearance Center

Figure 6.1: Letter confirming right to reproduce Figure 6.1.

Figure 2.2 is adapted from [30]. The publisher, Golden Light Publishing, has an open access policy and allows unrestricted use, as shown in Figure 6.2 [113].



OPEN ACCESS POLICY

All Golden Light Publishing® journals are published open access. This means publishing articles in Golden Light Publishing® journals does not require the transfer of copyright as authors retain the copyright of their manuscripts. All open-access articles are distributed under the terms of the Creative Commons Attribution License, which permits unrestricted use, distribution, and reproduction in any medium, provided that the original work is properly cited.

Figure 6.2: Golden Light Publishing open access policy [113].

References

[1] B. Blakey-Milner, P. Gradl, G. Snedden, *et al.*, "Metal additive manufacturing in aerospace: A review," *Materials & Design*, vol. 209, p. 110 008, Nov. 2021, ISSN: 0264-1275. DOI: 10.1016/j.matdes.2021.110008. [Online]. Available: https://www.sciencedirect.com/science/article/pii/S0264127521005633 (visited on 07/09/2025).

[2] G. P. Sutton and O. Biblarz, *Rocket propulsion elements*, eng, Ninth edition. Hoboken, New Jersey: John Wiley & Sons Inc, 2017.

[3] M. Armstrong, H. Mehrabi, and N. Naveed, "An overview of modern metal additive manufacturing technology," *Journal of Manufacturing Processes*, vol. 84, pp. 1001–1029, Dec. 2022, ISSN: 1526-6125. DOI: 10.1016/j.jmapro.2022.10.060. [Online]. Available: https://www.sciencedirect.com/science/article/pii/S1526612522007459 (visited on 07/10/2025).

[4] M. Tebianian, S. Aghaie, N. S. Razavi Jafari, *et al.*, "A Review of the Metal Additive Manufacturing Processes," *Materials*, vol. 16, no. 24, p. 7514, Dec. 2023, ISSN: 1996-1944. DOI: 10.3390/ma16247514. [Online]. Available: https://www.ncbi.nlm.nih.gov/pmc/articles/PMC10744938/ (visited on 07/10/2025).

[5] D. Thomas and S. W. Gilbert, *Costs and Cost Effectiveness of Additive Manufacturing*, en, Last Modified: 2021-06-24T00:06-04:00 Publisher: Douglas Thomas, Stanley W. Gilbert, Dec. 2014. [Online]. Available: https://www.nist.gov/publications/costs-and-cost-effectiveness-additive-manufacturing (visited on 07/10/2025).

[6] N. Khan and A. Riccio, "A systematic review of design for additive manufacturing of aerospace lattice structures: Current trends and future directions," *Progress in Aerospace Sciences*, vol. 149, p. 101 021, Aug. 2024, ISSN: 0376-0421. DOI: 10.1016/j.paerosci.2024.101021. [Online]. Available: https://www.sciencedirect.com/science/article/pii/S0376042124000472 (visited on 07/09/2025).

[7] J. Zhu, H. Zhou, C. Wang, L. Zhou, S. Yuan, and W. Zhang, "A review of topology optimization for additive manufacturing: Status and challenges," *Chinese Journal of Aeronautics*, vol. 34, no. 1, pp. 91–110, Jan. 2021, ISSN: 1000-9361. DOI: 10.1016/j.cja.2020.09.020. [Online]. Available: https://www.sciencedirect.com/science/article/pii/S1000936120304520 (visited on 07/09/2025).

[8] M. Srivastava and S. Rathee, "Additive manufacturing: Recent trends, applications and future outlooks," en, *Progress in Additive Manufacturing*, vol. 7, no. 2, pp. 261–287, Apr. 2022, ISSN: 2363-9520. DOI: 10.1007/s40964-021-00229-8. [Online]. Available: https://doi.org/10.1007/s40964-021-00229-8 (visited on 07/09/2025).

[9] *Standard Terminology for Additive Manufacturing – General Principles – Terminology*, 2015. [Online]. Available: https://compass.astm.org/document/?contentCode=ASTM%7CF3177-15%7Cen-US&proxycl=https%3A%2F%2Fsecure.astm.org&fromLogin=true (visited on 07/10/2025).

[10] A. Vafadar, F. Guzzomi, A. Rassau, and K. Hayward, "Advances in Metal Additive Manufacturing: A Review of Common Processes, Industrial Applications, and Current Challenges," en, *Applied Sciences*, vol. 11, no. 3, p. 1213, Jan. 2021, Number: 3 Publisher: Multidisciplinary Digital Publishing Institute, ISSN: 2076-3417. DOI: 10.3390/app11031213. [Online]. Available: https://www.mdpi.com/2076-3417/11/3/1213 (visited on 07/10/2025).

[11] S. Chowdhury, N. Yadaiah, C. Prakash, *et al.*, "Laser powder bed fusion: A state-of-the-art review of the technology, materials, properties & defects, and numerical modelling," *Journal of Materials Research and Technology*, vol. 20, pp. 2109–2172, Sep. 2022, ISSN: 2238-7854. DOI: 10.1016/j.jmrt.2022.07.121. [Online]. Available: https://www.sciencedirect.com/science/article/pii/S2238785422011607 (visited on 07/10/2025).

[12] Som Dixit and Shunyu Liu, "Laser Additive Manufacturing of High-Strength Aluminum Alloys: Challenges and Strategies," en, *ResearchGate*, Oct. 2024. DOI: 10.3390/jmmp6060156. [Online]. Available: https://www.researchgate.net/publication/366123456_Laser_Additive_Manufacturing_of_High-Strength_Aluminum_Alloys_Challenges_and_Strategies (visited on 01/03/2025).

[13] P. Renner, S. Jha, Y. Chen, A. Raut, S. G. Mehta, and H. Liang, "A Review on Corrosion and Wear of Additively Manufactured Alloys," *Journal of Tribology*, vol. 143, no. 050802, Apr. 2021, ISSN: 0742-4787. DOI: 10.1115/1.4050503. [Online]. Available: https://doi.org/10.1115/1.4050503 (visited on 07/10/2025).

[14] N. D. Dejene and H. G. Lemu, "Current Status and Challenges of Powder Bed Fusion-Based Metal Additive Manufacturing: Literature Review," en, *Metals*, vol. 13, no. 2, p. 424, Feb. 2023, Number: 2 Publisher: Multidisciplinary Digital Publish-

ing Institute, ISSN: 2075-4701. DOI: 10.3390/met13020424. [Online]. Available: https://www.mdpi.com/2075-4701/13/2/424 (visited on 07/10/2025).

[15] L. Brock, "Laser Powder Bed Fusion of AlSi10Mg for Fabrication of Fluid Power Components," en, MASc. dissertation, University of Waterloo, 2019.

[16] J. Patel, M. Vlasea, and S. Patel, "Towards generalizable machine learning prediction of downskin surface roughness in laser powder bed fusion," *Advances in Industrial and Manufacturing Engineering*, vol. 10, p. 100 163, May 2025, ISSN: 2666-9129. DOI: 10.1016/j.aime.2025.100163. [Online]. Available: https://www.sciencedirect.com/science/article/pii/S2666912925000078 (visited on 07/10/2025).

[17] S. Patel, "Melting modes in laser powder bed fusion additive manufacturing," en, Ph.D. dissertation, University of Waterloo, 2021.

[18] J. Schmelzle, E. V. Kline, C. J. Dickman, E. W. Reutzel, G. Jones, and T. W. Simpson, "(Re)Designing for Part Consolidation: Understanding the Challenges of Metal Additive Manufacturing," *Journal of Mechanical Design*, vol. 137, no. 11, Oct. 2015, ISSN: 1050-0472. DOI: 10.1115/1.4031156. [Online]. Available: https://doi.org/10.1115/1.4031156 (visited on 12/08/2022).

[19] Rick Kennedy, *Outside the Box: How GE Aviation Entered the Brave New World of Additive Manufacturing — GE Aerospace News*, en, 2019. [Online]. Available: https://www.geaerospace.com/news/articles/100-year-anniversary-manufacturing-technology/outside-box-how-ge-aviation-entered-brave (visited on 07/09/2025).

[20] O. Diegel, J. Schutte, A. Ferreira, and Y. L. Chan, "Design for additive manufacturing process for a lightweight hydraulic manifold," *Additive Manufacturing*, vol. 36,

p. 101 446, Dec. 2020, ISSN: 2214-8604. DOI: 10.1016/j.addma.2020.101446. [Online]. Available: https://www.sciencedirect.com/science/article/pii/S2214860420308186 (visited on 07/04/2025).

[21] M. Tomlin and J. Meyer, "Topology Optimization of an Additive Layer Manufactured (ALM) Aerospace Part," en, *The 7th Altair CAE Technology Conference 2011*, 2011.

[22] D. Jia, F. Li, and Y. Zhang, "3D-printing process design of lattice compressor impeller based on residual stress and deformation," en, *Scientific Reports*, vol. 10, no. 1, p. 600, Jan. 2020, Publisher: Nature Publishing Group, ISSN: 2045-2322. DOI: 10.1038/s41598-019-57131-1. [Online]. Available: https://www.nature.com/articles/s41598-019-57131-1 (visited on 07/14/2025).

[23] M. Buchholz, S. Gruber, A. Selbmann, *et al.*, "Flow rate improvements in additively manufactured flow channels suitable for rocket engine application," en, *CEAS Space Journal*, vol. 15, no. 5, pp. 715–728, Sep. 2023, ISSN: 1868-2510. DOI: 10.1007/s12567-022-00476-7. [Online]. Available: https://doi.org/10.1007/s12567-022-00476-7 (visited on 07/10/2025).

[24] G. Yamomo, N. Hossain, S. Towfighian, and R. Willing, "Design and analysis of a compliant 3D printed energy harvester housing for knee implants," *Medical Engineering & Physics*, vol. 88, pp. 59–68, Feb. 2021, ISSN: 1350-4533. DOI: 10.1016/j.medengphy.2020.12.008. [Online]. Available: https://www.sciencedirect.com/science/article/pii/S1350453320301880 (visited on 07/10/2025).

[25] Igor Yadroitsev, Ina Yadroitsava, Anton Du Plessis, and Eric MacDonald, *Fundamentals of Laser Powder Bed Fusion of Metals*, en-US. Elsevier, May 2021, ISBN: 978-0-12-824090-8. [Online]. Available: https://shop.elsevier.com/books/

fundamentals-of-laser-powder-bed-fusion-of-metals/yadroitsev/978-0-12-824090-8 (visited on 07/09/2025).

[26] Sagar Patel, Haoxiu Chen, Mihaela Vlasea, and Yu Zou, "The influence of beam focus during laser powder bed fusion of a high reflectivity aluminium alloy — AlSi10Mg," en, *Additive Manufacturing*, vol. 59, p. 103 112, Nov. 2022, Publisher: Elsevier, ISSN: 2214-8604. DOI: 10.1016/j.addma.2022.103112. [Online]. Available: https://www.sciencedirect.com/science/article/pii/S2214860422005012 (visited on 07/17/2023).

[27] K. Zhou, D. Cui, Z. Chai, *et al.*, "In-situ tailoring microstructures to promote strength-ductility synergy in laser powder bed fusion of NiCoCr medium-entropy alloy," *Additive Manufacturing*, vol. 66, p. 103 443, Mar. 2023, ISSN: 2214-8604. DOI: 10.1016/j.addma.2023.103443. [Online]. Available: https://www.sciencedirect.com/science/article/pii/S2214860423000568 (visited on 06/25/2025).

[28] N. Zolfaghari, "Design of Structural Members for a High-Powered Hybrid Sounding Rocket," en, University of Waterloo, Tech. Rep., May 2023.

[29] Richard G. Budynas and J. Keith Nisbett, *Shigley's Mechanical Engineering Design*, 11th Edition in SI Units. New York, NY: McGraw-Hill Education, 2021, ISBN: 978-981-315-898-6.

[30] M. Saracoglu and S. Uzun, "Stability analysis of columns with variable cross-sections," *Journal of Structural Engineering & Applied Mechanics*, vol. 3, pp. 169–179, Sep. 2020. DOI: 10.31462/jseam.2020.03169179.

[31] L. Brock, I. Ogunsanya, H. Asgari, S. Patel, and M. Vlasea, "Relative Performance of Additively Manufactured and Cast Aluminum Alloys," en, *Journal of Materials Engineering and Performance*, vol. 30, no. 1, pp. 760–782, Jan. 2021, ISSN: 1544-

1024. DOI: 10.1007/s11665-020-05403-7. [Online]. Available: https://doi.org/10.1007/s11665-020-05403-7 (visited on 01/06/2025).

[32] G. A. O. Adam and D. Zimmer, "On design for additive manufacturing: Evaluating geometrical limitations," *Rapid Prototyping Journal*, vol. 21, no. 6, pp. 662–670, Jan. 2015, Publisher: Emerald Group Publishing Limited, ISSN: 1355-2546. DOI: 10.1108/RPJ-06-2013-0060. [Online]. Available: https://doi.org/10.1108/RPJ-06-2013-0060 (visited on 12/01/2022).

[33] J. Kranz, "Design guidelines for laser additive manufacturing of lightweight structures in TiAl6V4," *Journal of Laser Applications*, vol. 27, Dec. 2014. DOI: 10.2351/1.4885235.

[34] N. Gerth, H. Sauer, M. Gebauer, and T. Rädel, "Process optimisation in the manufacturing of the bedplate," en, *MTZ worldwide*, vol. 74, no. 6, pp. 42–46, Jun. 2013, ISSN: 2192-9114. DOI: 10.1007/s38313-013-0063-y. [Online]. Available: https://doi.org/10.1007/s38313-013-0063-y (visited on 07/10/2025).

[35] Z. Zhu, Z. Hu, H. L. Seet, *et al.*, "Recent progress on the additive manufacturing of aluminum alloys and aluminum matrix composites: Microstructure, properties, and applications," *International Journal of Machine Tools and Manufacture*, vol. 190, p. 104 047, Aug. 2023, ISSN: 0890-6955. DOI: 10.1016/j.ijmachtools.2023.104047. [Online]. Available: https://www.sciencedirect.com/science/article/pii/S089069552300055X (visited on 01/06/2025).

[36] L. Hitzler, S. Hafenstein, F. Mendez Martin, *et al.*, "Heat Treatments and Critical Quenching Rates in Additively Manufactured Al–Si–Mg Alloys," en, *Materials*, vol. 13, no. 3, p. 720, Jan. 2020, Number: 3 Publisher: Multidisciplinary Digital Pub-

lishing Institute, ISSN: 1996-1944. DOI: 10.3390/ma13030720. [Online]. Available: https://www.mdpi.com/1996-1944/13/3/720 (visited on 06/25/2025).

[37] D. S. MacKenzie, "Heat Treating Aluminum for Aerospace Applications," en, *Houghton International*, 2003.

[38] N. Keleshian, R. Kyser, J. Rodriguez, *et al.*, "On the Distortion and Warpage of 7249 Aluminum Alloy After Quenching and Machining," en, *Journal of Materials Engineering and Performance*, vol. 20, no. 7, pp. 1230–1234, Oct. 2011, ISSN: 1544-1024. DOI: 10.1007/s11665-010-9756-4. [Online]. Available: https://doi.org/10.1007/s11665-010-9756-4 (visited on 06/25/2025).

[39] P. Li, Y. Kim, A. C. Bobel, *et al.*, "Microstructural origin of the anisotropic flow stress of laser powder bed fused AlSi10Mg," *Acta Materialia*, vol. 220, p. 117 346, Nov. 2021, ISSN: 1359-6454. DOI: 10.1016/j.actamat.2021.117346. [Online]. Available: https://www.sciencedirect.com/science/article/pii/S1359645421007254 (visited on 06/25/2025).

[40] EOS, *EOS Aluminium AlSi10Mg*, 2014. [Online]. Available: https://fathommfg.com/wp-content/uploads/2020/11/EOS_Aluminium_AlSi10Mg_en.pdf (visited on 12/18/2022).

[41] *EOS Aluminium AlSi10Mg Material Data Sheet*, 2022. [Online]. Available: https://www.eos.info/03_system-related-assets/material-related-contents/metal-materials-and-examples/metal-material-datasheet/aluminium/material_datasheet_eos_aluminium-alsi10mg_en_web.pdf (visited on 11/17/2022).

[42] Joseph R. Davis, Ed., *Metals Handbook Desk Edition*, en, 2nd Edition. ASM International, Dec. 1998, ISBN: 978-1-62708-199-3. [Online]. Available: https://

dl.asminternational.org/handbooks/edited-volume/49/chapter/603286/Properties-of-Wrought-Aluminum-Alloys (visited on 12/02/2024).

[43] Open Additive, *Metal Laser Powder Bed Fusion design guidelines*, 2019. [Online]. Available: https://openadditive.com/wp-content/uploads/2020/05/OA_LPBF_Design_Guide.pdf (visited on 11/27/2022).

[44] D. Thomas, "The development of design rules for selective laser melting," en, thesis, Cardiff Metropolitan University, Oct. 2009. DOI: 10.25401/cardiffmet.20974597.v1. [Online]. Available: https://figshare.cardiffmet.ac.uk/articles/thesis/The_development_of_design_rules_for_selective_laser_melting/20974597/1 (visited on 07/14/2025).

[45] P. Mercelis and J.-P. Kruth, "Residual stresses in selective laser sintering and selective laser melting," *Rapid Prototyping Journal*, vol. 12, no. 5, pp. 254–265, Jan. 2006, Publisher: Emerald Group Publishing Limited, ISSN: 1355-2546. DOI: 10.1108/13552540610707013. [Online]. Available: https://doi.org/10.1108/13552540610707013 (visited on 07/14/2025).

[46] T. Xu, X. Huang, X. Lin, and Y. M. Xie, "Topology optimization for maximizing buckling strength using a linear material model," *Computer Methods in Applied Mechanics and Engineering*, vol. 417, p. 116 437, Dec. 2023, ISSN: 0045-7825. DOI: 10.1016/j.cma.2023.116437. [Online]. Available: https://www.sciencedirect.com/science/article/pii/S0045782523005613 (visited on 11/08/2024).

[47] Z. Mears, "Part Consolidation and Optimization of a Rocket Engine Feed System," en, University of Waterloo, Tech. Rep., Dec. 2022, p. 41.

[48] A. Khajehdezfuly, D. Poorveis, and S. Nazarinia, "Comparison between linear and nonlinear buckling loads of FGM cylindrical panel with cutout," *International Jour-*

nal of Non-Linear Mechanics, vol. 150, p. 104 361, Apr. 2023, ISSN: 0020-7462. DOI: 10.1016/j.ijnonlinmec.2023.104361. [Online]. Available: https://www.sciencedirect.com/science/article/pii/S0020746223000136 (visited on 07/14/2025).

[49] S. Deshpande, "Buckling And Post Buckling Of Structural Components," *Mechanical and Aerospace Engineering Theses*, Jan. 2010. [Online]. Available: https://mavmatrix.uta.edu/mechaerospace_theses/221.

[50] G. Sander, A. P. Babu, X. Gao, D. Jiang, and N. Birbilis, "On the effect of build orientation and residual stress on the corrosion of 316L stainless steel prepared by selective laser melting," *Corrosion Science*, vol. 179, p. 109 149, Feb. 2021, ISSN: 0010-938X. DOI: 10.1016/j.corsci.2020.109149. [Online]. Available: https://www.sciencedirect.com/science/article/pii/S0010938X20324306 (visited on 07/14/2025).

[51] A. Hussein, L. Hao, C. Yan, R. Everson, and P. Young, "Advanced lattice support structures for metal additive manufacturing," *Journal of Materials Processing Technology*, vol. 213, pp. 1019–1026, Jul. 2013. DOI: 10.1016/j.jmatprotec.2013.01.020.

[52] C. C. Wu and J. S. Arora, "Design sensitivity analysis of non-linear buckling load," en, *Computational Mechanics*, vol. 3, no. 2, pp. 129–140, Mar. 1988, ISSN: 1432-0924. DOI: 10.1007/BF00317060. [Online]. Available: https://doi.org/10.1007/BF00317060 (visited on 01/07/2025).

[53] W. H. Horton and D. Struble, "End Fixity of Columns," en, Stanford University, USAAVLABS Technical Report 70-10, Aug. 1970.

[54] *Standard Test Methods of Compression Testing of Metallic Materials at Room Temperature*, 2019. [Online]. Available: https://compass.astm.org/document/?contentCode=ASTM%7CE0009-19%7Cen-US (visited on 01/12/2024).

[55] A. H. Alami, A. Ghani Olabi, A. Alashkar, *et al.*, "Additive manufacturing in the aerospace and automotive industries: Recent trends and role in achieving sustainable development goals," *Ain Shams Engineering Journal*, vol. 14, no. 11, p. 102 516, Nov. 2023, ISSN: 2090-4479. DOI: 10.1016/j.asej.2023.102516. [Online]. Available: https://www.sciencedirect.com/science/article/pii/S2090447923004057 (visited on 07/10/2025).

[56] O. Hitchens, *3D-printed rocket engines: The technology driving the private sector space race*, en, 2021. [Online]. Available: http://theconversation.com/3d-printed-rocket-engines-the-technology-driving-the-private-sector-space-race-168146 (visited on 12/17/2022).

[57] E. O. Ezugwu and Z. M. Wang, "Titanium alloys and their machinability—a review," *Journal of Materials Processing Technology*, Superplasticity and Superplastic Technology in Japan, vol. 68, no. 3, pp. 262–274, Aug. 1997, ISSN: 0924-0136. DOI: 10.1016/S0924-0136(96)00030-1. [Online]. Available: https://www.sciencedirect.com/science/article/pii/S0924013696000301 (visited on 07/12/2025).

[58] S. Roy, R. Kumar, Anurag, A. Panda, and R. K. Das, "A Brief Review on Machining of Inconel 718," *Materials Today: Proceedings*, Materials Processing and characterization, 16th – 18th March 2018, vol. 5, no. 9, Part 3, pp. 18 664–18 673, Jan. 2018, ISSN: 2214-7853. DOI: 10.1016/j.matpr.2018.06.212. [Online]. Available:

https://www.sciencedirect.com/science/article/pii/S221478531831335X (visited on 07/12/2025).

[59] M. McMahon, *Aluminium Additive Manufacturing: How a new generation of alloys will fuel industry growth*, en-GB, Dec. 2024. [Online]. Available: https://www.metal-am.com/articles/aluminium-additive-manufacturing-how-a-new-generation-of-alloys-will-fuel-industry-growth/ (visited on 07/12/2025).

[60] D. Y. Pimenov, M. Kiran, N. Khanna, *et al.*, "Review of improvement of machinability and surface integrity in machining on aluminum alloys," en, *The International Journal of Advanced Manufacturing Technology*, vol. 129, no. 11, pp. 4743–4779, Dec. 2023, ISSN: 1433-3015. DOI: 10.1007/s00170-023-12630-4. [Online]. Available: https://doi.org/10.1007/s00170-023-12630-4 (visited on 07/12/2025).

[61] A. Charles, A. Elkaseer, U. Paggi, L. Thijs, V. Hagenmeyer, and S. Scholz, "Down-facing surfaces in laser powder bed fusion of Ti6Al4V: Effect of dross formation on dimensional accuracy and surface texture," *Additive Manufacturing*, vol. 46, p. 102 148, Oct. 2021, ISSN: 2214-8604. DOI: 10.1016/j.addma.2021.102148. [Online]. Available: https://www.sciencedirect.com/science/article/pii/S2214860421003122 (visited on 07/12/2025).

[62] M. Bugatti and B. M. Colosimo, "Predicting the roughness of overhanging surfaces in laser powder bed fusion via in-situ thermal imaging," *Journal of Manufacturing Processes*, vol. 124, pp. 1340–1348, Aug. 2024, ISSN: 1526-6125. DOI: 10.1016/j.jmapro.2024.06.050. [Online]. Available: https://www.sciencedirect.com/science/article/pii/S1526612524006303 (visited on 07/14/2025).

[63] S. Z. Uddin, L. E. Murr, C. A. Terrazas, P. Morton, D. A. Roberson, and R. B. Wicker, "Processing and characterization of crack-free aluminum 6061 using high-

temperature heating in laser powder bed fusion additive manufacturing," *Additive Manufacturing*, vol. 22, pp. 405–415, Aug. 2018, ISSN: 2214-8604. DOI: 10.1016/j.addma.2018.05.047. [Online]. Available: https://www.sciencedirect.com/science/article/pii/S2214860418302975 (visited on 06/25/2025).

[64] J. H. Martin, B. D. Yahata, J. M. Hundley, J. A. Mayer, T. A. Schaedler, and T. M. Pollock, "3D printing of high-strength aluminium alloys," en, *Nature*, vol. 549, no. 7672, pp. 365–369, Sep. 2017, Publisher: Nature Publishing Group, ISSN: 1476-4687. DOI: 10.1038/nature23894. [Online]. Available: https://www.nature.com/articles/nature23894 (visited on 06/25/2025).

[65] P. A. Rometsch, Y. Zhu, X. Wu, and A. Huang, "Review of high-strength aluminium alloys for additive manufacturing by laser powder bed fusion," *Materials & Design*, vol. 219, p. 110 779, Jul. 2022, ISSN: 0264-1275. DOI: 10.1016/j.matdes.2022.110779. [Online]. Available: https://www.sciencedirect.com/science/article/pii/S0264127522004014 (visited on 07/14/2025).

[66] A. M. Rubenchik, W. E. King, and S. S. Wu, "Scaling laws for the additive manufacturing," *Journal of Materials Processing Technology*, vol. 257, pp. 234–243, Jul. 2018, ISSN: 0924-0136. DOI: 10.1016/j.jmatprotec.2018.02.034. [Online]. Available: https://www.sciencedirect.com/science/article/pii/S0924013618300906 (visited on 06/04/2025).

[67] A. K. Agrawal, B. Rankouhi, and D. J. Thoma, "Predictive process mapping for laser powder bed fusion: A review of existing analytical solutions," *Current Opinion in Solid State and Materials Science*, vol. 26, no. 6, p. 101 024, Dec. 2022, ISSN: 1359-0286. DOI: 10.1016/j.cossms.2022.101024. [Online]. Available: https:

//www.sciencedirect.com/science/article/pii/S1359028622000444 (visited on 07/09/2025).

[68] M. A. L. Phan, O. Dew, and I. Todd, "Predictive process diagram for parameters selection in laser powder bed fusion to achieve high-density and low-cracking built parts," *Additive Manufacturing*, vol. 85, p. 104 145, Apr. 2024, ISSN: 2214-8604. DOI: 10.1016/j.addma.2024.104145. [Online]. Available: https://www.sciencedirect.com/science/article/pii/S221486042400191X (visited on 06/17/2025).

[69] Z. Gan, O. L. Kafka, N. Parab, *et al.*, "Universal scaling laws of keyhole stability and porosity in 3D printing of metals," en, *Nature Communications*, vol. 12, no. 1, pp. 1–8, Apr. 2021, Number: 1 Publisher: Nature Publishing Group, ISSN: 2041-1723. DOI: 10.1038/s41467-021-22704-0. [Online]. Available: https://www.nature.com/articles/s41467-021-22704-0 (visited on 05/28/2025).

[70] S. Patel and M. Vlasea, "Melting modes in laser powder bed fusion," *Materialia*, vol. 9, p. 100 591, Mar. 2020, ISSN: 2589-1529. DOI: 10.1016/j.mtla.2020.100591. [Online]. Available: https://www.sciencedirect.com/science/article/pii/S2589152920300089 (visited on 10/13/2023).

[71] Allan David Rogalsky, Sagar Patel, Mihaela Vlasea, and Amin Molavi-Kakhki, "Improving Surface Quality and Geometric Fidelity of Water Atomized Pure Iron in Laser Powder Bed Fusion," in *AMPM 2022 Conference Proceedings*, 2022, pp. 356–374.

[72] T. Mukherjee and T. DebRoy, "Mitigation of lack of fusion defects in powder bed fusion additive manufacturing," *Journal of Manufacturing Processes*, vol. 36, pp. 442–449, Dec. 2018, ISSN: 1526-6125. DOI: 10.1016/j.jmapro.2018.10.028. [On-

line]. Available: https://www.sciencedirect.com/science/article/pii/S1526612518302603 (visited on 06/04/2025).

[73] M. Tang, P. C. Pistorius, and J. L. Beuth, "Prediction of lack-of-fusion porosity for powder bed fusion," *Additive Manufacturing*, vol. 14, pp. 39–48, Mar. 2017, ISSN: 2214-8604. DOI: 10.1016/j.addma.2016.12.001. [Online]. Available: https://www.sciencedirect.com/science/article/pii/S2214860416300471 (visited on 06/04/2025).

[74] K. Darvish, Z. W. Chen, and T. Pasang, "Reducing lack of fusion during selective laser melting of CoCrMo alloy: Effect of laser power on geometrical features of tracks," *Materials & Design*, vol. 112, pp. 357–366, Dec. 2016, ISSN: 0264-1275. DOI: 10.1016/j.matdes.2016.09.086. [Online]. Available: https://www.sciencedirect.com/science/article/pii/S0264127516312679 (visited on 06/04/2025).

[75] Allan Rogalsky, Issa Rishmawi, Brian Jeong, Ehsan Toyserkani, and Mihaela Vlasea, *Modulated Laser Scaling Models for SLM Process Mapping: A comparison using Iron, Invar 36 and 316 SS*, 2018.

[76] Y. Zhao, H. Zhang, J. Cai, S. Ji, and D. Li, "A Prediction Model of Effective Thermal Conductivity for Metal Powder Bed in Additive Manufacturing," *Chinese Journal of Mechanical Engineering*, vol. 36, no. 1, p. 41, Mar. 2023, ISSN: 2192-8258. DOI: 10.1186/s10033-023-00840-6. [Online]. Available: https://doi.org/10.1186/s10033-023-00840-6 (visited on 06/03/2025).

[77] L. C. Wei, L. E. Ehrlich, M. J. Powell-Palm, C. Montgomery, J. Beuth, and J. A. Malen, "Thermal conductivity of metal powders for powder bed additive manufacturing," *Additive Manufacturing*, vol. 21, pp. 201–208, May 2018, ISSN: 2214-8604. DOI: 10.1016/j.addma.2018.02.002. [Online]. Available: https://

www.sciencedirect.com/science/article/pii/S2214860417306231 (visited on 06/03/2025).

[78] R. R. J. Sélo, S. Catchpole-Smith, I. Maskery, I. Ashcroft, and C. Tuck, "On the thermal conductivity of AlSi10Mg and lattice structures made by laser powder bed fusion," *Additive Manufacturing*, vol. 34, p. 101 214, Aug. 2020, ISSN: 2214-8604. DOI: 10.1016/j.addma.2020.101214. [Online]. Available: https://www.sciencedirect.com/science/article/pii/S2214860420305868 (visited on 06/03/2025).

[79] N. T. Aboulkhair, M. Simonelli, L. Parry, I. Ashcroft, C. Tuck, and R. Hague, "3D printing of Aluminium alloys: Additive Manufacturing of Aluminium alloys using selective laser melting," *Progress in Materials Science*, vol. 106, p. 100 578, Dec. 2019, ISSN: 0079-6425. DOI: 10.1016/j.pmatsci.2019.100578. [Online]. Available: https://www.sciencedirect.com/science/article/pii/S007964251930060X (visited on 06/05/2025).

[80] U. Scipioni Bertoli, A. J. Wolfer, M. J. Matthews, J.-P. R. Delplanque, and J. M. Schoenung, "On the limitations of Volumetric Energy Density as a design parameter for Selective Laser Melting," *Materials & Design*, vol. 113, pp. 331–340, Jan. 2017, ISSN: 0264-1275. DOI: 10.1016/j.matdes.2016.10.037. [Online]. Available: https://www.sciencedirect.com/science/article/pii/S0264127516313363 (visited on 06/05/2025).

[81] C. K. Sit, L. N. S. Chiu, Y. Tang, and A. Huang, "Towards supportless laser powder bed fusion: Fundamental understanding of the formation of 1st layer overhang through parameter optimisation and in-situ high-speed thermal imaging," *Virtual and Physical Prototyping*, vol. 18, no. 1, e2231906, Dec. 2023, Publisher: Taylor & Francis _eprint: https://doi.org/10.1080/17452759.2023.2231906, ISSN: 1745-2759.

DOI: 10.1080/17452759.2023.2231906. [Online]. Available: https://doi.org/10.1080/17452759.2023.2231906 (visited on 10/22/2023).

[82] D. Wang, Y. Yang, Z. Yi, and X. Su, "Research on the fabricating quality optimization of the overhanging surface in SLM process," en, *The International Journal of Advanced Manufacturing Technology*, vol. 65, no. 9, pp. 1471–1484, Apr. 2013, ISSN: 1433-3015. DOI: 10.1007/s00170-012-4271-4. [Online]. Available: https://doi.org/10.1007/s00170-012-4271-4 (visited on 10/27/2023).

[83] V. Viale, J. Stavridis, A. Salmi, F. Bondioli, and A. Saboori, "Optimisation of downskin parameters to produce metallic parts via laser powder bed fusion process: An overview," en, *The International Journal of Advanced Manufacturing Technology*, vol. 123, no. 7, pp. 2159–2182, Dec. 2022, ISSN: 1433-3015. DOI: 10.1007/s00170-022-10314-z. [Online]. Available: https://doi.org/10.1007/s00170-022-10314-z (visited on 07/20/2023).

[84] S. Patel, A. Rogalsky, and M. Vlasea, "Towards understanding side-skin surface characteristics in laser powder bed fusion," en, *Journal of Materials Research*, vol. 35, no. 15, pp. 2055–2064, Aug. 2020, Publisher: Cambridge University Press, ISSN: 0884-2914, 2044-5326. DOI: 10.1557/jmr.2020.125. [Online]. Available: https://www.cambridge.org/core/journals/journal-of-materials-research/article/towards-understanding-sideskin-surface-characteristics-in-laser-powder-bed-fusion/AE257097BCBD86540CE6B90A1343BEC9 (visited on 07/19/2023).

[85] M. Salarian, H. Asgari, and M. Vlasea, "Pore space characteristics and corresponding effect on tensile properties of Inconel 625 fabricated via laser powder bed fusion," *Materials Science and Engineering: A*, vol. 769, p. 138 525, Jan. 2020, ISSN:

0921-5093. DOI: 10.1016/j.msea.2019.138525. [Online]. Available: https://www.sciencedirect.com/science/article/pii/S0921509319313115 (visited on 06/17/2025).

[86] S. I. Shahabad, U. Ali, Z. Zhang, *et al.*, "On the effect of thin-wall thickness on melt pool dimensions in laser powder-bed fusion of Hastelloy X: Numerical modeling and experimental validation," *Journal of Manufacturing Processes*, vol. 75, pp. 435–449, Mar. 2022, ISSN: 1526-6125. DOI: 10.1016/j.jmapro.2022.01.029. [Online]. Available: https://www.sciencedirect.com/science/article/pii/S1526612522000469 (visited on 07/15/2025).

[87] N. Baldi, A. Giorgetti, M. Palladino, I. Giovannetti, G. Arcidiacono, and P. Citti, "Study on the Effect of Inter-Layer Cooling Time on Porosity and Melt Pool in Inconel 718 Components Processed by Laser Powder Bed Fusion," *Materials*, vol. 16, no. 11, p. 3920, May 2023, ISSN: 1996-1944. DOI: 10.3390/ma16113920. [Online]. Available: https://www.ncbi.nlm.nih.gov/pmc/articles/PMC10253632/ (visited on 07/15/2025).

[88] L. K. Dharmalingam, V. Aute, and J. Ling, *Review of Triply Periodic Minimal Surface (TPMS) based Heat Exchanger Designs*, en, 2022.

[89] K. Yeranee and Y. Rao, "A Review of Recent Investigations on Flow and Heat Transfer Enhancement in Cooling Channels Embedded with Triply Periodic Minimal Surfaces (TPMS)," en, *Energies*, vol. 15, no. 23, p. 8994, Jan. 2022, Number: 23 Publisher: Multidisciplinary Digital Publishing Institute, ISSN: 1996-1073. DOI: 10.3390/en15238994. [Online]. Available: https://www.mdpi.com/1996-1073/15/23/8994 (visited on 07/03/2025).

[90] J. Wang, K. Chen, M. Zeng, T. Ma, Q. Wang, and Z. Cheng, "Assessment of flow and heat transfer of triply periodic minimal surface based heat exchangers," *Energy*, vol. 282, p. 128 806, Nov. 2023, ISSN: 0360-5442. DOI: 10.1016/j.energy.2023.128806. [Online]. Available: https://www.sciencedirect.com/science/article/pii/S0360544223022004 (visited on 07/03/2025).

[91] I. El Khadiri, M. Abouelmajd, M. Zemzami, N. Hmina, M. Lagache, and S. Belhouideg, "Comprehensive analysis of flow and heat transfer performance in triply periodic minimal surface (TPMS) heat exchangers based on Fischer-Koch S, PMY, FRD, and Gyroid structures," *International Communications in Heat and Mass Transfer*, vol. 156, p. 107 617, Aug. 2024, ISSN: 0735-1933. DOI: 10.1016/j.icheatmasstransfer.2024.107617. [Online]. Available: https://www.sciencedirect.com/science/article/pii/S0735193324003798 (visited on 07/03/2025).

[92] Huber, M, Hartmann, M, Ess, J, Loeffel, Kraenzler, T, and Rettberg, R, "Process method for manufacturing impellers by Selective Laser Melting (SLM)," en, *Sulzer Technical Review*, 2018. [Online]. Available: https://www.researchgate.net/publication/326177989_Process_method_for_manufacturing_impellers_by_Selective_Laser_Melting_SLM (visited on 07/03/2025).

[93] A. Adiaconitei, I. S. Vintila, R. Mihalache, *et al.*, "Manufacturing of Closed Impeller for Mechanically Pump Fluid Loop Systems Using Selective Laser Melting Additive Manufacturing Technology," eng, *Materials (Basel, Switzerland)*, vol. 14, no. 20, p. 5908, Oct. 2021, ISSN: 1996-1944. DOI: 10.3390/ma14205908.

[94] A. Kumar, M. A. Shandiz, F. Sikan, and M. Brochu, "Microstructural and mechanical properties of an internal support-free IN625 closed impeller manufactured via laser powder bed fusion (L-PBF)," *Materials Science and Engineering: A*, vol. 874,

p. 145 080, May 2023, ISSN: 0921-5093. DOI: 10.1016/j.msea.2023.145080. [Online]. Available: https://www.sciencedirect.com/science/article/pii/S092150932300504X (visited on 07/03/2025).

[95] E. S. Zink, D. Bourdon, V. Neias Junior, D. F. Sias, W. Kitsche, and B. Wagner, "Study of Manufacturing Processes for Liquid Rocket Turbopump Impellers: Test and Analysis," en, *Journal of Aerospace Technology and Management*, vol. 12, e0920, Mar. 2020, Publisher: Departamento de Ciência e Tecnologia Aeroespacial, ISSN: 2175-9146. DOI: https://doi.org/10.5028/jatm.v12.1099. [Online]. Available: https://www.scielo.br/j/jatm/a/R4BsNHcjQSYgxbRLkMnkf9D/ (visited on 07/03/2025).

[96] N. Limbasiya, A. Jain, H. Soni, V. Wankhede, G. Krolczyk, and P. Sahlot, "A comprehensive review on the effect of process parameters and post-process treatments on microstructure and mechanical properties of selective laser melting of AlSi10Mg," *Journal of Materials Research and Technology*, vol. 21, pp. 1141–1176, Nov. 2022, ISSN: 2238-7854. DOI: 10.1016/j.jmrt.2022.09.092. [Online]. Available: https://www.sciencedirect.com/science/article/pii/S2238785422014995 (visited on 04/30/2024).

[97] L. Zhao, L. Song, J. G. Santos Macías, *et al.*, "Review on the correlation between microstructure and mechanical performance for laser powder bed fusion AlSi10Mg," *Additive Manufacturing*, vol. 56, p. 102 914, Aug. 2022, ISSN: 2214-8604. DOI: 10.1016/j.addma.2022.102914. [Online]. Available: https://www.sciencedirect.com/science/article/pii/S2214860422003116 (visited on 07/03/2025).

[98] *Renishaw AlSi10Mg RenAM 500 series Material Data Sheet*, 2024.

[99] *Nikon SLM AlSi10Mg Material Data Sheet*, 2024. [Online]. Available: https://www.slm-solutions.com/fileadmin/Content/Powder/MDS/nw/2024/MDS_AlSi10Mg_2024-04.1_EN.pdf (visited on 07/03/2025).

[100] *Standard Test Methods for Tension Testing of Metallic Materials*, May 2024. [Online]. Available: https://compass.astm.org/document/?contentCode=ASTM%7CE0008_E0008M-24%7Cen-US (visited on 09/04/2024).

[101] M. Frey, M. Shellabear, and L. Thorsson, *Mechanical Testing of DMLS Parts*, en, 2015.

[102] ASM Handbook Committee, *Properties of Wrought Aluminum and Aluminum Alloys*, en, Jan. 1990. DOI: 10.31399/asm.hb.v02.a0001060. [Online]. Available: https://dl.asminternational.org/handbooks/edited-volume/14/chapter/201862/Properties-of-Wrought-Aluminum-and-Aluminum-Alloys (visited on 07/03/2025).

[103] P. D. Kazarinoff, *7.5. Calculate Yield Strength Programmatically — Materials Science and Engineering Programming*, 2023. [Online]. Available: https://professorkazarinoff.github.io/Engineering-Materials-Programming/07-Mechanical-Properties/calculate-yield-strength-programmatically.html (visited on 06/27/2025).

[104] Takahiro Namazu, Junki Kuroishi, Hiroya Yamagiwa, *et al.*, "Young's Modulus Measurement of Submicron-thick Aluminum Films Using Fan-shaped Silicon Resonators — Request PDF," en, *Sensors and Materials*, vol. 31, pp. 713–727, 2018. DOI: 10.18494/SAM.2019.2064. [Online]. Available: https://www.researchgate.net/publication/331600548_Young's_Modulus_Measurement_of_Submicron-

thick_Aluminum_Films_Using_Fan-shaped_Silicon_Resonators (visited on 06/24/2025).

[105] M. Tiryakioğlu, J. T. Staley, and J. Campbell, "The effect of structural integrity on the tensile deformation characteristics of A206-T71 alloy castings," *Materials Science and Engineering: A*, vol. 487, no. 1, pp. 383–387, Jul. 2008, ISSN: 0921-5093. DOI: 10.1016/j.msea.2007.11.005. [Online]. Available: https://www.sciencedirect.com/science/article/pii/S0921509307018138 (visited on 07/14/2025).

[106] E. Maleki and N. Shamsaei, "A comprehensive study on the effects of surface post-processing on fatigue performance of additively manufactured AlSi10Mg: An augmented machine learning perspective on experimental observations," *Additive Manufacturing*, vol. 86, p. 104 179, Apr. 2024, ISSN: 2214-8604. DOI: 10.1016/j.addma.2024.104179. [Online]. Available: https://www.sciencedirect.com/science/article/pii/S2214860424002252 (visited on 07/10/2025).

[107] N. Gathimba and Y. Kitane, "Effect of surface roughness on tensile ductility of artificially corroded steel plates," *Journal of Constructional Steel Research*, vol. 176, p. 106 392, Jan. 2021, ISSN: 0143-974X. DOI: 10.1016/j.jcsr.2020.106392. [Online]. Available: https://www.sciencedirect.com/science/article/pii/S0143974X20309445 (visited on 07/07/2025).

[108] J. Fiocchi, A. Tuissi, and C. Biffi, "Heat treatment of aluminium alloys produced by laser powder bed fusion: A review," *Materials & Design*, vol. 204, p. 109 651, Mar. 2021. DOI: 10.1016/j.matdes.2021.109651.

[109] M. Beltrami, M. Mayumi Kikuchi, R. Sawaya Sucaria, and G. Schilive de Souza, *The influence of specimen surface roughness on tensile testing results*, en, 2017. [Online].

Available: https://www.researchgate.net/publication/323215917_The_influence_of_specimen_surface_roughness_on_tensile_testing_results (visited on 07/07/2025).

[110] G. S. Gill and W. H. Nurick, *NASA SP 8089 Liquid Rocket Engine Injectors*, 1976. [Online]. Available: https://ntrs.nasa.gov/api/citations/19760023196/downloads/19760023196.pdf (visited on 01/29/2025).

[111] X. Chen, X. Xie, H. Wu, *et al.*, "In-situ control of residual stress and its distribution in a titanium alloy additively manufactured by laser powder bed fusion," *Materials Characterization*, vol. 201, p. 112 953, Jul. 2023, ISSN: 1044-5803. DOI: 10.1016/j.matchar.2023.112953. [Online]. Available: https://www.sciencedirect.com/science/article/pii/S1044580323003121 (visited on 07/11/2025).

[112] C. Chen, Z. Xiao, Y. Wang, X. Yang, and H. Zhu, "Prediction study on in-situ reduction of thermal stress using combined laser beams in laser powder bed fusion," *Additive Manufacturing*, vol. 47, p. 102 221, Nov. 2021, ISSN: 2214-8604. DOI: 10.1016/j.addma.2021.102221. [Online]. Available: https://www.sciencedirect.com/science/article/pii/S221486042100381X (visited on 07/11/2025).

[113] *Ethics and Policies — Journal of Structural Engineering & Applied Mechanics - Golden Light Publishing ® — Trabzon*. [Online]. Available: https://www.goldenlightpublish.com/journals/jseam/1-ethics-and-policies# (visited on 07/14/2025).

APPENDICES

Appendix A

Chapter 2: Structural Optimization

Appendix A.1 Build Plate Layout



Figure A.1: Build plate with structural members and various other components for use in other works.

Appendix A.2 Test Fixture Alignment



Figure A.2: Test fixture alignment process using clamps and 1-2-3 blocks to ensure centering.

Appendix A.3 Test Data Including Outliers

The complete experimental testing results for all samples are presented in Table A.1 and Figure A.3.

Table A.1: Failure load of tested samples, outliers are in bold.

Sample	Validation	Conventional	Printed
Sample 1	15,423 N	11,230 N	19,909 N
Sample 1 re-test	N/A	10,406 N	21,067 N
Sample 2	12,116 N	**44,491 N**	22,387 N
Sample 3	14,769 N	**55,601 N**	**42,631 N**
Sample 4	N/A	10,322 N	N/A

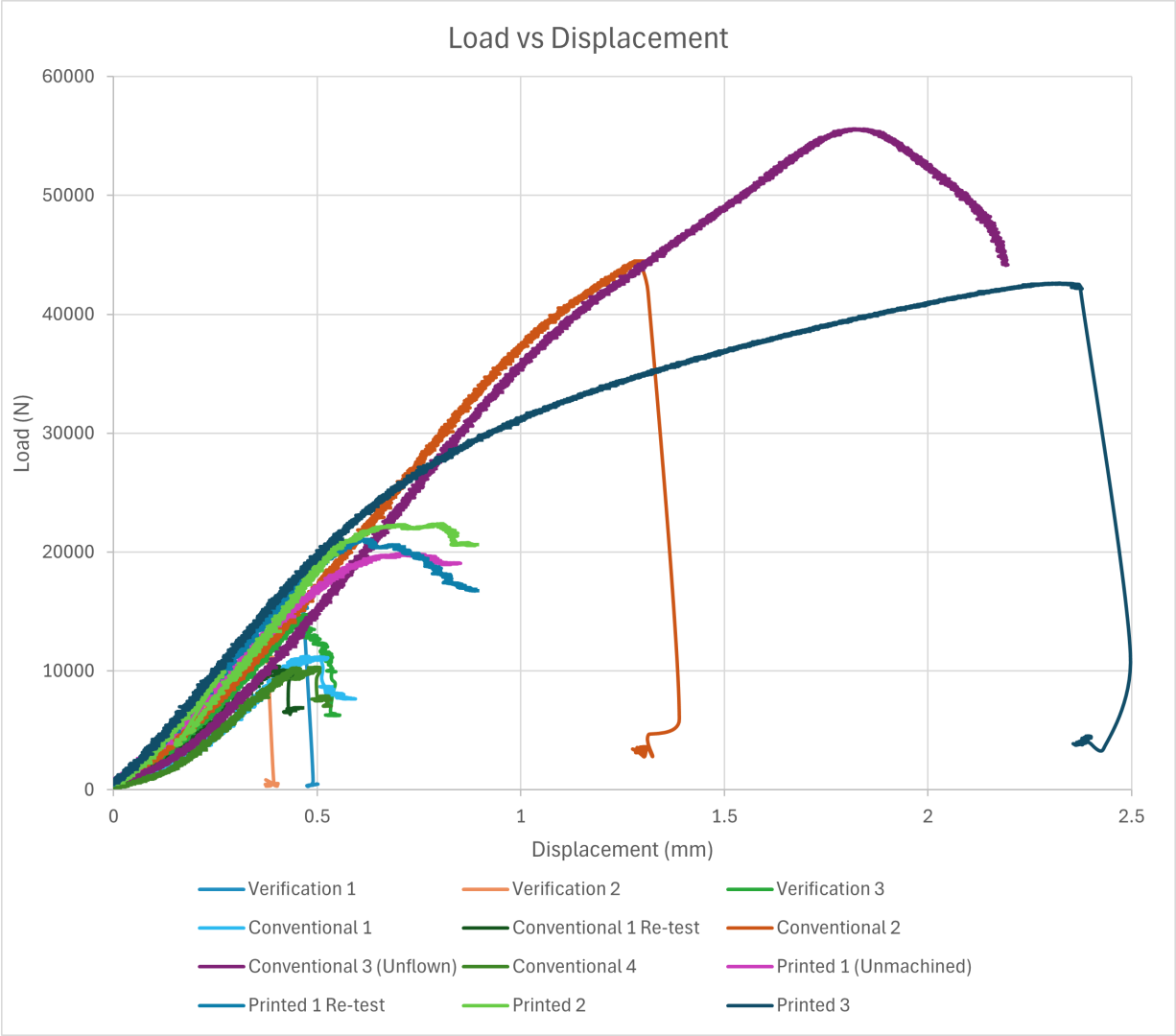


Figure A.3: Experimental test results for all samples including outliers.

Appendix B

Chapter 3: Downskin Surface Roughness Optimization

Appendix B.1 Numerical Values for Downskin Overlap Model

Table B.1: Computed values for the downskin melt pool overlap model presented in section 3.2.2. Effective thermal conductivity, K_{eff}, effective density, ρ_{eff}, and effective diffusivity, α_{eff}, are specific to AlSi10Mg.

Angle [°]	**Border ratio**	**Solid fraction**	**Relative conductivity**	**Relative solid fraction**	K_{eff} [W/(mK)]	ρ_{eff} [kg/m^3]	α_{eff} [m^2/s]
0	0.313	0.331	0.350	0.433	39.60	1863.09	2.21e-5
15	0.361	0.351	0.404	0.459	45.69	1900.38	2.50e-5
20	0.449	0.475	0.504	0.621	56.91	2136.07	2.77e-5
30	0.559	0.617	0.626	0.808	70.77	2406.06	3.05e-5
45	0.674	0.711	0.756	0.930	85.44	2583.57	3.43e-5
60	0.772	0.749	0.865	0.980	97.78	2656.66	3.82e-5
75	0.861	0.763	0.966	0.999	109.15	2683.51	4.22e-5
90	0.892	0.764	1.000	1.000	113.00	2685.00	4.37e-5

Appendix B.2 Previous Work on Downskin Roughness of 7A76 Aluminum

Optimizing Additive Manufacturing of Complex Components for Aerospace

Zachariah Mears, JD Zhu, Sagar Patel, Allan David Rogalsky, Jerry Ratthapakdee, Mihaela Vlasea - Multi-Scale Additive Manufacturing Laboratory, University of Waterloo, Waterloo, ON, N2L 3W8, Canada

Background

Metal Additive Manufacturing (AM), Specifically Laser Powder Bed Fusion (LPBF) presents many new opportunities for greatly improving the manufacturing of aerospace components. Of particular interest are the new design possibilities created by AM.

AM allows for complex geometries that would not be possible with conventional manufacturing methods such as:

- **Optimized shells and lattices** for high-rigidity light-weight components
- **Part consolidation** that reduces manufacturing complexity, failure modes, size, and weight
- **Integrated fluid channels** that allow conformal cooling and very compact lightweight fluid systems

There are also manufacturing challenges unique to AM that must be considered:

- **Surface roughness**: Compared to conventional manufacturing techniques such as machining, LPBF has a quite high surface roughness, often requiring additional machining on critical surfaces
- **Overhang angles**: there is a limit to the angle at which parts can be printed without supports. Traditionally, this limit has been 45^0
- **Support material removal**: parts must be designed so that supports can be removed after printing. This means that supports cannot be used on parts with complex internal geometry where the supports are inaccessible

While these challenges will likely never be fully removed, minimizing these limitations will increasingly allow more parts to be additively manufactured, and allow for further optimization of parts.

New Material: 7A76 Aluminum

Currently MSAM is working on printing 7A76 aluminum. This is a high strength alloy derived from 7075. Printing of very high strength materials is particularly exciting, as Design for Additive Manufacturing (DfAM) can allow for significant improvements in rigidity, part size, and weight. However, maximum stress is not easily reduced, so access to high strength alloys is important to facilitate high performance aerospace components.

Down-Skin Surface Optimization

The goal of this study was to determine printing recipes that reduce the surface roughness of overhanging surfaces (down-skin) and to reduce the maximum overhang angle that can be printed with 7A76 Aluminum.

Methods

A test coupon was designed that allows testing of 5 down-skin angles as shown in Figure 1. A total of 36 coupons were printed across 4 prints. Each of these coupons tested a different combination of laser power, velocity, and focus. Numerical models developed by MSAM were used to predict the melting behavior of each recipe for each down-skin angle and select appropriate recipes to test [1, 2]

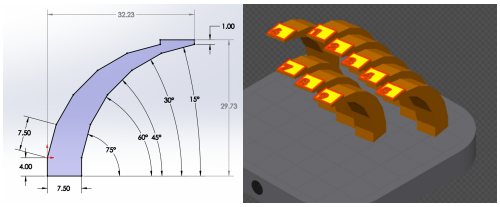


Figure 1: Down-skin surface optimization coupon design

Results

Based on the printed coupons, it was found that by using a focused beam running at maximum power and high speed, the coupons could be printed with relatively good surface roughness at angles as low as 15^0, significantly better than the traditional guideline of a 45^0 maximum overhang. The most promising print is shown in Figure 2, with samples 28-31 showing the best results.

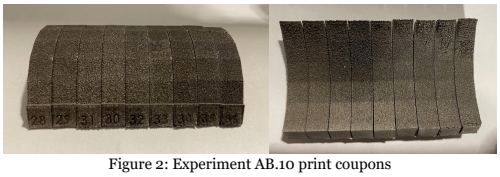


Figure 2: Experiment AB.10 print coupons

Continuing Work

Currently, surface roughness measurements and metallography is being done on the samples to determine the quantitative performance of the samples and examine the quality of the microstructure. Figure 3 shows the first roughness measurements done on sample 30.

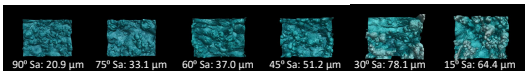


Figure 3: Surface roughness measurements of sample 30

Further work will include testing different scan strategies and applying these optimized recipes to complex functional components.

Application Demonstrators

To highlight the use cases of AM for aerospace, a pair of demonstrator components have been printed:

Rocket Structural Member: By using a hollow shell with a variable thickness to match the applied load and an internal isogrid, this component achieves 3x the buckling resistance of it's conventionally manufactured counterpart for the same weight and maximum stress.

Liquid Rocket Injector: By using Metal AM, optimized flow paths can be made for better fuel mixing. In addition, multiple soldered components ca combined into a single part.

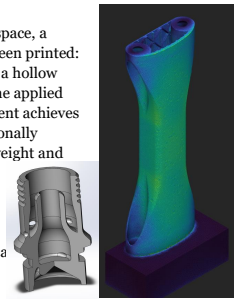


Figure 4: Demonstrator parts

Acknowledgements

This research was made possible through funding support provided through the WISA Research-For-Impact call for proposal, project "Additive manufacturing of economically-sustainable high-strength aluminium alloys for high-performance aerospace applications ". Additional support with regards to powder material systems courtesy of Metal Powder Works and The Barnes Global Advisors.

References

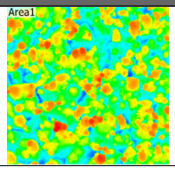
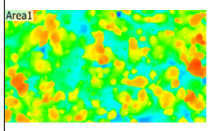
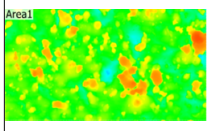
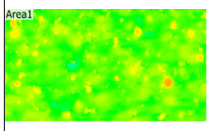
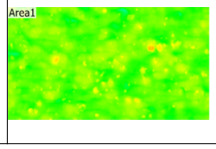
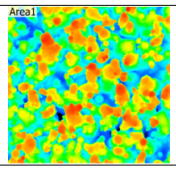
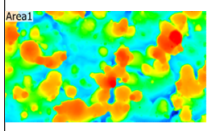
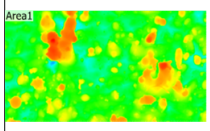
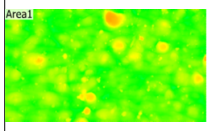
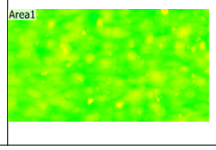
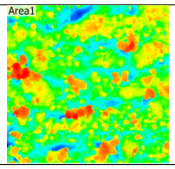
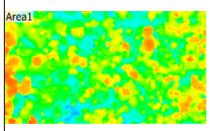
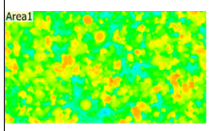
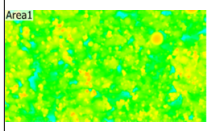
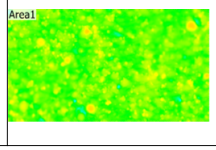
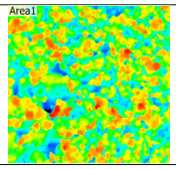
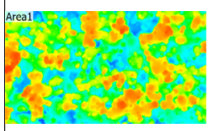
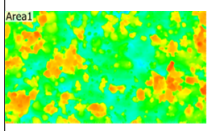
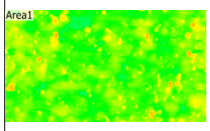
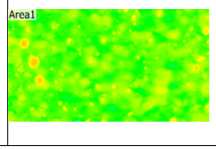
[1] S. Patel and M. Vlasea, "Melting modes in laser powder bed fusion," Materialia, vol. 9, p. 100591, Mar. 2020, doi: 10.1016/j.mtla.2020.100591.

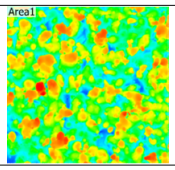
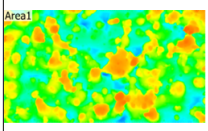
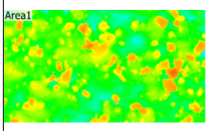
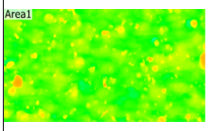
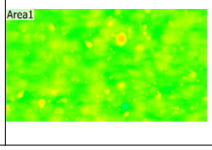
[2] A.D. Rogalsky, S. Patel, M. Vlasea, and A. Molavi-Kakhki "Improving Surface Quality and Geometric Fidelity of Water Atomized Pure Iron in Laser Powder Bed Fusion" AMPM 2022 Conference Proceedings, pp 356-374

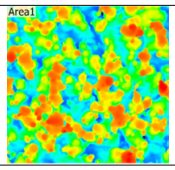
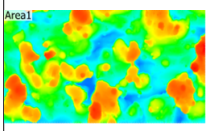
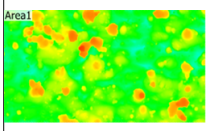
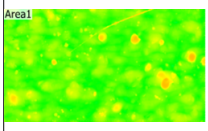
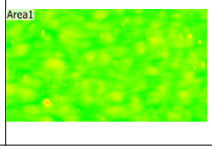
Funded by:
Federal Economic Development Agency for Southern Ontario

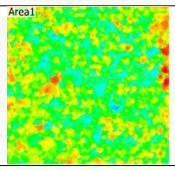
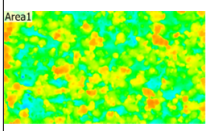
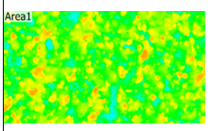
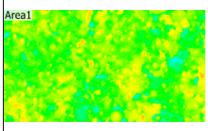
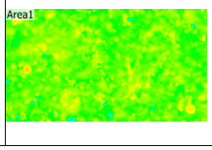
Financé par :
Agence fédérale de développement économique pour le Sud de l'Ontario

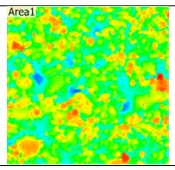
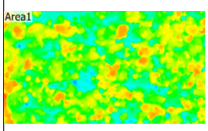
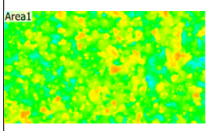
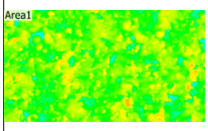
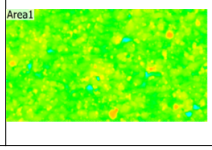
Appendix B.3 Complete Surface Roughness Measurements

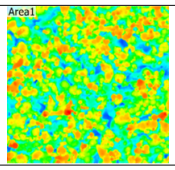
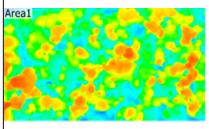
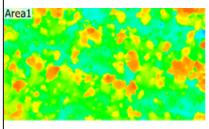
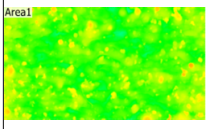
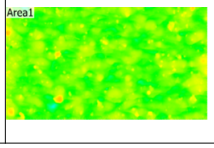
Sample	Surface roughness						
	Height Map	Measurements					
		Sa	Sz	Str	Spc	Sdr	Sq
		µm	µm		1/mm		µm
S1_20down		72.6039	669.3187	0.8017	909.0081	3.286	90.1152
S1_30down		60.1051	547.3091	0.5748	1497.9705	3.019	74.6280
S1_45down		35.2808	398.9391	0.6644	1217.2187	1.543	49.0533
S1_60down		13.6514	214.3618	0.9481	919.6215	0.5607	19.3071
S1_75down		10.7101	176.0884	0.6792	783.9644	0.2974	14.6853
S2_20down		98.6335	726.5416	0.8418	1269.6616	4.432	119.1494
S2_30down		97.8039	662.0595	0.6167	1520.0375	5.128	115.1899
S2_45down		44.2980	491.5481	0.5675	1182.5159	1.376	61.8564
S2_60down		14.0711	194.4954	0.7799	1259.5970	0.5236	20.4508
S2_75down		8.9395	129.9722	0.9052	878.2042	0.2787	11.8379
S3_20down		65.4753	736.2388	0.5883	1170.2399	3.519	87.0910
S3_30down		51.4932	433.2015	0.2790	1440.2466	2.503	65.1001
S3_45down		37.5555	333.5285	0.9317	1351.3793	1.895	46.8244
S3_60down		23.6937	271.5260	0.8743	1356.0692	1.449	31.1750
S3_75down		13.6901	207.0007	0.7734	835.8250	0.4037	18.4330
S4_20down		76.1013	770.6539	0.8046	1182.8096	4.634	94.7762
S4_30down		79.0386	530.8183	0.7618	1453.1735	4.027	94.8732
S4_45down		55.8046	412.9324	0.5692	1413.6626	2.752	67.5392
S4_60down		17.4860	208.4760	0.8109	1324.9778	0.8541	23.3538
S4_75down		13.4577	186.9829	0.9460	892.5756	0.3704	18.1943

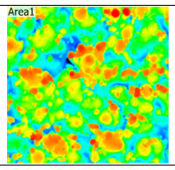
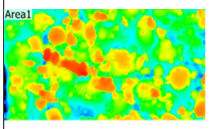
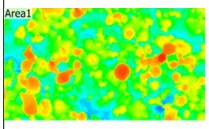
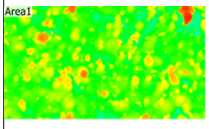
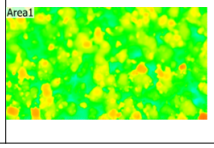
S5_20down		69.8978	639.1142	0.8755	1556.8415	3.108	87.3238
S5_30down		60.0941	447.2004	0.8872	1335.2353	2.306	72.6685
S5_45down		35.3204	339.9320	0.7776	1021.8961	1.482	46.6404
S5_60down		14.7785	217.4050	0.8355	1729.5416	1.001	21.1239
S5_75down		10.3222	166.1718	0.8448	1306.6344	0.4854	14.0382

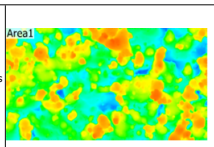
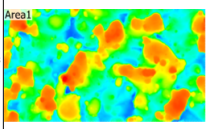
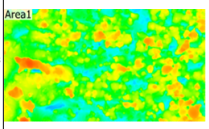
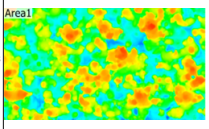
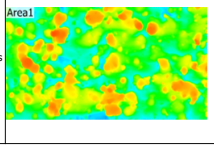
S6_20down		97.8320	726.9779	0.8693	1363.6657	3.806	118.1630
S6_30down		87.4928	552.4052	0.7040	1124.8795	4.366	106.4543
S6_45down		36.7124	381.2335	0.5914	1166.7391	1.234	50.5524
S6_60down		12.5116	157.6265	0.8814	1444.0283	0.7289	18.2922
S6_75down		8.0820	140.5261	0.8387	1125.8716	0.3597	10.8366

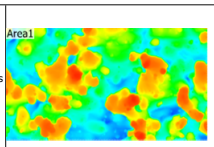
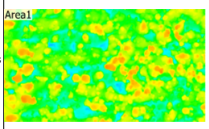
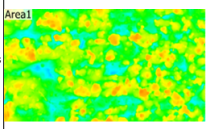
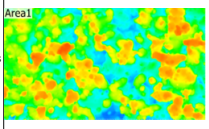
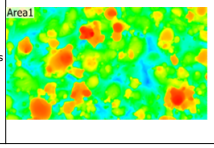
S7_20down		48.5055	560.9815	0.8420	835.1702	2.483	63.5937
S7_30down		44.2957	389.7002	0.8456	1265.9606	2.305	55.2219
S7_45down		31.4699	302.6741	0.7274	1002.8446	1.792	40.3341
S7_60down		23.7713	255.4787	0.7142	1347.7498	1.263	30.4085
S7_75down		13.5393	223.1605	0.8634	940.5102	0.4678	18.2554

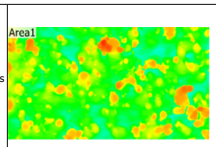
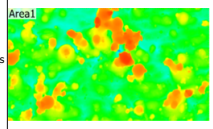
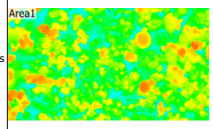
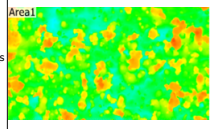
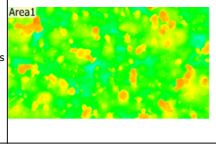
S8_20down		51.8260	618.3394	0.7755	1337.0705	2.507	66.8647
S8_30down		44.8815	426.5027	0.7334	1409.2683	2.199	56.2445
S8_45down		30.8825	332.5823	0.7810	905.6050	1.486	39.4412
S8_60down		22.7727	264.7601	0.7956	1248.8073	1.249	29.5466
S8_75down		14.7545	257.0596	0.7971	1169.2937	0.6360	20.3671

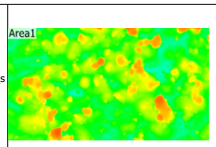
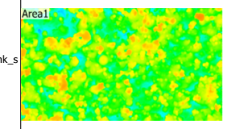
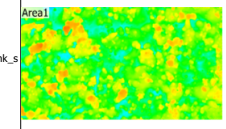
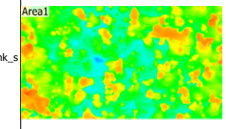
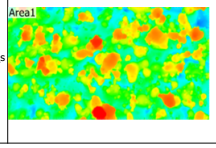
S9_20down		71.6166	681.5508	0.8696	371.5197	4.056	88.2810
S9_30down		70.5600	547.0692	0.7045	1473.6953	3.234	84.4992
S9_45down		49.4971	405.1365	0.6121	1418.6427	2.300	62.3628
S9_60down		17.7108	196.9315	0.6240	1110.1851	0.7615	23.2583
S9_75down		14.3521	209.8856	0.9196	761.5882	0.3352	18.9611

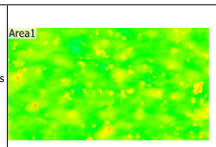
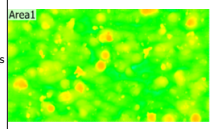
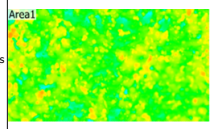
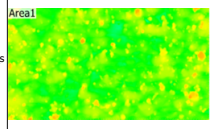
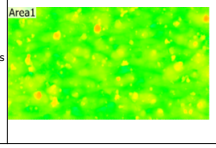
S10_20down		80.4883	709.5985	0.6914	1228.8816	3.884	101.8215
S10_30down		69.0612	851.2960	0.5305	1378.7671	3.641	89.4063
S10_45down		56.6716	513.8221	0.7745	1022.1929	2.447	73.7330
S10_60down		27.9079	400.4818	0.7591	1513.3824	1.585	41.5959
S10_75down		30.3324	313.6283	0.8747	950.7741	0.6369	37.3362

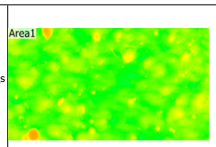
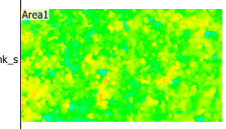
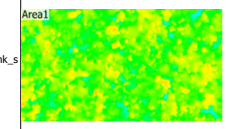
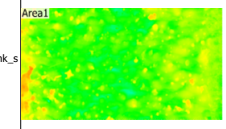
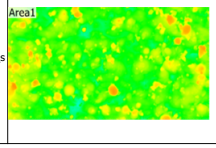
30deg_down_thk_sample_1		67.0746	487.3564	0.8536	1126.8231	2.472
30deg_down_thk_sample_2		92.4882	612.2845	0.7318	1284.6519	2.853
30deg_down_thk_sample_3		47.0655	420.5792	0.5286	1311.5075	2.167
30deg_down_thk_sample_4		68.8986	516.6410	0.8401	1105.8384	3.410
30deg_down_thk_sample_5		55.5421	429.6146	0.6929	1442.1777	2.093

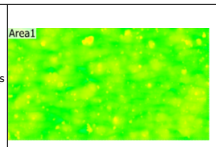
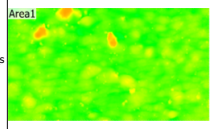
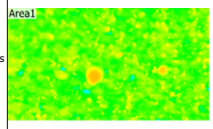
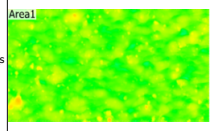
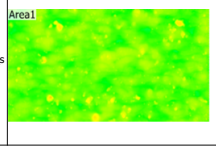
30deg_down_thk_sample_6		91.9828	559.5225	0.7712	1389.6767	3.160
30deg_down_thk_sample_7		40.0889	336.8083	0.6684	1243.5200	1.903
30deg_down_thk_sample_8		40.6825	339.6248	0.5027	1111.9836	1.696
30deg_down_thk_sample_9		65.8639	470.6761	0.6468	1286.4927	2.994
30deg_down_thk_sample_10		62.3146	520.8498	0.8647	1095.3142	2.232

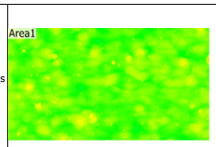
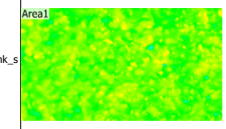
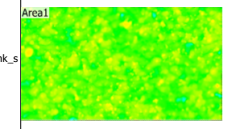
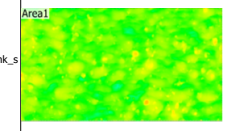
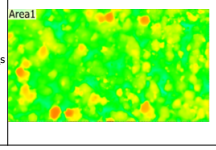
45deg_down_thk_sample_1		40.5102	414.7631	0.8025	1558.7340	2.587
45deg_down_thk_sample_2		50.2200	476.1072	0.6567	2341.2463	2.873
45deg_down_thk_sample_3		45.1697	396.5665	0.7554	1800.1852	3.567
45deg_down_thk_sample_4		48.4960	450.7727	0.7966	1825.3245	3.913
45deg_down_thk_sample_5		30.8289	310.4098	0.8776	1964.5381	2.025

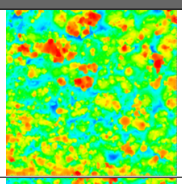
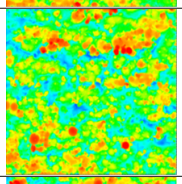
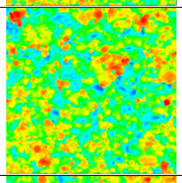
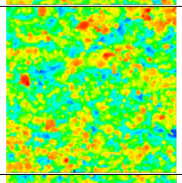
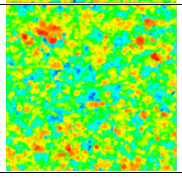
45deg_down_thk_sample_6		35.6190	330.6587	0.7885	1970.9826	1.942
45deg_down_thk_sample_7		37.5997	385.0549	0.8253	1735.0779	3.021
45deg_down_thk_sample_8		35.8323	357.0769	0.8041	1906.4408	2.841
45deg_down_thk_sample_9		49.8662	434.1937	0.6655	1959.6761	3.645
45deg_down_thk_sample_10		66.7533	607.3157	0.6318	1661.6064	5.068

60deg_down_thk_sample_1		13.8768	301.6175	0.7550	776.5816	0.5309
60deg_down_thk_sample_2		18.2613	202.1502	0.8213	1172.2313	0.5949
60deg_down_thk_sample_3		25.6955	282.7992	0.8820	1347.1854	1.281
60deg_down_thk_sample_4		18.2473	201.1014	0.8385	1177.4382	0.7944
60deg_down_thk_sample_5		13.8174	196.0709	0.8062	749.8419	0.4791

60deg_down_thk_sample_6		14.2016	208.1202	0.8913	827.2985	0.3709
60deg_down_thk_sample_7		22.7613	237.4996	0.8224	1066.8610	1.103
60deg_down_thk_sample_8		23.0509	239.2765	0.8786	1631.4281	1.395
60deg_down_thk_sample_9		21.0952	265.8579	0.5124	1022.2228	0.6730
60deg_down_thk_sample_10		24.2262	249.1027	0.8908	1033.9731	0.8712

75deg_down_thk_sample_1		10.2708	129.0709	0.7078	923.4268	0.3528
75deg_down_thk_sample_2		11.1991	193.1792	0.7218	981.4290	0.3406
75deg_down_thk_sample_3		14.3224	236.5651	0.8209	552.6021	0.4744
75deg_down_thk_sample_4		12.9593	162.3308	0.8415	879.5592	0.3521
75deg_down_thk_sample_5		10.1145	160.1113	0.7319	1117.8232	0.4088

75deg_down_thk_sample_6		9.8232	152.1975	0.7446	526.6482	0.2076
75deg_down_thk_sample_7		13.5316	184.2530	0.8678	822.2031	0.4258
75deg_down_thk_sample_8		13.4508	193.2117	0.6764	983.3078	0.5951
75deg_down_thk_sample_9		14.6596	178.9942	0.6917	1062.0334	0.4861
75deg_down_thk_sample_10		26.7141	254.7778	0.8472	1259.2258	0.6826

File name	Surface roughness					Main image
	Measurements					
	Sa	Sz	Str	Spc	Sdr	Height
	µm	µm		1/mm		
20deg_core_power_sample_1	51.158	496.630	0.600	1515.379	2.776	
20deg_core_power_sample_2	50.943	482.554	0.463	1447.632	3.266	
20deg_core_power_sample_3	48.201	460.417	0.693	1515.179	3.092	
20deg_core_power_sample_4	46.162	520.741	0.580	1476.046	3.335	
20deg_core_power_sample_5	44.499	497.020	0.656	1450.762	3.246	

Appendix B.4 Analysis of Variance Code

```
import pandas as pd
import numpy as np
import pingouin as pg

df = pd.read_excel('Facet_Surface roughness.xlsx', 'python stats',
↪  header=0)

#filter for data that exist in all combinations
subset = df.loc[df['Angle'].isin([30, 45, 60, 75])]
subset = subset.loc[subset['Downskin'].isin(['# 1', '# 3', '# 4', '# 5'])]
#print(subset)


# test for significant effect from the core
aov = pg.anova(dv='Roughness', between=['Angle', 'Downskin', 'Core'],
↪  data=subset, detailed=True)

SSt = sum(aov['SS'])
aov['contribution'] = aov['SS']/SSt #Calculate the percent contribution
↪  to variance (Design and Analysis of experiments pg 217)
print(SSt)
print(aov)
```

```
#test for significant effect from the thickness
aov = pg.anova(dv='Roughness', between=['Angle', 'Downskin', 'Thickness'],
↪  data=subset, detailed=True)

SSt = sum(aov['SS'])
aov['contribution'] = aov['SS']/SSt #Calculate the percent contribution
↪  to variance (Design and Analysis of experiments pg 217)
print(SSt)
print(aov)
```

The following is the output for the above code:

```
$ python facet_roughness_stats.py
36949.236119140005
               Source            SS    DF  ...         p-unc       np2  contribution
0               Angle  30827.936508   3.0  ...  8.617570e-33  0.990994      0.834332
1            Downskin   1265.306513   3.0  ...  5.722487e-12  0.818717      0.034244
2                Core    168.767276   1.0  ...  1.156104e-04  0.375927      0.004568
3      Angle*Downskin   4215.076477   9.0  ...  9.320519e-17  0.937674      0.114077
4          Angle*Core    135.664018   3.0  ...  5.030903e-03  0.326246      0.003672
5       Downskin*Core     32.026100   3.0  ...  3.186329e-01  0.102584      0.000867
6 Angle*Downskin*Core     24.290128   9.0  ...  9.665481e-01  0.079781      0.000657
7            Residual    280.169098  32.0  ...           NaN       NaN      0.007583

[8 rows x 8 columns]
36949.23611913994
                   Source          SS    DF  ...         p-unc      np2  contribution
0                   Angle  30827.9365   3.0  ...  4.69112e-29  0.98457      0.834332
1                Downskin   1265.3065   3.0  ...  4.55885e-09  0.72379      0.034244
```

```
2                Thickness      0.3250   1.0  ...  8.84227e-01  0.00067      0.000009
3           Angle*Downskin   4215.0764   9.0  ...  2.41337e-13  0.89722      0.114077
4          Angle*Thickness     46.6618   3.0  ...  3.92067e-01  0.08812      0.001263
5       Downskin*Thickness     34.5951   3.0  ...  5.22506e-01  0.06685      0.000936
6 Angle*Downskin*Thickness     76.4793   9.0  ...  8.16539e-01  0.13673      0.002070
7                 Residual    482.8551  32.0  ...          NaN      NaN      0.013068

[8 rows x 8 columns]
```

Appendix C

Chapter 4: Tensile Properties

Appendix C.1 Tensile Data Processing Code

Appendix C.1.1 process_samples.py

This is the top-level script which handles loading data and calling the calculate properties function for each sample.

```
from unicodedata import name
from calculate_properties import calculate_properties
import pandas as pd
import numpy as np
from glob import glob

gauge_length = 25.0 #mm

df = pd.read_excel('../tensile testing.xlsx', 'for python', header=0,
↪  skiprows=[1])

#Try writing to the file now to make sure it isn't open
df.to_excel('../tensile testing python results.xlsx')

#Manual Measurements
df['E'] = np.zeros(len(df))
df['Yeild'] = np.zeros(len(df))
df['UTS'] = np.zeros(len(df))
df['elongation'] = np.zeros(len(df))
```

```
#Ideal Measurements
df['E_corrected'] = np.zeros(len(df))
df['Yeild_corrected'] = np.zeros(len(df))
df['UTS_corrected'] = np.zeros(len(df))

#CT Measurements
df['E_CT'] = np.zeros(len(df))
df['Yeild_CT'] = np.zeros(len(df))
df['UTS_CT'] = np.zeros(len(df))



for index, row in df.iterrows():
    name = row['Name']
    print('Processing ', name, ' . . .')

    filepath = glob('../Test Data/*'+ str(name) + '/*.csv',
    ↪  recursive=True)[0]
    print(filepath)
    test_data = pd.read_csv(filepath,header=6,skiprows=[7])

    ################################### Calculate Properties Based on
    ↪  Manual Measurements  ###################################
    area = row['Area'] # mm^2
```

```
stress_data = (test_data['Load ']/area)*1000.0 # 1000 * kN / mm^2 ->
↪  MPa
strain_data = test_data['Extensometer ']/gauge_length # mm/mm
E, Sy, UTS, elongation = calculate_properties(stress_data,
↪  strain_data, plot=False, name=name)

print(f'The elastic modulus is {round(E/1000.0, 2)} GPa')
print(f'The yield strength is {round(Sy, 2)} MPa')
print(f'The ultimate tensile strength is {round(UTS, 2)} MPa')
print(f'The elongation at break is {round(elongation, 3)}')

df.loc[index, 'E'] = E
df.loc[index, 'Yeild'] = Sy
df.loc[index, 'UTS'] = UTS
df.loc[index, 'elongation'] = elongation

################################### Calculate Properties Based on
↪  Corrected Dimensions  ###################################
area = row['Corrected Area'] # mm^2

stress_data = (test_data['Load ']/area)*1000.0 # 1000 * kN / mm^2 ->
↪  MPa
E, Sy, UTS, elongation = calculate_properties(stress_data,
↪  strain_data, plot=False, name=name)
```

```
        df.loc[index, 'E_corrected'] = E
        df.loc[index, 'Yeild_corrected'] = Sy
        df.loc[index, 'UTS_corrected'] = UTS
        ################################### Calculate Properties Based on CT
        ↪  Scan Results  ###################################
        area = row['CT Area'] # mm^2

        if(area > 0):
            stress_data = (test_data['Load ']/area)*1000.0 # 1000 * kN / mm^2
            ↪  -> MPa
            E, Sy, UTS, elongation = calculate_properties(stress_data,
            ↪  strain_data, plot=False, name=name)

            df.loc[index, 'E_CT'] = E
            df.loc[index, 'Yeild_CT'] = Sy
            df.loc[index, 'UTS_CT'] = UTS

df.to_excel('../tensile testing python results.xlsx')
```

Appendix C.1.2 calculate_properties.py

This file contains the functions for calculating tensile properties.

```
#  imports
from cProfile import label
import numpy as np
```

```
import pandas as pd
import matplotlib.pyplot as plt
from scipy.stats import linregress


#calculates the intersection of two lines defined by 4 points
def intersection_point(Ax1, Ay1, Ax2, Ay2, Bx1, By1, Bx2, By2):
    d = (By2-By1)*(Ax2-Ax1)-(Bx2-Bx1)*(Ay2-Ay1)
    if d:
        uA = ((Bx2-Bx1)*(Ay1-By1)-(By2-By1)*(Ax1-Bx1))/d
        uB = ((Ax2-Ax1)*(Ay1-By1)-(Ay2-Ay1)*(Ax1-Bx1))/d
    else:
        return None
    if not(0 <= uA <= 1 and 0 <= uB <= 1):
        return None
    x = Ax1 + uA * (Ax2 - Ax1)
    y = Ay1 + uA * (Ay2 - Ay1)

    return x, y

# Stress in MPa and strain in mm/mm
def calculate_properties(stress, strain, plot=True, name=''):
    strain_array = np.array(strain)
    stress_array = np.array(stress)
```

```
#Calculate UTS
UTS_index = np.argmax(stress_array)
UTS = stress_array[UTS_index]
UTS_strain = strain_array[UTS_index]

""" #Plot full stress strain curve
fig,ax = plt.subplots()
ax.plot(strain, stress)
ax.set_xlabel('Strain (mm/mm)')
ax.set_ylabel('Stress (MPa)')
ax.set_title('Stress-Strain Curve')

plt.show() """

# Find the elastic modulus
# use stress and strain values from stress=0 to stress= 25% + initial
↪  offset of UTS MPa and only at strains < 25% of strain at break
linear_stress_mask = (stress < (UTS*0.25 + stress[0])) & (stress > 0)
linear_strain_mask = strain < UTS_strain*0.25
linear_stress = stress[linear_stress_mask & linear_strain_mask]
linear_strain = strain[linear_stress_mask & linear_strain_mask]


linear_regression_output = linregress(linear_strain, linear_stress)
E = linear_regression_output[0]
```

```
#print(f'The elastic modulus is {round(E/1000.0, 2)} GPa')
print("test: ")
print(linear_regression_output)
print(stress[0])

# calculate the yield strength. add offset to acount for non-zero
↪  stress at start (strain should be zero)
stress_offset = E*(strain-0.002) + stress[0]
f = np.array(stress)
g = np.array(stress_offset)
yield_stress_index = np.argwhere(np.diff(np.sign(f - g)))[0][0]

#calculate yeild strength using the intersection function
first = yield_stress_index
second = first + 1
# A points from the stress strain curve
Ax1 = strain_array[first]
Ay1 = stress_array[first]
Ax2 = strain_array[second]
Ay2 = stress_array[second]
# B points from the offset line
Bx1 = strain_array[first]
By1 = stress_offset[first]
Bx2 = strain_array[second]
```

```
By2 = stress_offset[second]

# run our function that finds the intersection point
Sy_strain, Sy = intersection_point(Ax1,Ay1,Ax2,Ay2,Bx1,By1,Bx2,By2)

#print(f'The yield strength calculated programmatically is
↪  {round(Sy,2)} MPa')

if(plot):
    fig,ax = plt.subplots()

    ax.plot(strain_array,stress_array) #plot stress vs strain
    ax.plot(linear_strain, linear_stress, 'r', label='Linear region')
    ax.plot(strain_array,stress_offset, label='0.2% offset') #plot
    ↪  0.2% offset
    ax.plot(Sy_strain,Sy,'go', label='Yield point') #Plot yeild point
    ax.plot(UTS_strain, UTS, 'ro', label='UTS point') #Plot UTS point

    ax.set_xlabel('Strain (mm/mm)')
    ax.set_ylabel('Stress (MPa)')
    ax.set_title(name + ' Stress-Strain Curve')

    #ax.set_ylim([0,300])
    ax.set_ylim([0,UTS*1.1])
    #ax.set_xlim([0,0.01])
```

```
        ax.legend()

        plt.show()

    elongation = UTS_strain #TODO: does not consider ductile faliure

    return E, Sy, UTS, elongation
```

Appendix C.2 Complete Tensile Data

Table C.1: Measured tensile properties for all samples. Sample dimensions can be found in Table 4.5.

Name	Young's Modulus (GPa)	Yield Strength (MPa)	UTS (MPa)	Elongation (%)
1XTK-T	71.61	262.60	428.09	6.47
1XTK-B	71.50	262.45	414.16	5.13
2XTK-T	71.03	262.27	396.29	4.09
2XTK-B	70.06	261.43	436.10	8.09
3XTK-T	69.38	263.68	434.32	7.21
3XTK-B	69.83	263.66	425.88	6.21
1YTK-T	73.44	263.96	423.58	5.52
1YTK-B	73.12	267.98	435.20	7.22
2YTK-T	70.70	264.68	432.93	6.77

2YTK-B	70.74	264.84	430.50	6.47
3YTK-T	70.31	262.69	431.49	6.87
3YTK-B	70.38	265.99	423.58	5.82
1XTN-T	67.88	266.17	421.44	6.22
1XTN-B	67.98	267.22	412.89	5.36
2XTN-T	69.31	266.07	407.72	4.94
2XTN-B	66.73	266.92	419.04	6.19
3XTN-T	68.19	264.93	401.28	4.58
3XTN-B	69.82	266.41	423.87	6.75
1YTN-T	67.84	270.66	429.12	6.69
1YTN-B	68.17	271.15	423.94	6.01
2YTN-T	71.25	267.73	421.14	5.85
2YTN-B	71.67	268.43	422.49	6.07
3YTN-T	67.81	265.71	416.86	5.84
3YTN-B	66.97	265.72	418.42	6.12
20-1	50.50	201.37	238.80	1.37
20-2	54.02	193.97	211.40	0.84
30-1	52.97	219.65	343.58	4.13
30-2	65.28	219.04	345.99	4.40
45-1	67.09	234.43	357.21	3.72
45-2	59.37	233.61	361.16	4.15
60-1	61.04	259.35	418.92	6.57
60-2	64.21	259.00	399.78	4.81
75-1	64.03	263.58	419.10	6.53
75-2	64.27	262.77	402.69	4.90

Round 1	70.54	243.08	399.05	3.57
Round 2	68.77	222.82	441.51	6.61
Round 3	68.57	243.54	438.78	5.25
Round 4	67.60	223.31	427.60	5.15
Round 5	69.90	243.14	466.19	7.45
Round 6	67.11	216.15	444.84	8.58
Round 7	69.42	243.74	469.95	8.54
Round 8	66.50	218.90	443.15	7.25
Round 9	68.61	243.56	460.39	6.60
Round 10	65.68	218.24	443.09	7.31
Flat 1	66.34	238.96	399.63	3.68
Flat 2	69.80	221.95	374.77	3.14
Flat 3	67.15	236.24	392.29	3.50
Flat 4	63.19	222.86	404.28	4.42
Flat 5	65.86	242.88	418.80	4.20
Flat 6	62.49	217.76	409.53	5.10
Flat 7	66.14	239.78	416.21	4.05
Flat 8	64.00	219.14	375.03	3.31
Flat 9	67.66	245.29	413.21	3.77
Flat 10	63.66	219.03	379.37	3.47

Appendix C.3 Analysis of Variance Code

Appendix C.3.1 Surface Roughness ANOVA Code

```
import pandas as pd
import numpy as np
import pingouin as pg

df = pd.read_excel('../tensile testing.xlsx', 'python roughness stats',
↪  header=0)

df = df.loc[df['Orientation'].isin(['X', 'Y'])] #filter for only
↪  horizontal samples

aov = pg.anova(dv='Roughness', between=['Thick', 'Position', 'Side',
↪  'Orientation'], data=df, detailed=True)
SSt = sum(aov['SS'])
aov['contribution'] = aov['SS']/SSt #Calculate the percent contribution
↪  to variance (Design and Analysis of experiments pg 217)
print(SSt)
print(aov)
```

The following is the output for the above code:

```
$ python tensile_roughness_stats.py
67.00735814050395
                    Source       SS  DF ...        p-unc       np2 contribution
```

```
0                           Thick  0.13570  1.0 ...  6.16240e-01  0.00794     0.00202
1                        Position  3.33488  1.0 ...  1.73653e-02  0.16438     0.04976
2                            Side  0.02137  1.0 ...  8.42064e-01  0.00125     0.00031
3                     Orientation 26.62760  1.0 ...  4.83259e-08  0.61100     0.39738
4                   Thick*Position  2.80448  1.0 ...  2.80650e-02  0.14195     0.04185
5                       Thick*Side  1.80585  1.0 ...  7.41151e-02  0.09627     0.02695
6                     Position*Side  2.09201  1.0 ...  5.55146e-02  0.10985     0.03122
7                Thick*Orientation  0.23855  1.0 ...  5.06998e-01  0.01387     0.00356
8             Position*Orientation  3.22014  1.0 ...  1.92321e-02  0.15963     0.04805
9                 Side*Orientation  8.32981  1.0 ...  3.86018e-04  0.32947     0.12431
10             Thick*Position*Side  0.11063  1.0 ...  6.50760e-01  0.00648     0.00165
11      Thick*Position*Orientation  1.11596  1.0 ...  1.56401e-01  0.06176     0.01665
12          Thick*Side*Orientation  0.02457  1.0 ...  8.30843e-01  0.00144     0.00036
13       Position*Side*Orientation  0.12992  1.0 ...  6.23825e-01  0.00760     0.00193
14 Thick*Position*Side*Orientation  0.06369  1.0 ...  7.31040e-01  0.00374     0.00095
15                        Residual 16.95212 32.0 ...          NaN      NaN     0.25298

[16 rows x 8 columns]
```

Appendix C.3.2 Tensile Properties ANOVA Code

Note: The below code and output is for the horizontal samples and filters out data other than the X and Y samples. For the overhang and vertical samples, the only changes are that this filter is adjusted to only include those results instead, and the tested variables are adjusted as appropriate.

```
import pandas as pd
import pingouin as pg
```

```
pd.set_option('display.precision', 2)

df = pd.read_excel('../tensile testing.xlsx', 'python stats', header=0)

df = df.loc[df['Orientation'].isin(['X', 'Y'])] #Filter for only X and Y
↪  samples

aov = pg.anova(dv='Yeild_corrected', between=['Thick', 'Orientation',
↪  'Position'], data=df, detailed=True)
print('Yeild_corrected:')
SSt = sum(aov['SS'])
aov['contribution'] = aov['SS']/SSt #Calculate the percent contribution
↪  to variance (Design and Analysis of experiments pg 217)
print(SSt)
print(aov)

aov = pg.anova(dv='UTS_corrected', between=['Thick', 'Orientation',
↪  'Position'], data=df, detailed=True)
print('UTS_corrected:')
SSt = sum(aov['SS'])
aov['contribution'] = aov['SS']/SSt
print(SSt)
print(aov)
```

```
aov = pg.anova(dv='elongation', between=['Thick', 'Orientation',
↪  'Position'], data=df, detailed=True)
print('elongation:')
SSt = sum(aov['SS'])
aov['contribution'] = aov['SS']/SSt
print(SSt)
print(aov)

aov = pg.anova(dv='E_corrected', between=['Thick', 'Orientation',
↪  'Position'], data=df, detailed=True)
print('E:')
SSt = sum(aov['SS'])
aov['contribution'] = aov['SS']/SSt)
print(SSt)
print(aov)
```

The following is the output for the above code:

```
$ python tensile_stats.py
Yeild_corrected:
148.19689921779772
                         Source     SS   DF  ...     p-unc       np2  contribution
0                         Thick  69.66  1.0  ...  6.63e-05  6.41e-01      4.70e-01
1                   Orientation  27.61  1.0  ...  3.96e-03  4.14e-01      1.86e-01
2                      Position   5.08  1.0  ...  1.69e-01  1.15e-01      3.42e-02
3            Thick * Orientation   0.23  1.0  ...  7.61e-01  5.97e-03      1.58e-03
```

	Source	SS	DF	...	p-unc	np2	contribution
4	Thick * Position	0.15	1.0	...	8.08e-01	3.81e-03	1.01e-03
5	Orientation * Position	1.65	1.0	...	4.23e-01	4.05e-02	1.11e-02
6	Thick * Orientation * Position	4.74	1.0	...	1.82e-01	1.08e-01	3.20e-02
7	Residual	39.08	16.0	...	NaN	NaN	2.64e-01

[8 rows x 8 columns]

UTS_corrected:

2409.272915080205

	Source	SS	DF	...	p-unc	np2	contribution
0	Thick	367.51	1.0	...	0.07	1.91e-01	1.53e-01
1	Orientation	323.90	1.0	...	0.09	1.72e-01	1.34e-01
2	Position	72.71	1.0	...	0.40	4.46e-02	3.02e-02
3	Thick * Orientation	0.46	1.0	...	0.95	2.92e-04	1.89e-04
4	Thick * Position	0.80	1.0	...	0.93	5.13e-04	3.32e-04
5	Orientation * Position	79.87	1.0	...	0.38	4.87e-02	3.32e-02
6	Thick * Orientation * Position	5.49	1.0	...	0.82	3.51e-03	2.28e-03
7	Residual	1558.54	16.0	...	NaN	NaN	6.47e-01

[8 rows x 8 columns]

elongation:

0.0018329540320133066

	Source	SS	DF	...	p-unc	np2	contribution
0	Thick	1.15e-04	1.0	...	0.28	7.15e-02	6.26e-02
1	Orientation	6.72e-05	1.0	...	0.41	4.32e-02	3.66e-02
2	Position	8.08e-05	1.0	...	0.37	5.15e-02	4.41e-02
3	Thick * Orientation	4.75e-06	1.0	...	0.82	3.18e-03	2.59e-03
4	Thick * Position	5.70e-07	1.0	...	0.94	3.83e-04	3.11e-04
5	Orientation * Position	6.84e-05	1.0	...	0.40	4.39e-02	3.73e-02
6	Thick * Orientation * Position	8.69e-06	1.0	...	0.76	5.81e-03	4.74e-03
7	Residual	1.49e-03	16.0	...	NaN	NaN	8.12e-01

[8 rows x 8 columns]

E:

77849815.97615933

	Source	SS	DF	...	p-unc	np2	contribution
0	Thick	3.38e+07	1.0	...	2.10e-03	4.56e-01	4.34e-01
1	Orientation	3.44e+06	1.0	...	2.60e-01	7.86e-02	4.41e-02
2	Position	1.34e+05	1.0	...	8.21e-01	3.31e-03	1.72e-03
3	Thick*Orientation	8.94e+04	1.0	...	8.53e-01	2.21e-03	1.15e-03
4	Thick*Position	4.38e+02	1.0	...	9.90e-01	1.09e-05	5.62e-06
5	Orientation*Position	5.59e+04	1.0	...	8.83e-01	1.38e-03	7.18e-04
6	Thick*Orientation*Position	4.99e+03	1.0	...	9.65e-01	1.24e-04	6.40e-05
7	Residual	4.03e+07	16.0	...	NaN	NaN	5.18e-01

[8 rows x 8 columns]